AL-TR-90-063

AD:

Interim Report
for the period
November 1988
to June 1990

Aluminum Alloys for Cryogenic Tanks: Oxygen Compatibility Volume 1.

September 1990

Authors:
R.P Reed
N.J. Simon
J.D. McColskey
J.R. Berger
C.N. McCowen
J.W. Bransford
E.S. Drexler
R.P. Walsh

National Institute of Standards and Technology
325 Broadway
Boulder CO 80303

AL 99011

DTIC
ELECTE
NOV 0 8 1990
S E D

AD-A229 229

Approved for Public Release

Prepared for the: **Astronautics Laboratory (AFSC)**
Air Force Space Technology Center
Space Systems Division
Air Force Systems Command
Edwards AFB CA 93523-5000

NOTICE

When U. S. Government drawings, specifications, or other data are used for any purpose other than a definitely related Government procurement operation, the fact that the Government may have formulated, furnished, or in any way supplied the said drawings, specifications, or other data, is not to be regarded by implication or otherwise, or in any way licensing the holder or any other person or corporation, or conveying any rights or permission to manufacture, use or sell any patented invention that may be related thereto.

FOREWORD
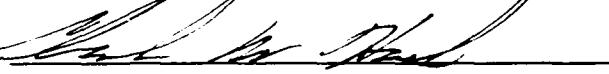
This interim report was submitted by National Institute of Standards and Technology, Boulder CO on completion of contract AL 99011 with the Astronautics Laboratory (AFSC), Edwards AFB CA. AL Project Managers were Bao Nguyen and Lt Bruce Pham.

This report has been reviewed and is approved for release and distribution in accordance with the distribution statement on the cover and on the DD Form 1473.

BAO K. NGUYEN
Project Manager

ROBERT L. WISWELL
Chief, Liquid Propulsion Branch

FOR THE DIRECTOR

CLARK W. HAWK
Director, Propulsion Division

REPORT DOCUMENTATION PAGE

Form Approved
OMB No. 0704-0188

1a. REPORT SECURITY CLASSIFICATION UNCLASSIFIED		1b. RESTRICTIVE MARKINGS
2a. SECURITY CLASSIFICATION AUTHORITY		3. DISTRIBUTION / AVAILABILITY OF REPORT Approved for Public Release Distribution is Unlimited
2b. DECLASSIFICATION / DOWNGRADING SCHEDULE		

4. PERFORMING ORGANIZATION REPORT NUMBER(S) NISTIR 3942	5. MONITORING ORGANIZATION REPORT NUMBER(S) AL-TR-90-063 Vol. 1

6a. NAME OF PERFORMING ORGANIZATION National Institute of Standards and Technology	6b. OFFICE SYMBOL (If applicable)	7a. NAME OF MONITORING ORGANIZATION Astronautics Laboratory (AFSC)
6c. ADDRESS (City, State, and ZIP Code) 325 Broadway Boulder, CO 80303		7b. ADDRESS (City, State, and ZIP Code) AL/RKLB Edwards AFB CA 93523-5000

8a. NAME OF FUNDING / SPONSORING ORGANIZATION	8b. OFFICE SYMBOL (If applicable)	9. PROCUREMENT INSTRUMENT IDENTIFICATION NUMBER AL 99011

8c. ADDRESS (City, State, and ZIP Code)	10. SOURCE OF FUNDING NUMBERS			
	PROGRAM ELEMENT NO.	PROJECT NO. 4SL1	TASK NO 3148	WORK UNIT ACCESSION NO.

11. TITLE (Include Security Classification)
Aluminum Alloys for Cryogenic Tanks: Oxygen Compatibility

12. PERSONAL AUTHOR(S) Reed, Richard Palmer, Simon, Nancy Jane, McColskey, Joseph David, Berger, John Roland, McCowan, Christopher Nelson, Bransford, James Warren, Drexler, Elizabeth Susan,

13a. TYPE OF REPORT Interim	13b. TIME COVERED FROM 8811 9006	14. DATE OF REPORT (Year, Month, Day) 9009	15. PAGE COUNT 204

16. SUPPLEMENTARY NOTATION

17.	COSATI CODES		18. SUBJECT TERMS (Continue on reverse if necessary and identify by block number) aluminum alloys, aluminum-lithium alloys, 8090, 2090, 2219, Weldalite, oxygen compatibility, LOX compatibility, oxygen, reaction, mechanical-impact test, promoted-combustion test
FIELD	GROUP	SUB-GROUP	
13	13		
11	06	01	

19. ABSTRACT (Continue on reverse if necessary and identify by block number)

In Part I of this program, Al-Li alloys 8090-T3 and 2090-T81 and Al alloy 2219 (tempers T851, T37) were tested for compatibility with liquid oxygen using pressurized mechanical-impact apparatuses at two NASA laboratories, Marshall Space Flight Center (MSFC) and White Sands Test Facility (WSTF). Specimens and data from tests at Santa Susana Field Laboratory (SSFL), Rocketdyne, on alloy 2090-T81 were supplied by ALCOA. Pressurized mechanical-impact data on alloy WL049-T351 were produced by WSTF. In addition, WSTF conducted open-cup mechanical-impact and promoted-combustion tests on all alloys.

Reactions occurred in some specimens of all alloys during pressurized mechanical-impact tests at MSFC. There were no reactions during similar tests at WSTF and SSFL. The reactions at MSFC are not attributed to specimen contamination.

20. DISTRIBUTION / AVAILABILITY OF ABSTRACT ☒ UNCLASSIFIED/UNLIMITED ☐ SAME AS RPT ☐ DTIC USERS	21. ABSTRACT SECURITY CLASSIFICATION UNCLASSIFIED	
22a. NAME OF RESPONSIBLE INDIVIDUAL BAO K. NGUYEN	22b. TELEPHONE (Include Area Code) 805-275-5541	22c. OFFICE SYMBOL RKLB

DD Form 1473, JUN 86 Previous editions are obsolete.

12. and Walsh, Robert Patrick.

19. This interim report analyzes the ignitions found in the MSFC pressurized mechanical-impact tests, compares the results and test methodologies of both MSFC and WSTF facilities (since each laboratory is producing test data that are apparently divergent), and addresses the current test standard document NASA NHB 8060.1B[1] as it pertains to this study.

Significant disparities have been identified in the pressurized mechanical-impact test equipment, conditions, and procedures used by the three laboratories. Reactions in the MSFC tests are attributed to test parameter variations that produce excessive local deformation leading to very high local temperatures in the specimens in the presence of oxygen and in the absence of protective oxides. Lack of reactions at WSTF is attributed to lower absorbed-energy levels in the specimens.

All alloys behaved similarly in pressurized mechanical-impact tests, but the Al-Li alloys were superior to alloy 2219 in promoted-combustion tests. However, the pressurized mechanical-impact data are not conclusive. Continuation of the test program is urged at absorbed energy levels of about 65 J, but limited to only one test laboratory to conserve time and resources.

Changes are recommended in NASA NHB 8060.1B[1] (Paragraph 413, Test 13), the NASA qualification standard for mechanical-impact testing to assess oxygen compatibility of materials.

CONTENTS

Appendices

I.A. Excerpts from NASA NHB 8060.1B on Cleaning of Specimens for LOX
       Compatibility Testing
I.B. Promoted Combustion Tests at White Sands Test Facility
I.C. Physical Measurements on Impacted LOX Compatibility Specimens
I.D. Report from Dr. F. Gayle, National Institute of Standards and
       Technology, Gaithersburg, MD
I.E. Summary Report on Observations Made on Aluminum and Aluminum-Lithium
       Alloys Subjected to Impact While in Contact with Liquid Oxygen,
       Dr. M. B. Kasen
I.F. Surface Chemistries of Selected Al-Li Alloys and Alloy 2219,
       C. C. Wan, Aerospace Corporation, Los Angeles, CA
I.G. Ignited Specimens of 2090-T81 That Are Retained by Marshall Space
       Flight Center, Courtesy T. Vaughan, Marshall Space Flight Center,
       Huntsville, AL

LIST OF TABLES

LIST OF FIGURES

x

I.1. **EXECUTIVE SUMMARY**

Aluminum alloys 8090-T3, 2090-T81, 2219-T851, and 2219-T37 have been tested for compatibility with liquid oxygen using pressurized mechanical impact apparatus at two NASA laboratories, Marshall Space Flight Center (MSFC) and White Sands Test Facility (WSTF). Specimens and data from tests at Santa Susana Field Laboratory (SSFL), Rocketdyne, on alloy 2090-T81 have been supplied by ALCOA. Pressurized mechanical impact data on alloy WL049-T351 have been produced by WSTF. In addition, WSTF conducted open-cup mechanical impact and promoted combustion tests on all alloys.

Ignitions occurred in some specimens of all alloys during pressurized mechanical impact tests at MSFC. There were no ignitions during similar tests at WSTF and SSFL. The ignitions at MSFC are not attributed to specimen contamination. Significant disparities have been identified in the pressurized mechanical impact test equipment, conditions, and procedures used by the three laboratories. Ignitions in the MSFC tests are attributed to test parameter variations that produce excessive local deformation leading to very high local temperatures in the specimens in the presence of oxygen and in the absence of protective oxides.

All alloys behaved similarly in pressurized mechanical impact tests, but the Al-Li alloys were superior to alloy 2219 in promoted combustion tests. This leads to the conclusion that Al-Li alloys are at least equivalent to, if not better than, alloy 2219 with respect to oxygen compatibility. However, the pressurized mechanical impact data are not conclusive. Continuation of the test program is urged at absorbed energy levels of about 65 J, but limited to only one test laboratory to conserve time and resources.

Major changes are recommended in NASA NHB 8060.1B[1] (Paragraph 413, Test 13), the NASA qualification standard for mechanical impact testing to assess oxygen compatibility of materials.

   o   Specifications should be developed for the test parameters that affect the absorbed energy of the specimen, such as striker-pin ometry and surface tolerance and the eccentricity of the striker-pin impact with the specimen.

   o   The frictional losses and resiliency-rebound energies that subtract from the plummet potential en rgy (nominal impact energy) to limit the actual energy absorbed by the specimen should be considered in any test configuration. The results should be reported in terms of specimen absorbed energy.

   o   To facilitate interlaboratory and alloy-to-alloy comparisons, suggestions are presented to increase the statistical confidence level of test results.

These improvements will reduce the large disparity in test procedures that exist among laboratories that conduct pressurized mechanical impact tests. Changes in the standard would also provide a closer link between absorbed energies from structural failure analysis to specimen absorbed energy in mechanical impact tests.

I.2. INTRODUCTION

The oxygen-compatibility studies reported here are part of a broader National Institute of Standards and Technology (NIST) program to assess new high-strength Al-Li alloys for use in the cryogenic tankage of the Advanced Launch System (ALS). This program is sponsored by the Air Force Systems Command, Astronautics Laboratory, Edwards Air Force Base, with Bao Nguyen, Task Manager. It is part of the Materials and Processes Validation (3101) of the Structures, Materials, and Manufacturing (3000) portion of the ALS Advanced Development Program.

The purpose of the NIST oxygen-compatibility program has been to assess the relative compatibility with liquid and gaseous oxygen of high-strength aluminum alloys for use in ALS cryogenic tanks. Program objectives are: (1) to provide well-characterized specimens of state-of-the-art commercial Al alloys for LOX (liquid oxygen) and GOX (gaseous oxygen) measurements at both qualified NASA test laboratories, MSFC and WSTF; (2) to study the roles of intrinsic material variables, such as fracture properties, chemistry, and inclusions, on ignition characteristics; and (3) to assess the extrinsic test variables, such as impact energy, pressure, temperature, and specimen size, orientation, and specimen location (within the plate) on ignition tendencies.

We provide this interim report now for two reasons: (1) our test results at MSFC have shown ignition events in all Al alloys that have been tested (2090, 8090, 2219), and (2) MSFC has temporarily closed their facilities to outside (ALS) use. The halt in the test program has provided a convenient time for assessment of the test results.

A number of experts assisted us in this study. James W. Bransford (NIST, Boulder) is currently studying combustion of laser-heated metals. His advice and previous experience have been valuable. Roberto J. Rioja and the ALCOA Al-Li research staff, led by Richard S. James, have been extremely cooperative and, have supplied their specimens and data from tests at SSFL, which are included in this report. Chung-Chu Wan of the Aerospace Corporation conducted accurate and very relevant surface chemical and scanning electron microscopy (SEM) studies of specimens selected from our test program. Frank W. Gayle of NIST, Gaithersburg, contributed his extensive knowledge of Al-Li alloy metallurgy and SEM analysis of a MSFC striker pin. Maurice B. Kasen, formerly of NIST, studied our impacted specimens and suggested several possible ignition mechanisms. Timothy P. Vaughan (MSFC) has supervised surface chemical analysis of specimens tested at MSFC and provided a summary of his observations. Without these contributions, our investigation could not have been focused as rapidly and would have lacked some insight into possible ignition causes and effects.

This interim report analyzes the ignitions found in the MSFC pressurized mechanical impact tests, compares the results and test methodologies of both MSFC and WSTF facilities (since each laboratory is producing test data that are apparently divergent) and addresses the current test standard document NASA NHB 8060.1B[1] as it pertains to this study.

I.3. MATERIAL CHARACTERIZATION

I.3.1. Inventory

A list of the alloys, suppliers, dates that alloys were received by NIST, and quantity of material is found in Table I.3.1. This interim report covers the following alloys: 8090-T3, 2090-T81, WL049-T351, 2219-T851, and 2219-T37. Compatibility tests have not been performed on other alloys or tempers.

Portions of our material inventory have been distributed to other laboratories [Oak Ridge National Laboratory (ORNL), WSTF, MSFC, and Boeing Aerospace]. Figure I.3.1 indicates the type of research conducted on these alloys by these laboratories and also includes ongoing research activities at NIST on these alloys.

I.3.2. Chemical Composition

The chemical compositions of the alloys, as furnished by the material suppliers,[*] are given in Table I.3.2. All compositions fall within the Aluminum Association specifications for each alloy. There are two slightly different compositions listed for 8090: one corresponds to the material used in LOX compatibility testing, the other to the material used in tensile and toughness tests. The WL049 alloy does not have a generic specification at this time, and is commonly termed Weldalite 049^{TM}.[**]

I.3.3. Mechanical Properties

The mechanical properties were characterized at low temperatures using the following tests: tensile, fracture toughness, and hardness. Results of tensile and fracture toughness tests are given in Table I.3.3 (8090), Tables I.3.4 and I.3.5 (2090), Table I.3.6 (WL049, tensile data only), and Tables I.3.7 and I.3.8 (2219). Tensile values reported in these tables are the mean of two test results. Fracture toughness values each represent one test result. Fracture toughness is not reported for WL049-T351. Details of the test procedures and results are presented below.

I.3.3.1. Tensile Tests

Displacement control tensile tests were carried out at 295 K (ambient), 76 K (liquid nitrogen), 20 K (cold helium gas), and 4 K (liquid helium). At ambient temperature, the tensile tests were performed according

[*]The analyses of the 2219 alloys were furnished by an independent contractor.

[**]Trade names are furnished to identify the material adequately. Such identification does not imply recommendation or endorsements by NIST, nor does it imply that the materials identified are necessarily the best available for the purpose.

3

Table I.3.1. Inventory of Al and Al-Li Plate Material.

Date Received	Supplier	Alloy	Quantity	Plate Dimensions, in
June 29, 1989	ALCAN	8090-T3	5	10 x 10 x 0.5
July 12, 1989	Kaiser	2219-T851	4	48 x 48 x 0.5
July 12, 1989	Kaiser	2219-T37	4	48 x 48 x 0.5
Aug 10, 1989	ALCOA	2090-T81	1	48 x 96 x 0.5
			1	48 x 96 x 0.75
Sept 19, 1989	Reynolds	WL049-T3	2	48 x 48 x 0.5
Sept 22, 1989	ALCAN	8090-T8771	4	36 x 64 x 0.5
Oct 3, 1989	Reynolds	WL049-T6	4	48 x 48 x 0.5
Oct 11, 1989	ALCAN	8090-T8151	3	36 x 60 x 0.5
Nov 27, 1989	Reynolds	WL049-T8	2	48 x 48 x 0.5

Table I.3.2. Compositions of Al Alloys, wt%.

Alloy	Cu	Li	Mg	Zr	Si	Fe	Ti	Cr	Zn	Ag	Ni	B	Pb	Sn	Mn
8090-T3 oxygen[1]	1.18	2.23	0.63	0.11	0.02	0.04	0.024	0.001	0.02	—	0.004	0.0001	0.002	0.007	—
8090-T3 tensile[2]	1.16	2.34	0.61	0.12	0.03	0.05	0.030	0.002	0.03	—	0.001	0.0008	0.004	0.007	—
2090-T81 1/2 in	2.70	2.3	0.03	0.12	—	0.08	0.19	<0.00	0.01	—	0.01	0.0000	—	—	<0.00
2090-T81 3/4 in	2.85	2.3	0.05	0.10	—	0.07	0.13	<0.00	0.02	—	0.01	0.0007	—	—	<0.00
WL049-T351	4.72	1.28	0.42	0.12	0.02	0.03	0.02	<0.00	0.02	0.35	0.01	—	—	—	<0.00
2219-T851	5.71	—	—	0.08	0.04	0.02	0.044	0.18	—	—	0.016	—	—	—	0.24
2219-T37	5.72	—	—	0.028	0.04	0.018	0.03	0.02	—	—	0.01	—	—	—	0.22

[1] plate 3516 301A

[2] plate 3518 302A

```
NIST:    METALLOGRAPHY
         HARDNESS
         TENSILE
         FRACTURE TOUGHNESS

ORNL:    WELDING

NIST MATERIAL
INVENTORY        WSTF:   LOX, GOX COMPATIBILITY
                         OPEN CUP
                         PRESSURIZED
                         PROMOTED COMBUSTION

                 MSFC:   LOX, GOX COMPATIBILITY
                         OPEN CUP
                         PRESSURIZED

                 BOEING: PLASMA-ARC WELDING
```
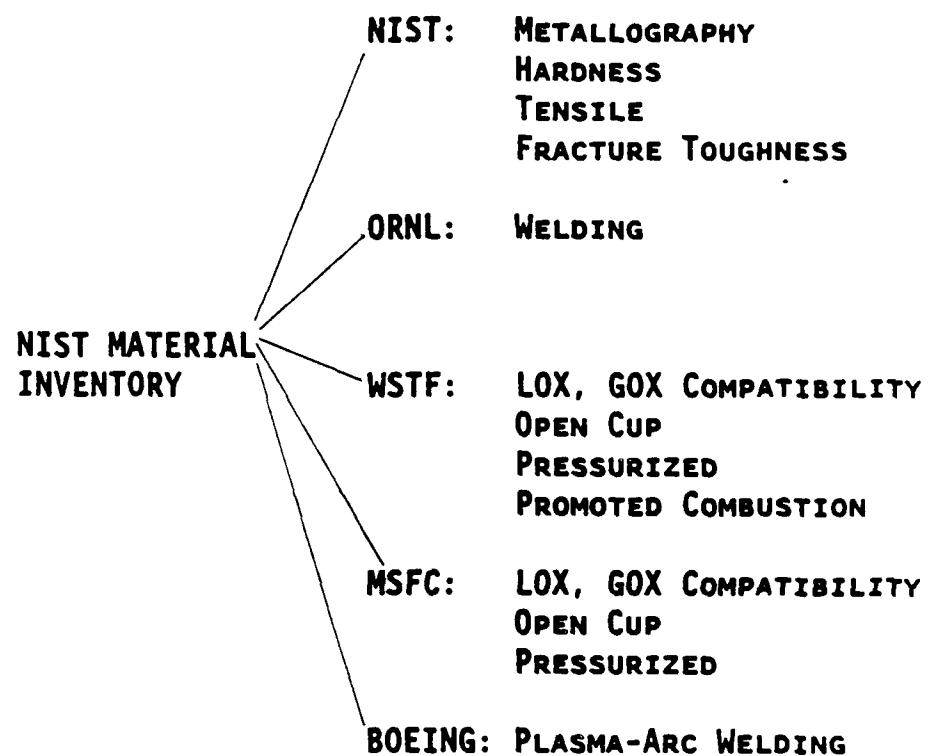
Figure I.3.1. Distribution and research uses of the NIST material
              inventory.

Table I 3.3. Tensile and Toughness Properties: 8090-T3.

Test Temp. K	Orientation	Yield Strength, MPa (ksi)	Tensile Strength, MPa (ksi)	Elonga-tion[*] %	Reduction of Area, %	Toughness MPa/m	(ksi/in)
295	L L-T	217 (31)	326 (47)	12	18	—	—
295	T T-L	208 (30)	348 (50)	14	26	—	—
76	L L-T	248 (36)	458 (66)	22	27	97	(88)
76	T T-L	241 (35)	450 (65)	20	37	60	(55)
20	L L-T	272 (39)	609 (88)	28	28	—	—
20	T T-L	268 (39)	592 (86)	25	27	—	—
4	L L-T	280 (41)	605 (88)	26	28	74	(67)
4	T T-L	270 (39)	597 (87)	24	29	50	(45)

*Measured over 1.5 in G.L.

Table I.3.4. Tensile and Toughness Properties: 2090-T81, 0.50-in-thick plate.

Test Temp., K	Orientation	Yield Strength, MPa (ksi)		Tensile Strength, MPa (ksi)		Elongation,* %	Reduction of Area, %	Toughness, MPa√m (ksi√in)	
295	L L-T	501	(73)	530	(77)	7	9	35	(32)
295	T T-L	507	(73)	546	(79)	2	4	34	(31)
76	L L-T	550	(80)	616	(89)	9	9	74	(67)
76	T T-L	570	(83)	610	(88)	1	4	27	(25)
20	L L-T	591	(86)	715	(104)	12	10	—	—
20	T T-L	613	(89)	666	(97)	1	2	—	—
4	L-T L	600	(87)	688	(100)	10	17	58	(53)
4	T T-L	621	(90)	669	(97)	1	4	41	(37)

*Measured over 1 0 in G.L.

8

Table I.3.5.   Tensile and Toughness Properties: 2090-T81, 0.75-in-thick plate.

Test Temp., K	Orientation	Yield Strength, MPa (ksi)		Tensile Strength, MPa (ksi)		Elongation* %	Reduction of Area, %	Toughness MPa√m (ksi√in)	
295	L	578	(84)	608	(88)	8	17		
	L-T							37	(34)
295	T	559	(81)	597	(86)	6	13		
	T-L							25	(23)
76	L	649	(94)	738	(107)	10	2		
	L-T							33	(30)
76	T	624	(90)	· 693	(100)	3	4		
	T-L							24	(22)
20	L	665	(96)	836	(121)	15	12		
	L-T							—	—
20	T	663	(96)	764	(111)	4	7		
	T-L							—	—
4	L	672	(97)	861	(125)	12	7		
	L-T							44	(40)
4	T	670	(97)	760	(110)	3	4		
	T-L							38	(35)

*Measured over 1.0 in G.L.

9

Table I.3.6. Tensile Properties: WL049-T351.

Test Temp., K	Orien- tation	Yield Strength, MPa (ksi)		Tensile Strength, MPa (ksi)		Elonga- tion, [*] %	Reduction of Area, %
295	L	453	(66)	551	(80)	11	15
295	T	412	(60)	541	(78)	14	22
76	L	583	(84)	680	(99)	12	14
76	T	506	(73)	671	(97)	14	13
20	L	703	(102)	858	(124)	13	12
20	T	606	(88)	803	(116)	10	13
4	L	699	(101)	853	(124)	13	15
4	T	621	(90)	792	(115)	10	16

*Measured over 1.0 in G.L.

Table I.3.7. Tensile and Toughness Properties: 2219-T851.

Test Temp., K	Orientation	Yield Strength, MPa (ksi)		Tensile Strength, MPa (ksi)		Elonga-tion,[*] %	Reduction of Area, %	Toughness, MPa√m (ksi√in)	
295	L	342	(50)	447	(65)	8	19		
	L-T							31	(28)
295	T	331	(48)	443	(64)	8	16		
	T-L							30	(27)
76	L	409	(59)	556	(81)	10	22		
	L-T							41	(37)
76	T·	405	(59)	557	(81)	9	16		
	T-L							38	(35)
20	L	430	(62)	642	(93)	11	17		
	L-T							—	—
20	T	424	(61)	649	(94)	11	17		
	T-L							—	—
4	L	439	(64)	662	(96)	10	18		
	L-T							42	(38)
4	T	434	(63)	660	(96)	9	15		
	T-L							36	(33)

*Elongation measured over 1.50 in G.L.

Table I.3.8 Tensile and Toughness Properties: 2219-T37.

Test Temp., K	Orientation	Yield Strength, MPa (ksi)		Tensile Strength, MPa (ksi)		Elonga-tion,* %	Reduction of Area, %	Toughness, MPa√m (ksi√in)	
295	L	333	(48)	391	(57)	12	28		
	L-T							31	(28)
295	T	303	(44)	398	(58)	11	25		
	T-L							26	(24)
76	L	420	(61)	510	(74)	17	27		
	L-T							41	(37)
76	T	381	(55)	518	(75)	16	21		
	T-L							32	(29)
20	L	500	(72)	665	(96)	18	19		
	L-T							—	—
20	T	463	(67)	668	(97)	13	18		
	T-L							—	—
4	L	516	(75)	671	(97)	17	23		
	L-T							35	(32)
4	T	477	(69)	668	(97)	14	16		
	T-L							33	(30)

*Elongation measured over 1.50 in G.L.

to the ASTM E8 standard method. For cryogenic temperature tests, a procedure based upon ASTM E8 was used. Further details of the experimental procedure for cryogenic measurements are reported elsewhere.[2] The engineering data obtained from these tests were yield strength, tensile strength, and ductility.

Round tensile specimens with a 6-mm (0.25-in) diameter by 38-mm (1.50-in) long reduced gage section were machined with the tensile axis oriented either transversely or longitudinally to the plate rolling direction. All specimens were cut so that the gage section of the specimen was centered within the plate thickness.
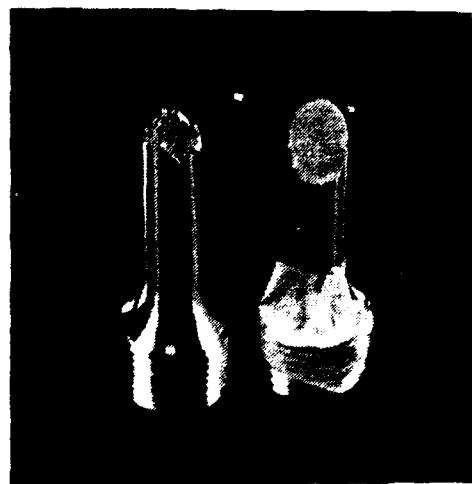
The tensile tests give information on both strength and fracture characteristics. The yield and tensile strengths of all the alloys exhibit a temperature dependence. As the test temperature decreases, the strength increases. At room temperature, a ranking of the materials in the order of their yield strengths shows that 2090-T81 has the highest strength and 8090-T3 the lowest. The two tempers of 2219 have a slightly higher strength than the 8090-T3 but are fairly close to each other. Alloy WL049-T351 falls in the middle.

At 20 K, the ranking of materials on the basis of strength is changed. WL049-T351 has the highest yield strength but the strength shows a fairly strong dependence on specimen orientation. The transversely oriented specimens had a yield strength approximately 15% lower than that of the longitudinally oriented specimens. The longitudinally oriented specimens of the other alloys usually showed higher yield strengths than the transverse specimens but the difference was usually only a few percent. The tensile fracture characteristics of these alloys are distinctive and worth noting. The Al-Li alloys can be generalized since they exhibited fairly common characteristics according to specimen orientation and test temperature.

At room temperature, the Al-Li alloys exhibited two different failure modes depending on the orientation of the specimen. The transversely oriented specimens failed under a global shear mode but also displayed smaller, grain-size shear failures along the major 45° fracture surface. This behavior, which is shown in Figure I.3.2a, results from the highly laminated microstructure of the Al-Li alloys. Longitudinal specimens also typically failed in a global shear mode with a resulting single-plane 45° fracture surface, as illustrated in Figure I.3.2b.
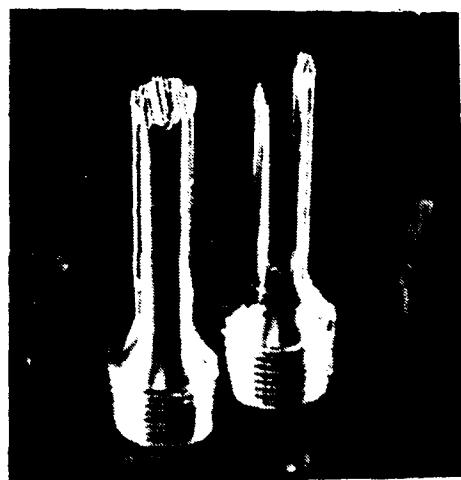
At low temperatures, the failure of the transversely oriented specimens was similar to the failures at room temperature (see Figure I.3.3a). However, the longitudinally oriented specimens showed large amounts of delamination parallel to the tension axis. This delamination behavior, shown in Figure I.3.3b, is again due to the pancake-like grain structure and to the presence of precipitates at the grain boundaries in the Al-Li alloys.

The fracture surfaces of the two tempers of the 2219 alloys were less orientation dependent. The T851 temper exhibited a transition in fracture surface appearance from a ductile, cup-cone type of fracture at room temperature to a 45° shear, single-plane fracture at 4 K. The 2219-T37

13

(a)   (b)

Figure I.3.2. Al-Li tension specimens (a) transverse orientation, (b)
               longitudinal orientation tested at room temperature.

(a)   (b)

Figure I 3 3. Al-Li tension specimens (a) transverse orientation, (b)
               longitudinal orientation.

temper also showed a transition from a 45° shear single-plane fracture at
room temperature to a jagged fracture surface oriented perpendicular to the
tensile axis.

The stress-strain curves of alloys 8090-T3, 2090-T81, WL049-T351, 2219-
T851, and 2219-T37 for the longitudinal orientation are plotted in Figures
I.3.4 to I.3.8. At 76 K, the 2090-T81 alloy exhibits very little work
hardening (σ_u/σ_y - 1.05). But the other alloys show good to excellent work
hardening and plastic strain ranges (σ_u/σ_y - 1.4, 1.6, and 1.8 for alloys
2219-T37, 2219-T851, and 8090-T3, respectively). Other deformation
characteristics will be described in future reports.

I.3.3.2. Fracture Toughness Tests

The J-integral testing was carried out on compact specimens with the
thickness of the as-received plate. The specimen width was 2.0 in (50 mm).
The machined notch was modified to permit attachment of a clip gage in the
loadline.

The J-integral specimens were precracked using a 100 kN (22.5 klb)
fatigue testing machine and cryostat. The J-integral specimens were
precracked at room temperature for the room temperature tests and at 76 K
for the cryogenic tests. All fatigue operations were conducted in load
control using a sinusoidal load cycle at 30 Hz. After precracking, the
specimens were removed from the test machine. The specimens precracked at
76 K were warmed to room temperature before testing at low temperatures.

The J-integral tests followed ASTM standard E813-88, Standard Test
Method for J_{Ic}, "A Measure of Fracture Toughness," using the single specimen
technique. The test was conducted using a computerized data acquisition
system which calculated crack lengths from the elastic unloadings, energy
absorbed by the specimen, and simultaneously plotted the resistance curve
(J vs. Δa).

The critical value of J, J_{Ic}, defined as the J value at the initiation
of crack extension, was obtained using an algorithm following E813-81. An
estimation of the plane strain fracture toughness parameter, $K_{Ic}(J)$, was
made using

$$K_{Ic}^2(J) - EJ_{Ic} \qquad (3-1)$$

where E is Young's modulus. Values of E used at each temperature were
obtained from tensile tests.

The 8090-T3 alloy exhibited the highest toughness values in comparison
to the other alloys at a given temperature and orientation. (A higher
toughness would generally be expected from a T3 temper than from a T8
temper.) However, the 8090-T3 had the largest change in toughness due to
orientation: note the 50% drops in toughness between the LT and TL
configurations. The toughness values for the remaining alloys are approxi-
mately equivalent. The only exceptions are the relatively high values for
the LT orientation at 2090-T81 at 76 K and 4 K for specimens from the 0.5-in

15
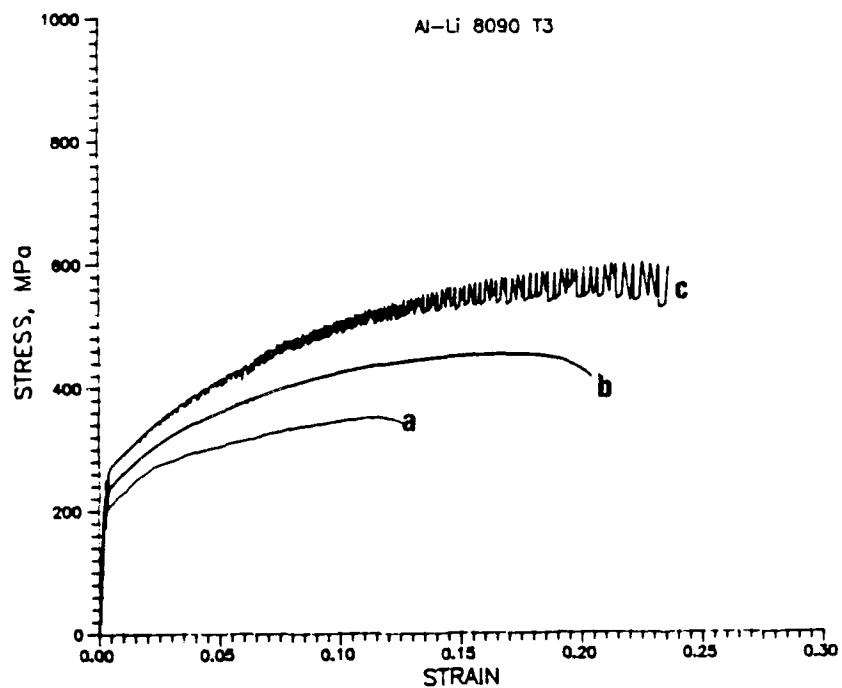
Figure I.3.4.   Stress vs. strain at (a) room temperature, (b) 76 K, and
(c) 4 K for 8090-T3.
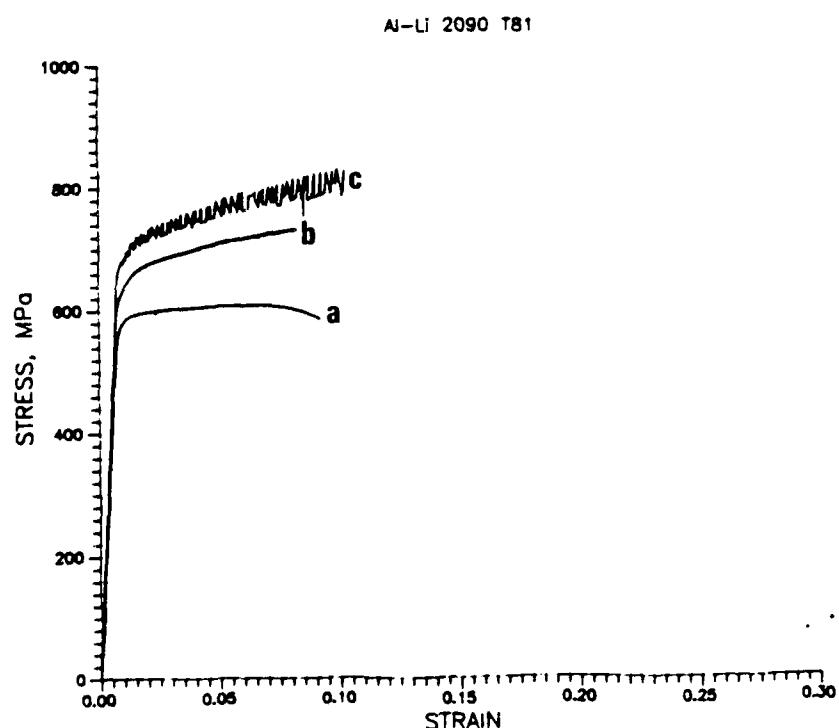
Figure I 3.5.   Stress vs. strain at (a) room temperture, (b) 76 K, and
(c) 4 K for 2090-T81.

16
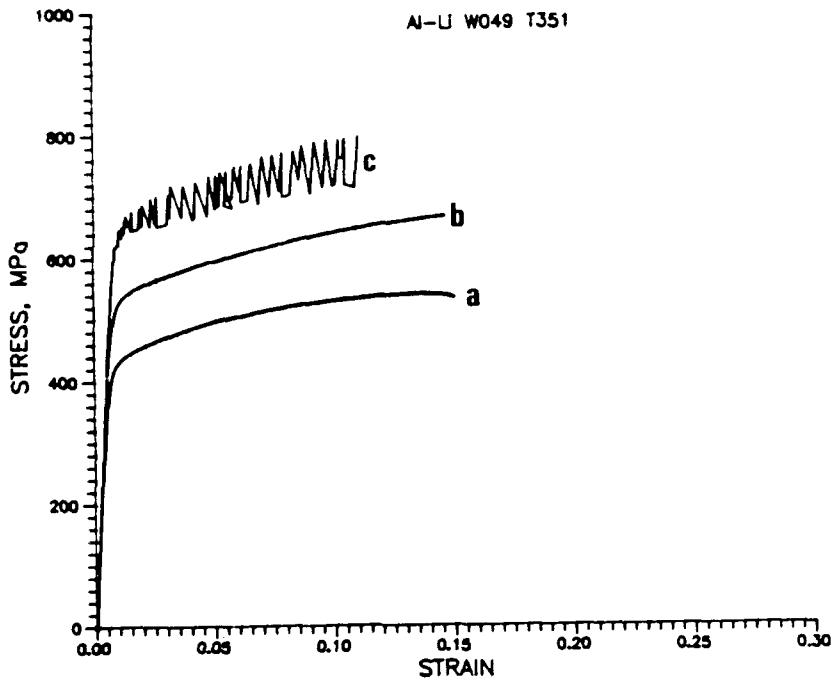
Figure I.3.6. Stress vs. strain at (a) room temperature, (b) 76K, and (c) 4 K for WL049-T351.
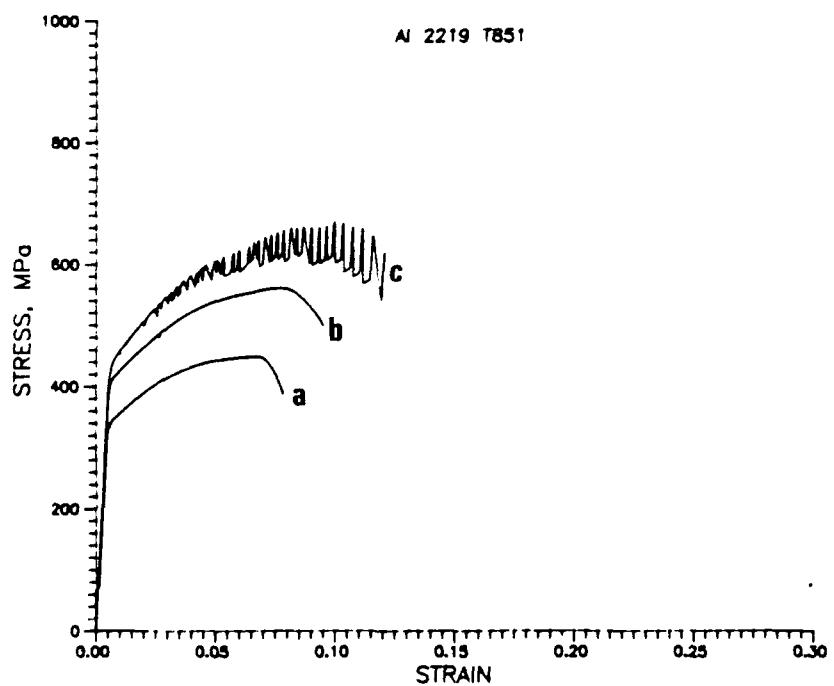
Figure I.3.7. Stress vs. strain at (a) room temperature, (b) 76 K, and (c) 4 K for 2219-T851.

17
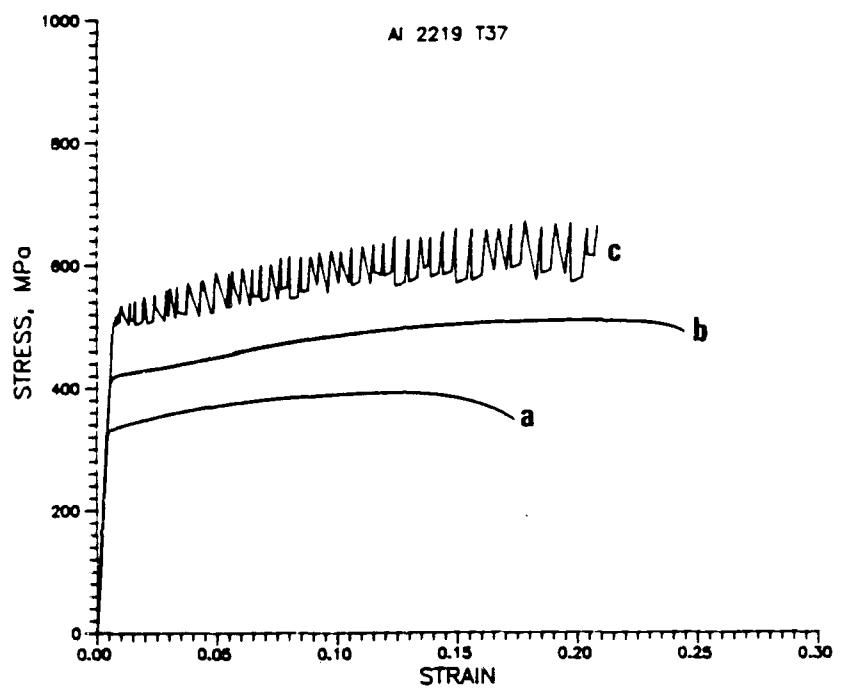
Figure I.3.8. Stress vs. strain at (a) room temperature, (b) 76 K, and (c) 4 K for 2219-T37.

(12.7-mm) thick plate. The large increase in toughness is not evident in the low-temperature LT specimens from the 0.75-in (19.0-mm) thick plate. Therefore, final conclusions about this apparent toughening at low temperatures of alloy 2090-T81 will require data from multiple specimens.

I.3.3.3. Hardness Tests

Vickers microhardness tests were conducted on nonimpacted oxygen compatibility specimens. Each sample was sectioned as shown in Figure I.3.9 and mounted in epoxy. Hardness traverses were made across the specimen's top surface and across the specimen at approximately one-half of the thickness. For purposes of this discussion, the surface traverse is called "surface" and the mid-thickness traverse is called the "profile."

The variation in Vickers hardness with position is illustrated in Figure I.3.10—I.3.13. In each figure the values from the "profile" traverse are above those from the "surface" traverse. All graphs have been plotted with a common y-axis so direct comparisons between the alloys can easily be made. Averages and standard deviations (S.D.'s) for the hardness of each alloy are summarized in Table I.3.9.

The 2090-T81 alloy was the hardest of the four alloys. The two tempers of 2219 had lower hardnesses than the 2090-T81 but were higher than that for the 8090-T3. Under identical static loading conditions, therefore, we can expect the 8090-T3 alloy to undergo the most deformation with smaller deformations occurring in the 2090 and 2219 alloys. The dynamics of impact loading require consideration of the relative resiliencies of the alloys and absorbed energy to predict dynamic indentation behavior.

I.3.4. Physical Properties

I.3.4.1. Density and Elastic Modulus

Table I.3.10 presents density and modulus values for the Al-Li alloys and alloy 2219. Sources of these data are referenced in the table.

I.3.4.2. Specific Heat

The available specific heat data for alloys 8090 and 2090 between 155 and 598 K are shown in Figure I.3.14. Some of these data, obtained by differential scanning calorimetry to indicate the dissolution of precipitates and the formation of subsequent phases produced by various aging treatments, are shown in a smoothed form,[9,10] or are omitted[9] above 400 K. At present, there are no specific heat data for WL049 or 2219 alloys in the cryogenic temperature range. The curve for the specific heat of alloy 2219 vs. temperature presented in Figure 3.2.6.0. of MIL-HDBK 5E[7] appears to be based upon data from Al-alloy 2024.[11,12] The composition of alloy 2024 (4.5Cu, 1.5Mg, and 0.6Mn), is similar to the composition of alloy 2219 (5.8—6.8Cu, and 0.2—0.4Mn). These data, labeled 2024 (2219), are also given in Figure I.3.14.
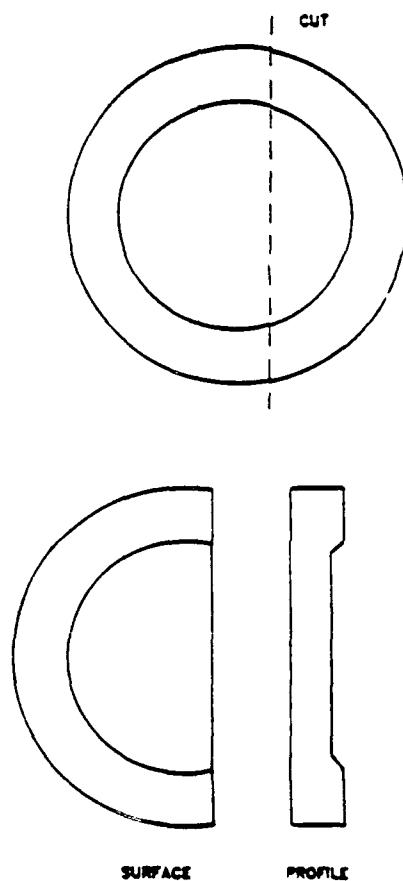
Figure I.3.9. Sectioning of impact specimen for hardness testing.

Table I.3.9. Vickers Hardness Tests on Non-Impacted Compatibility Specimens.

ALLOY	8090-T3		2090-T81 (3/4-in plate)	
	Profile	Surface	Profile	Surface
Avg.	120.9	118.5	197.6	198.3
S.D.	3.0	3.9	4.6	6.5
Specimen Thickness	1/16 in	1/16 in	1/8 in	1/8 in

ALLOY	2219-T851		2219-T37	
	Profile	Surface	Profile	Surface
Avg.	148.8	154.8	136.6	142.9
S.D.	7.5	10.5	4.5	5.4
Specimen Thickness	1/16 in	1/16 in	1/16 in.	1/16 in.

Table I.3.10.   Density and Modulus Values for Al Alloys.

Alloy	Li, wt.%	Cu, wt.%	ρ, x 10^3 kg/m^3 (lbs/in^3)	E, GPa (10^6 psi)	Ref.
8090	2 3–2.6	1.0–1.4	2.54 (0.092)	79.3 (11.5)	3
2090	1.9–2.6	2.4–3.0	2 57 (0.093) 2.59 (0.093)	75.8 (11.0)	4, 5
WL049	1.3	4.5–6.3	2.71 (T6) (0.098)	76 (11.0)	6
2219	—	6.3	2.85 (0.103)	70.3 (10.2)	7,8
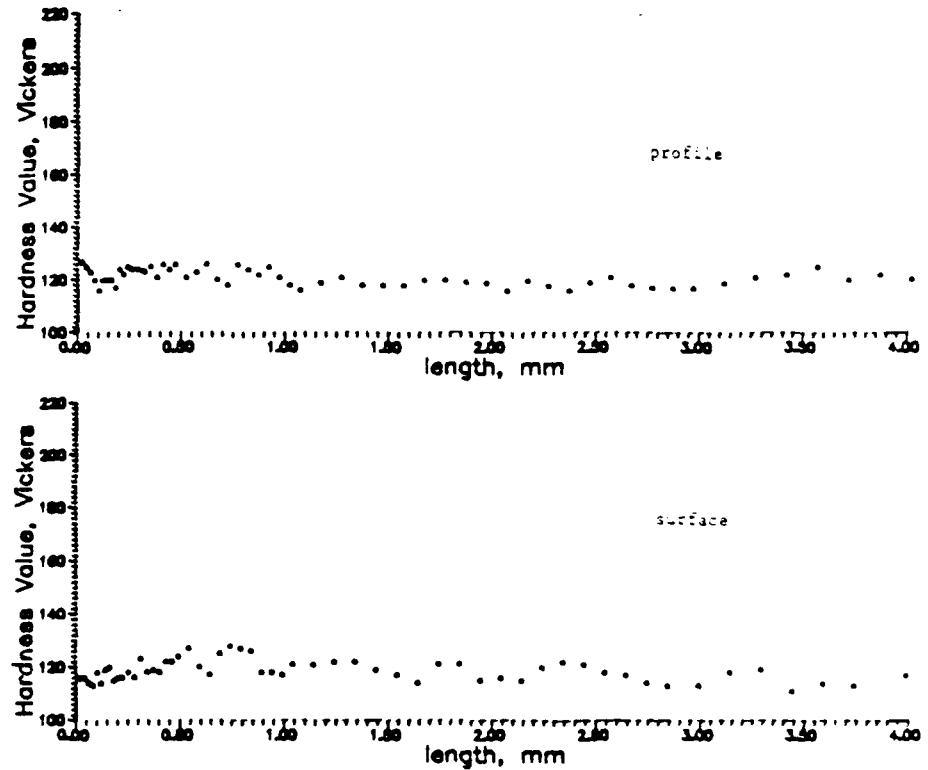
Figure I.3.10. Hardness profiles: Nonimpacted 8090-T3 specimens.
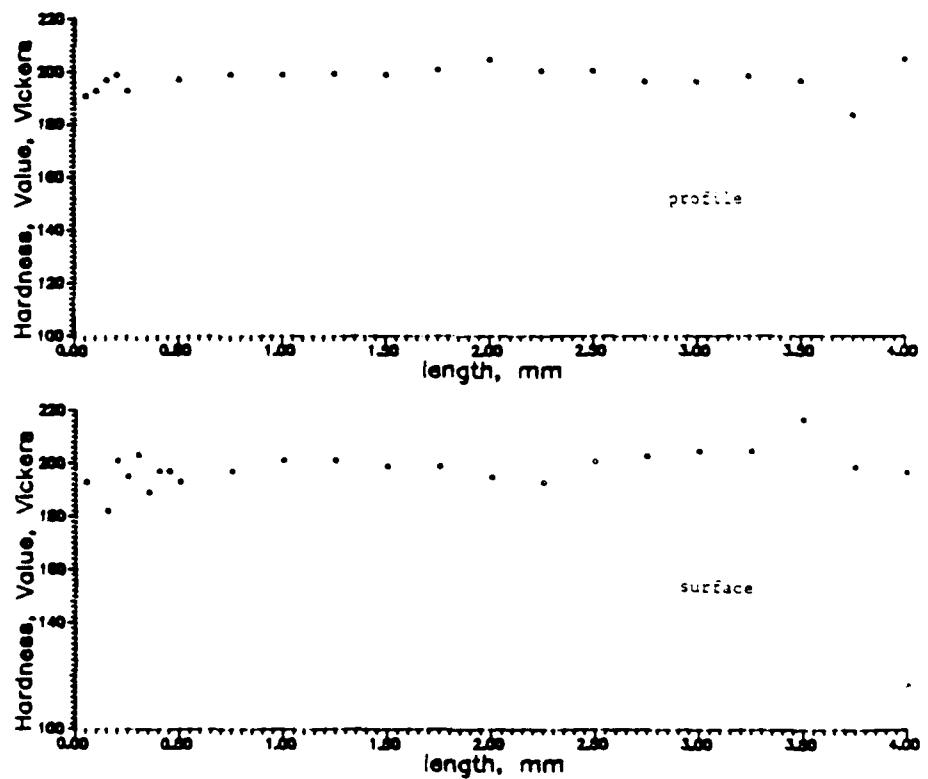
Figure I.3.11. Hardness profiles: Nonimpacted 2090-T81 specimens.
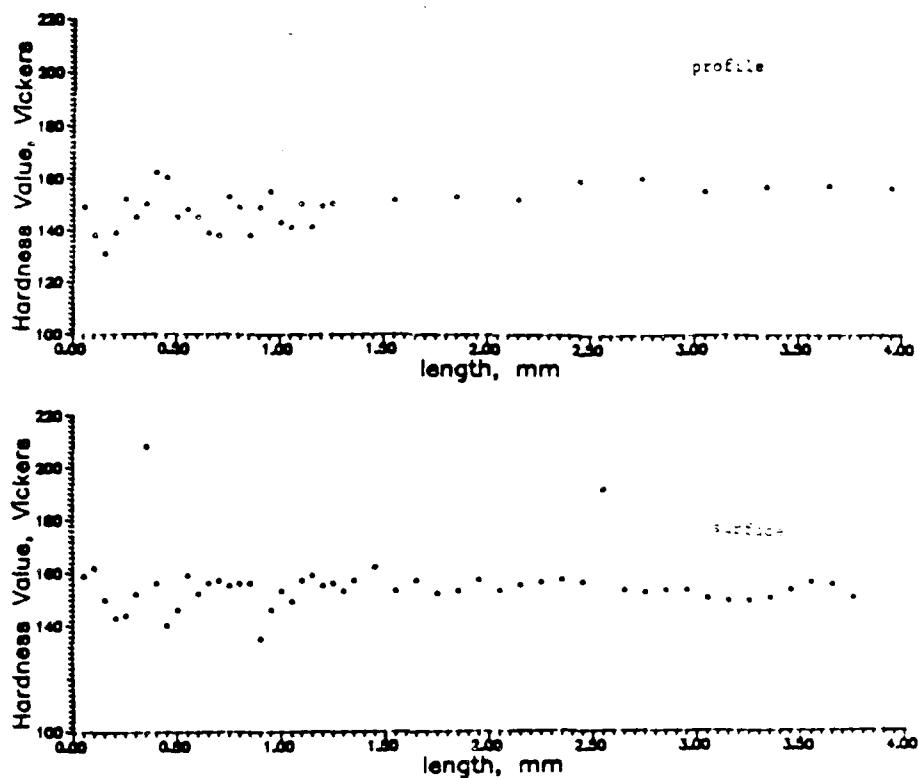
Figure I.3.12. Hardness profiles: Nonimpacted 2219-T851 specimens.
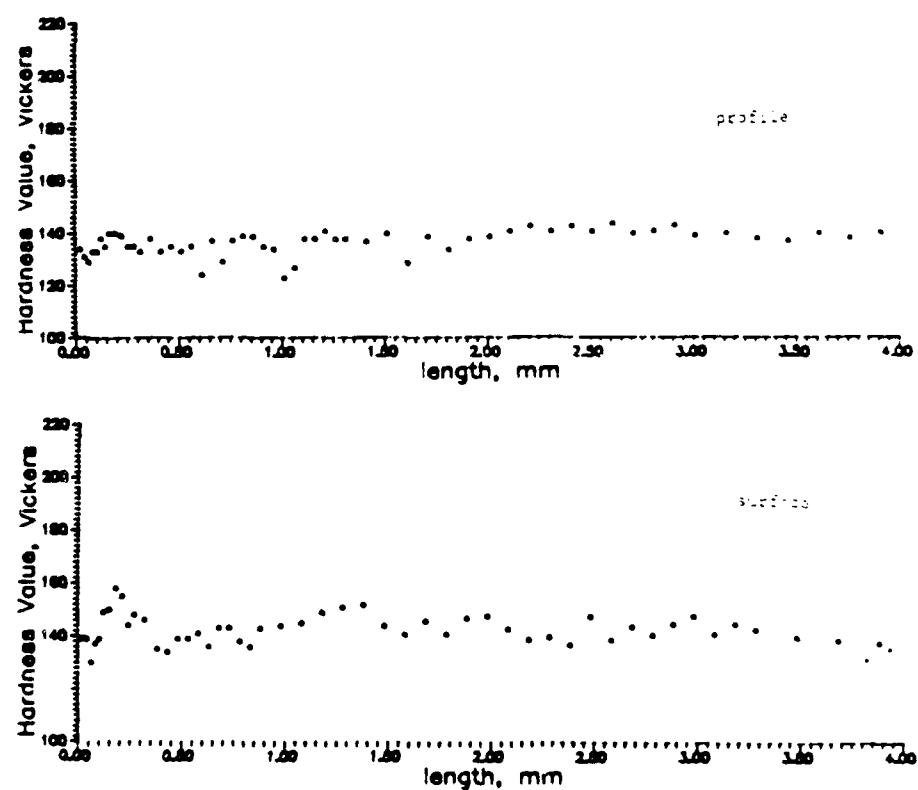
Figure I 3.13. Hardness profiles: Nonimpacted 2219-T37 specimens.

24
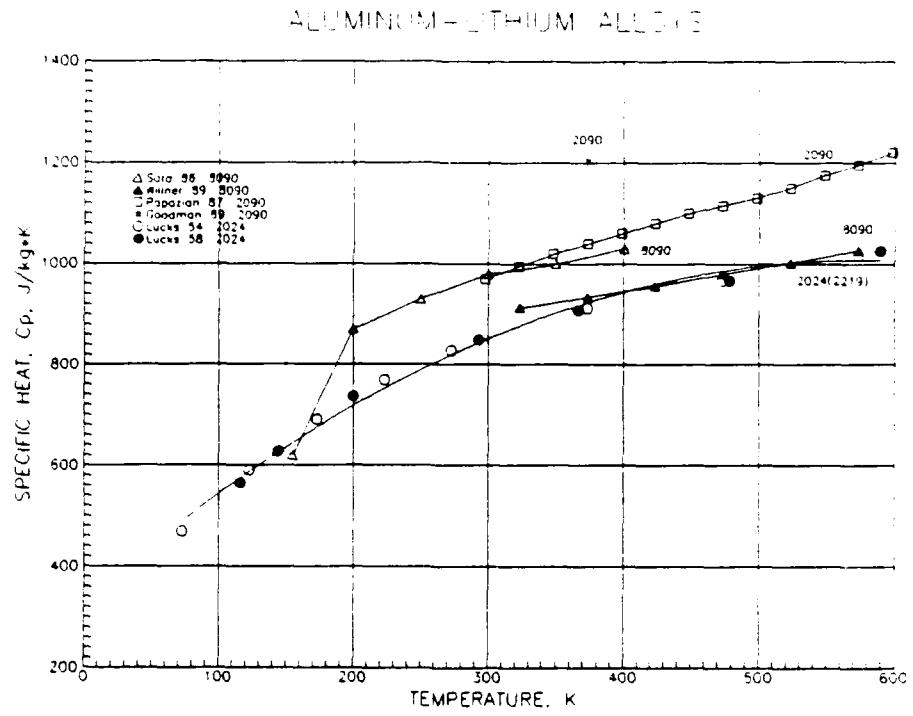
Figure I.3.14. Specific heat vs. temperature for Al alloys 8090, 2090, and 2024(2219).
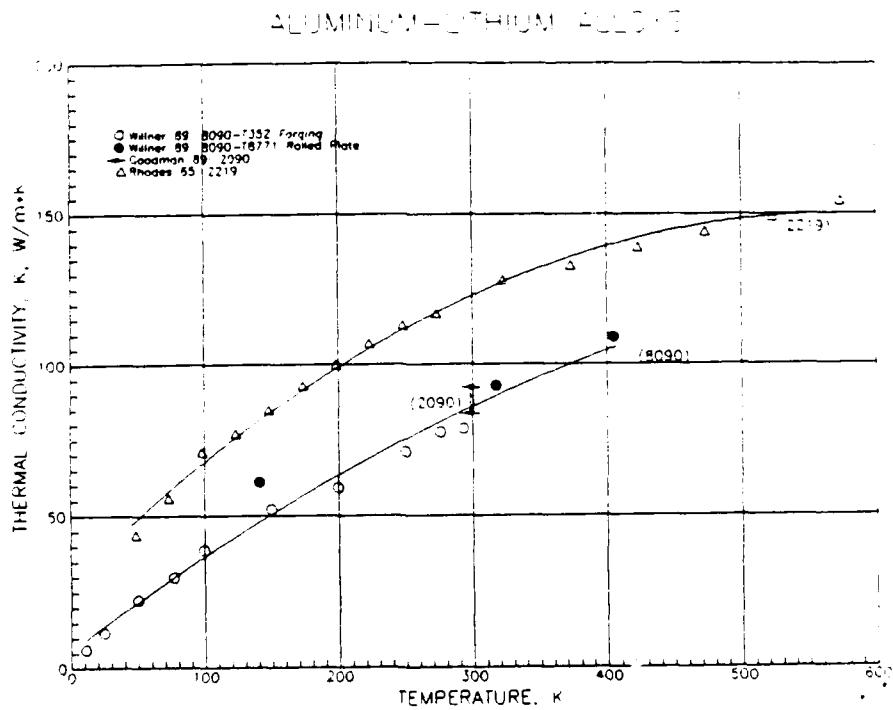
Figure I.3.15. Thermal conductivity vs. temperture for Al alloys 8090, 2090, and 2219.

The specific heat of an alloy can be approximated, near ambient temperature, by a linear combination of the specific heats of the constituent elements.[13] Because the specific heat of Li is about 4 times larger than the specific heat of Al, and about 9 times larger than that of Cu, the specific heats of alloys 8090 and 2090 should be about 10% higher than that of alloy 2219. This is similar to what is shown in Figure I.3.14 for data of Sato[9] on alloy 8090 and Papazian[10] on alloy 2090. However, the higher temperature data on alloy 8090[3] appear quite similar to that of alloy 2024 (2219), and therefore, are probably too low. Variations in aging conditions and chemistry for individual heats can result in changes in the fine structure of a specific heat curve for Al-Li alloys, especially above ambient temperatures. This could account for this apparent discrepancy, and perhaps, also, for one unexpectedly high value of specific heat[5] at 100 °C. More measurements of the specific heat on current production heats of Al-Li alloys would be very desirable.

For the thermal calculations in Section 7, an artificial curve was synthesized that combined alloy 2090 data[10] from 300 to 600 K, alloy 8090 data[9] from 200 to 300 K, and joined smoothly to the 2024 (2219) curve below 100 K. A fourth-order polynomial was fitted to this synthesized curve and then integrated to estimate the temperature rise that would be produced in the specimens after absorption of the impact energy.

I.3.4.3. Thermal Conductivity

Thermal conductivity data for alloys 8090, 2090 (ambient temperature only), and 2219 between 11 and 573 K are given in Figure I.3.15. The solid lines shown in the figure represent the fit of second-order polynomials to the alloy 8090[3] and alloy 2219[14] data. These thermal conductivity data were also used in the calculations discussed in Section 7. At 100 K, approximately the temperature of impact, Figure I.3.15 indicates that the thermal conductivity of Al-Li alloys 8090 and 2090 may be about half that of alloy 2219. However, thermal conductivity of Al alloys at low temperatures is composition and cold-work sensitive.[15]

I.3.5.   Microstructure of the As-Received Materials

The two 8090-T3 alloy plates (3516-301A and 3518-302A) have a similar pancake-grain morphology and size (Figure I.3.16). The average grain length in the rolling plane is 0.6 mm, and the average grain thickness is about 0.02 mm. Some recrystallization is evident, but, in general, the structures of these alloys show unrecrystallized grains with equiaxial subgrain sizes ranging from 0.01 to 0.05 mm (Figure I.3.17). The distribution of inclusions (undissolved phases and impurities) in the alloys is indicative of the as-cast structure (Figure I.3.18). The inclusions do not necessarily coincide with the grain boundary traces on the rolling plane. However, on planes perpendicular to the rolling plane, there is a much stronger correlation between the positions of grain boundaries and inclusions (Figure I.3.18). This observation is generally valid for the Al-Li alloys covered in this report.
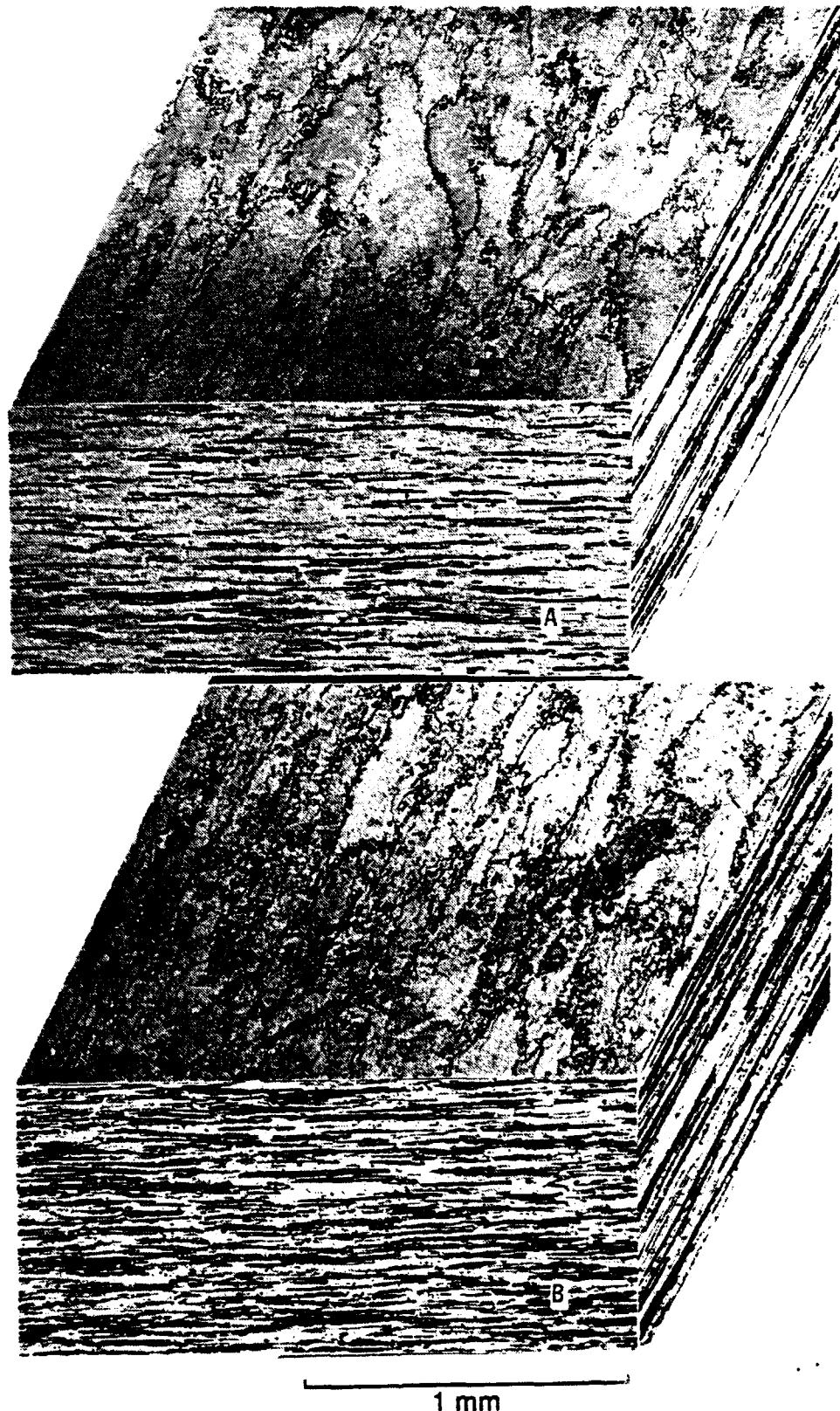
Figure I.3.16. The grain size and morphologies of the two 8090-T3 1/2-
in plates used to make test specimens were similar: (a)
3516 301A, (b) 3518 302A.
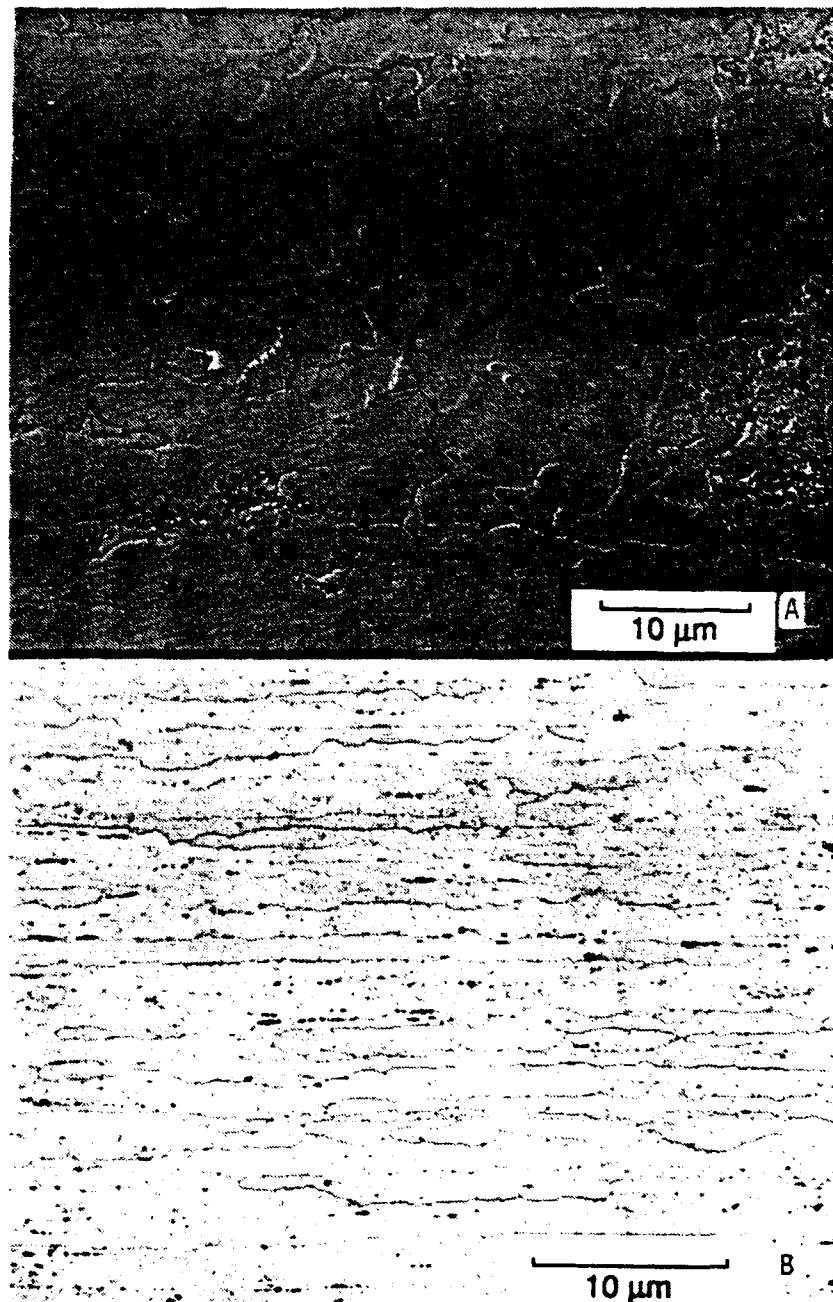
Figure I.3.17. The distribution of inclusions (black dots) in the 8090
plates outlines what was the as-cast structure of the
plate material: (a) 3516 301A, (b) 3518 302A.

1 mm
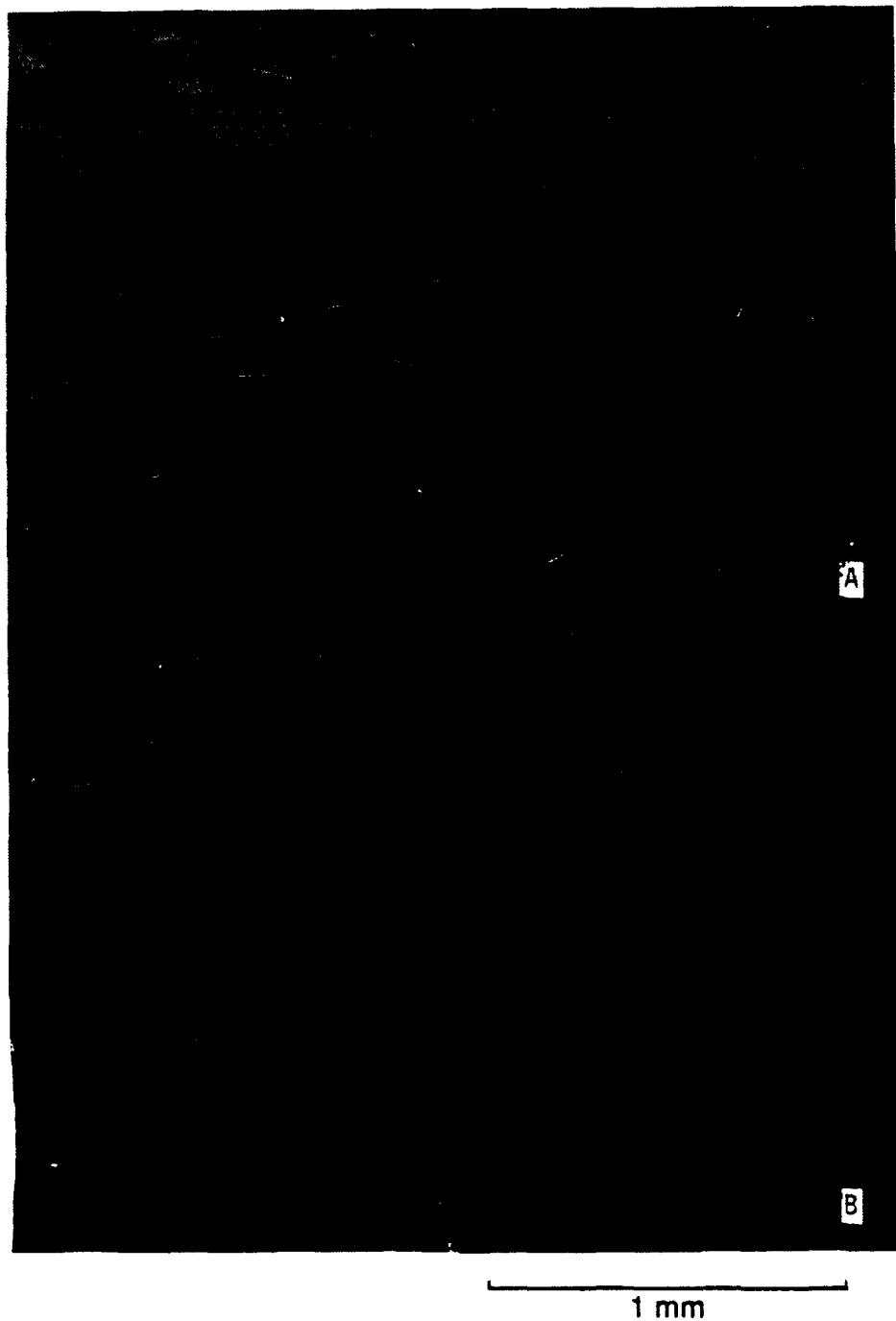
Figure I.3.18. The subgrain structure in the 8090-T3 alloy is pinned, presumably by dispersoid particles. The range in subgrain size and shape is similar to the rolling plane (a) and on planes perpendicular to the rolling direction (b). The larger, more deeply etched particles in (b) are inclusions; most are located at either high- or low-angle grain boundaries.

29

Figure I.3.19. The grain size and morphology of the 2090-T81 1/2-in plate (a) and 3/4-in plate (b).

30
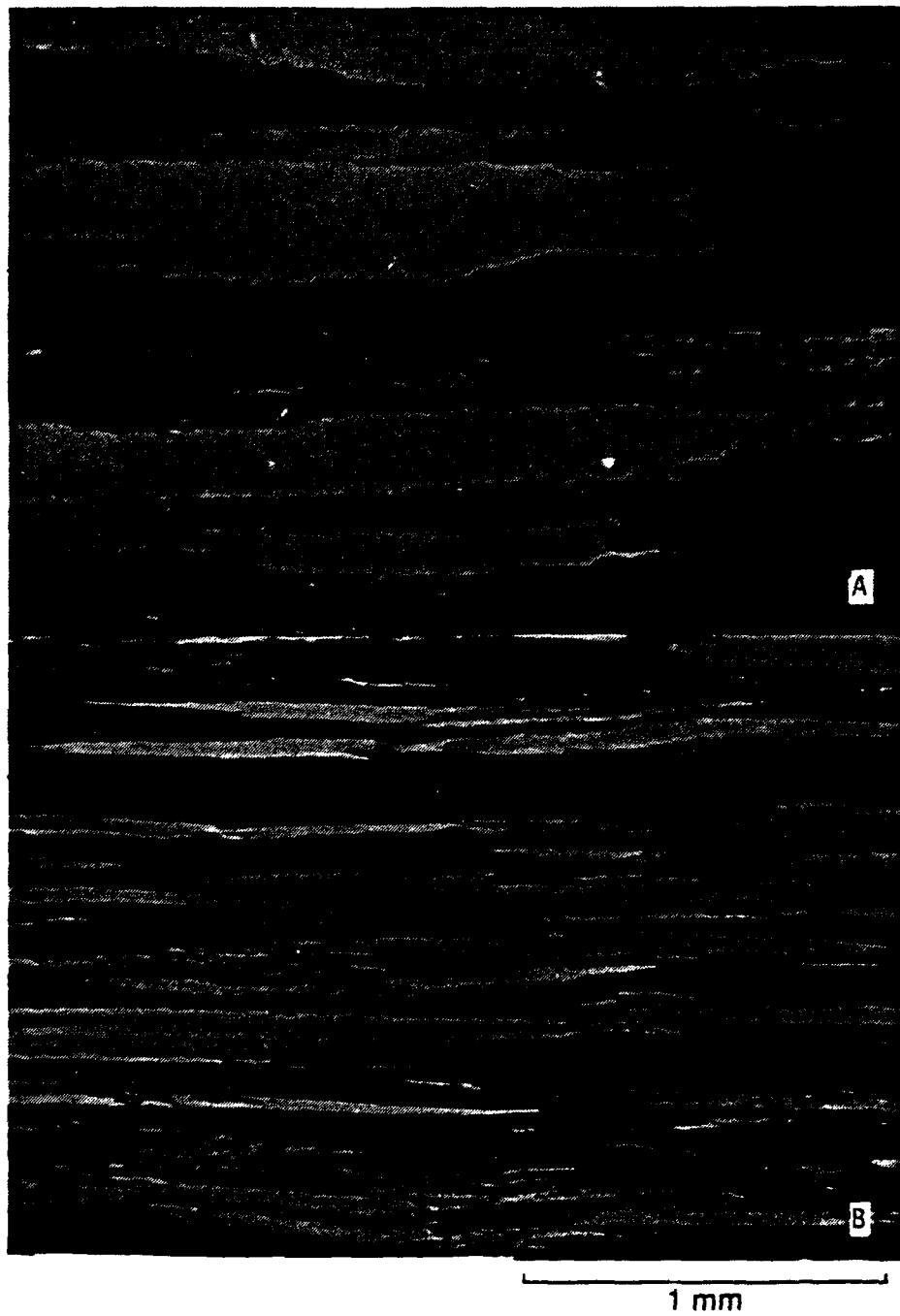
Figure I.3.20. The microstructure of the 2090-T81 1/2-in plate (a) and
3/4-in plate (b) on planes perpendicular to the rolling
direction at approximately a T/4 position.

31

The 2090-T81 alloy has a much larger grain size than the 8090, 2219, or WL049-T351 alloys. The length of the grains ranges from approximately 1 to 3 mm (Figure I.3.19). Also, from Figure I.3.20, it is clear that the grains of the 0.5-in 2090 plate material are much thicker (0.2 mm) than those observed in the 0.75-in plate (0.1 mm). Small recrystallized grains are located almost exclusively at the boundaries between grains in the 0.5-in plate. The 0.75-in plate material has some recrystallization within the grains. The subgrain boundaries in both plates are not visible throughout much of the structure. The inclusion distribution of the 2090 alloy indicates that the solidification structure had more closely spaced dendrites than the 8090 alloy (Figure I.3.21). The inclusion contents of the 2090 and 8090 alloys appear to be similar.

Inclusion counts were only conducted on Al-Li alloys with T8 tempers, so quantitative comparisons are not made at this time for the alloys covered in this interim report. The content, above the size of 1 μm, of inclusions in the 2090-T81 alloy is between 2000 and 3000 inclusions per mm^2. The inclusion size distribution ranges up to 15 μm, but more than 90% of the inclusions are less than 5 μm. Inclusion type has not been determined.

The microstructure of the WL049-T351 alloy has a much larger number of small, recrystallized grains than the 2090 or 8090 Al-Li alloys (Figures I.3.22 and I.3.23). The length of the pancake grains is estimated at 0.8 mm in the rolling plane; however, this may grossly overestimate the effective grain size for the material. The thickness of the grains perpendicular to the rolling plane is 0.4 mm. The inclusion content of the WL049 alloy is higher than that observed for the 2090 or 8090 Al-Li alloys (Figure I.3.24).

The 2219 alloys (T851, T37) have grain lengths ranging from 0.05 to 0.3 mm in the rolling plane (Figure I.3.25). The thickness of the grains is approximately equal to half their length (average grain thickness is 0.05 mm), so, compared to the Al-Li alloys, these grains are only slightly deformed. The inclusion content of the alloys (Figure I.3.26) is most similar to the WL049 alloy and noticeably higher than the 2090 or 8090 alloys. The inclusions are more randomly distributed in the 2219 alloy than in the Al-Li alloys and are usually not located at grain boundaries.
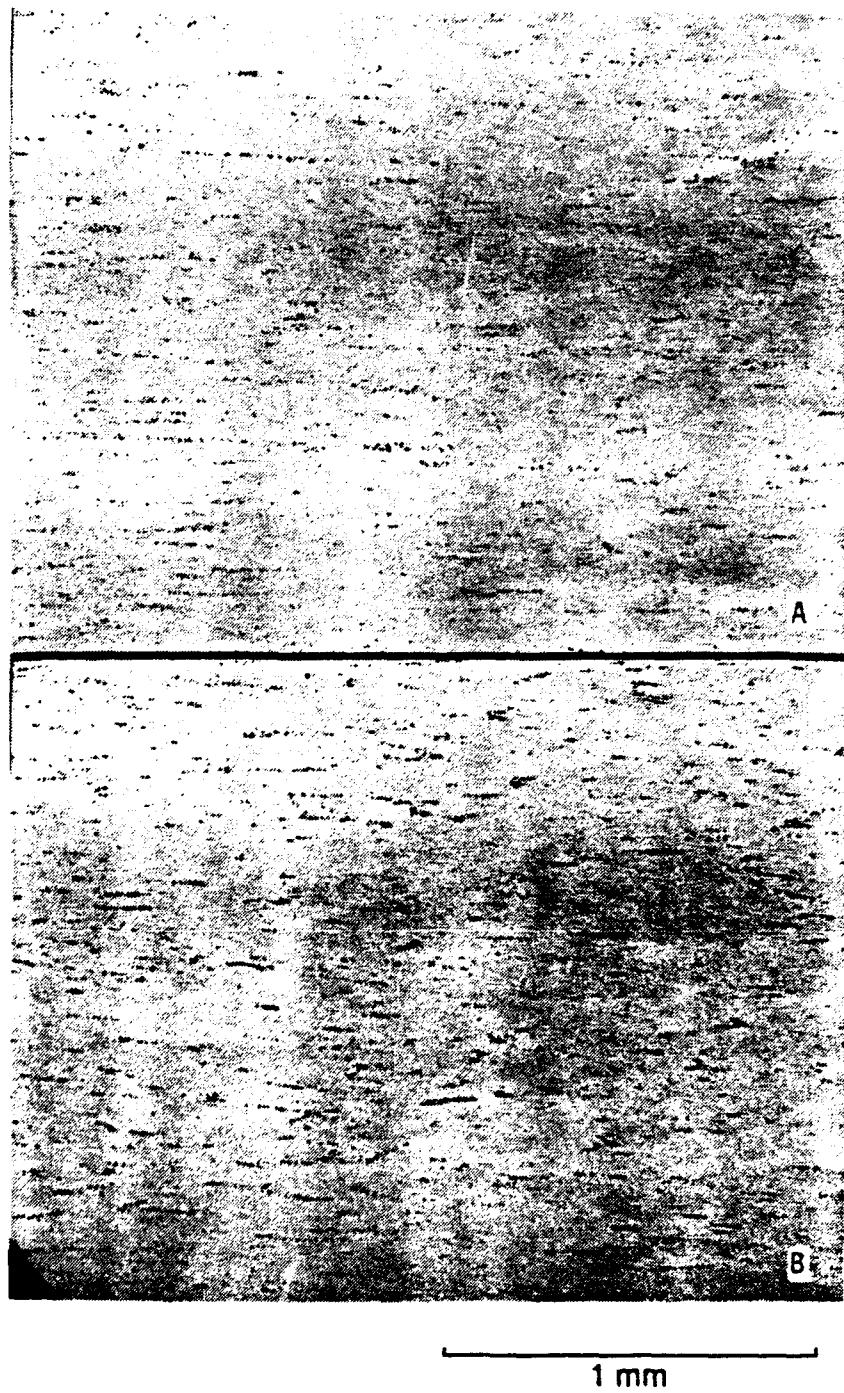
Figure I 3.21. The as-polished appearance of the inclusions in the (a)
2090-T81 1/2-in plate and the (b) 2090-T81 3/4-in plate.

33
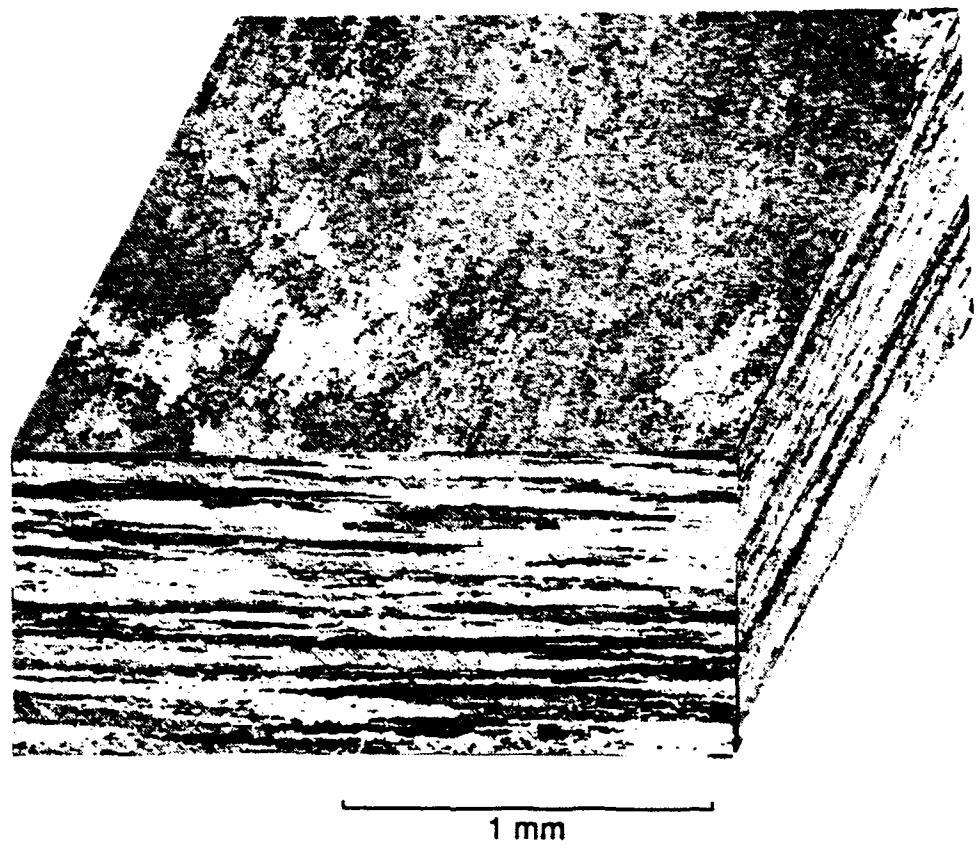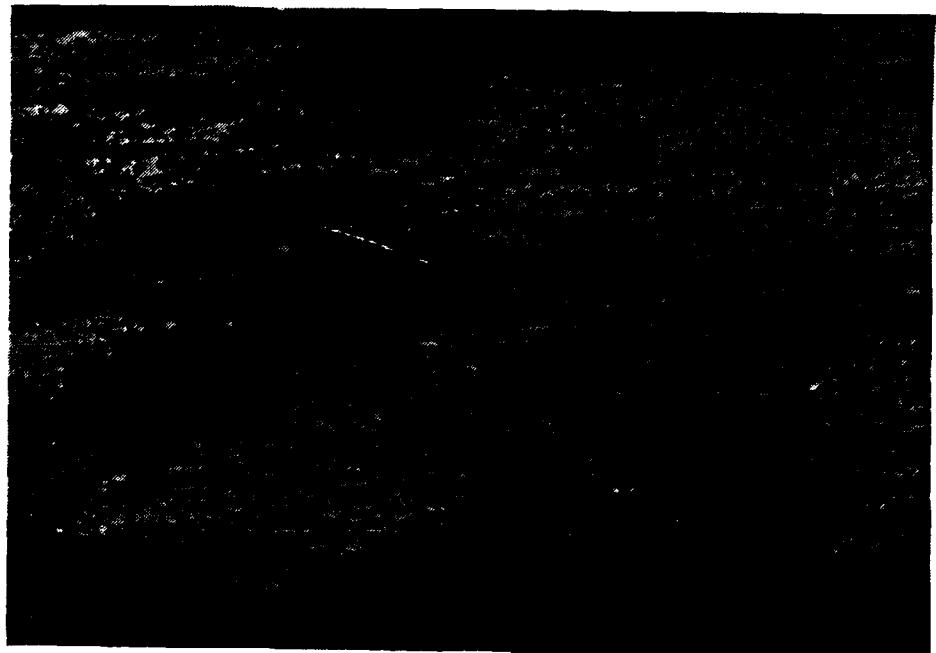
Figure I.3.22. The grain size and morphology of the WL049-T351 alloy.

1 mm

Figure I.3.23. The WL049-T351 alloy has many small, recrystallized grains in its microstruture.
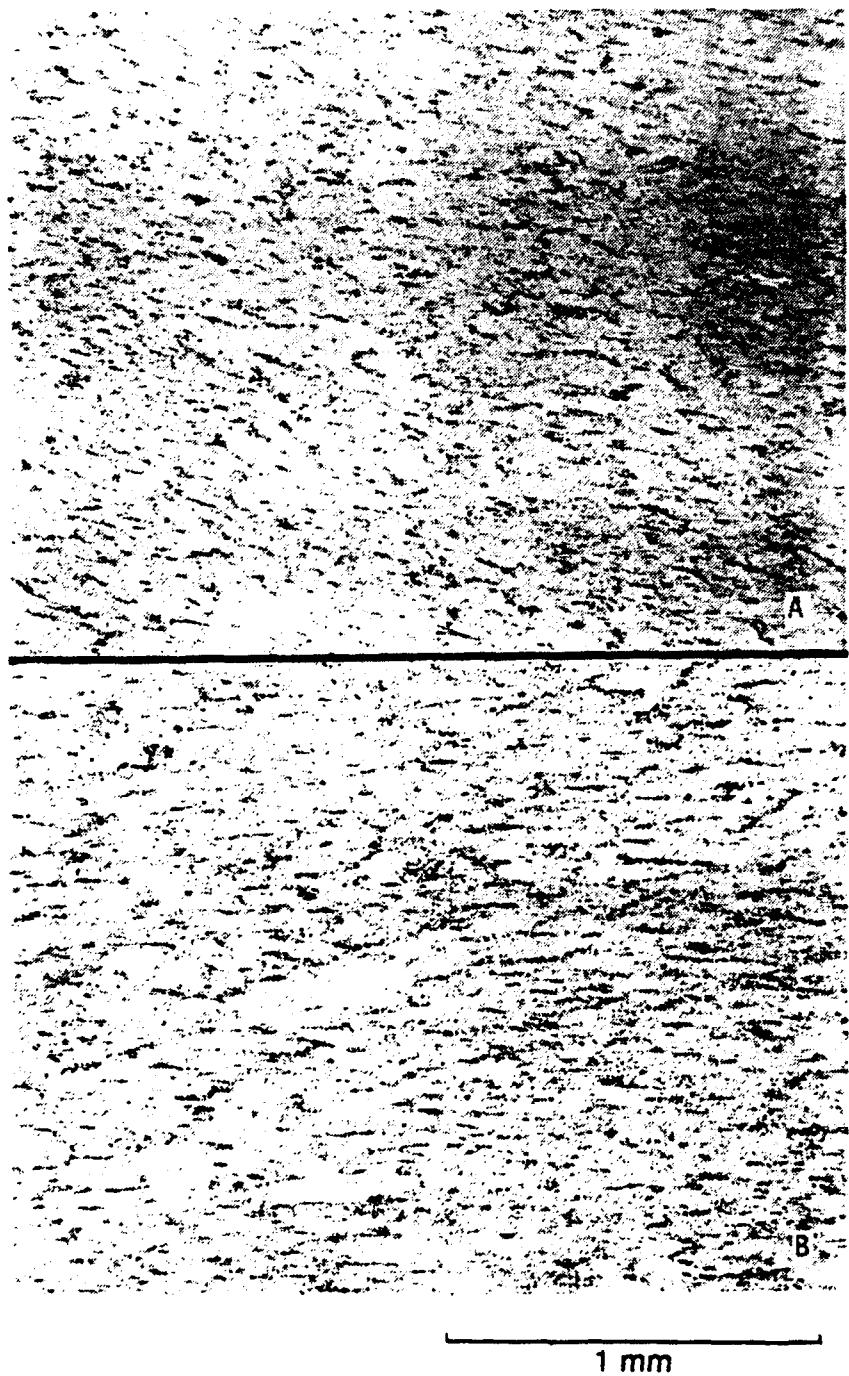
Figure I.3.24. The as-polished appearance of inclusions in the (a)
WL049-T651, and (b) WL049-T351 plates.
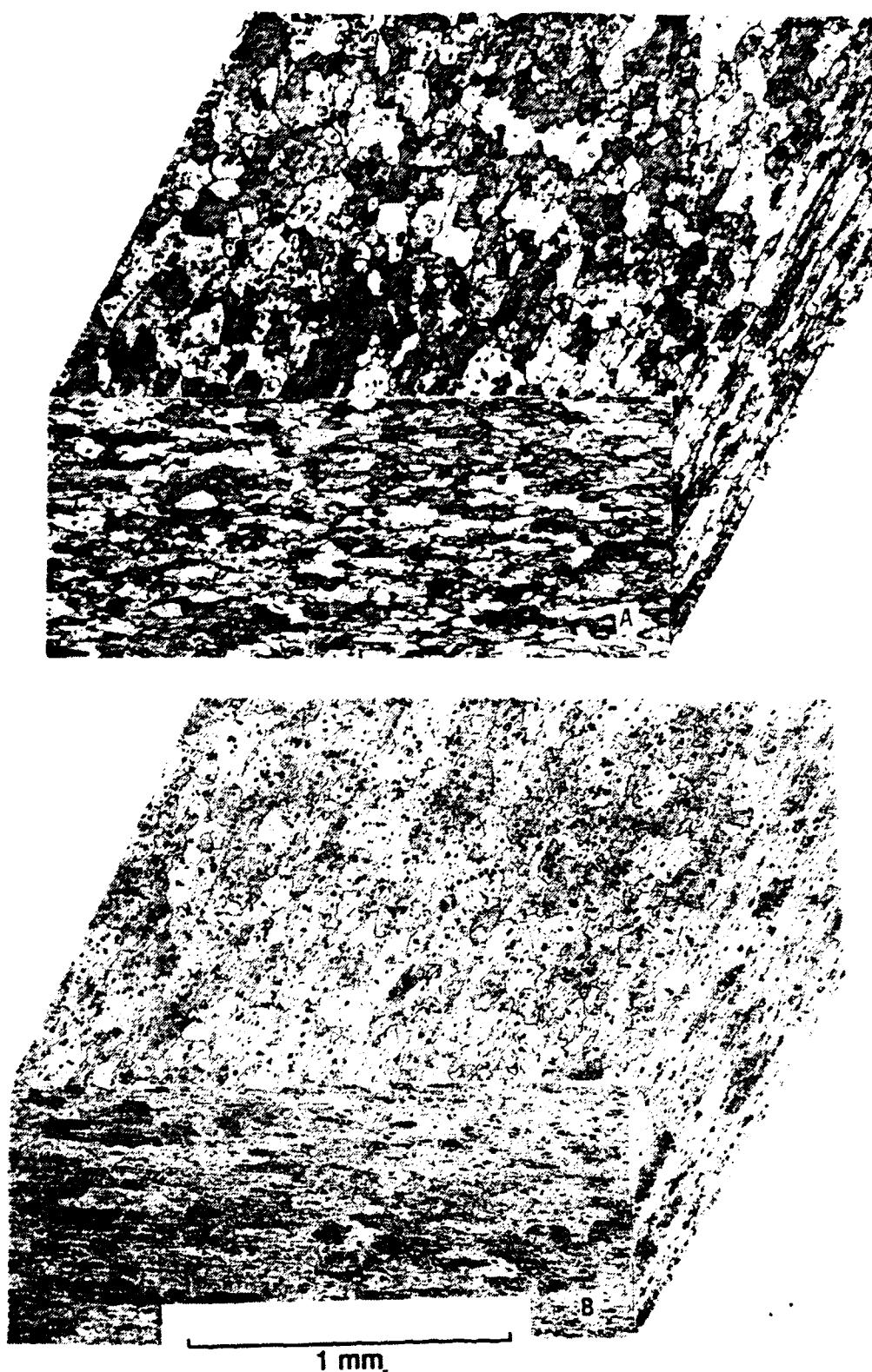
Figure I.3.25. The grain size and morphology of the (a) 2219-T37, and (b) 2219-T851 plates.
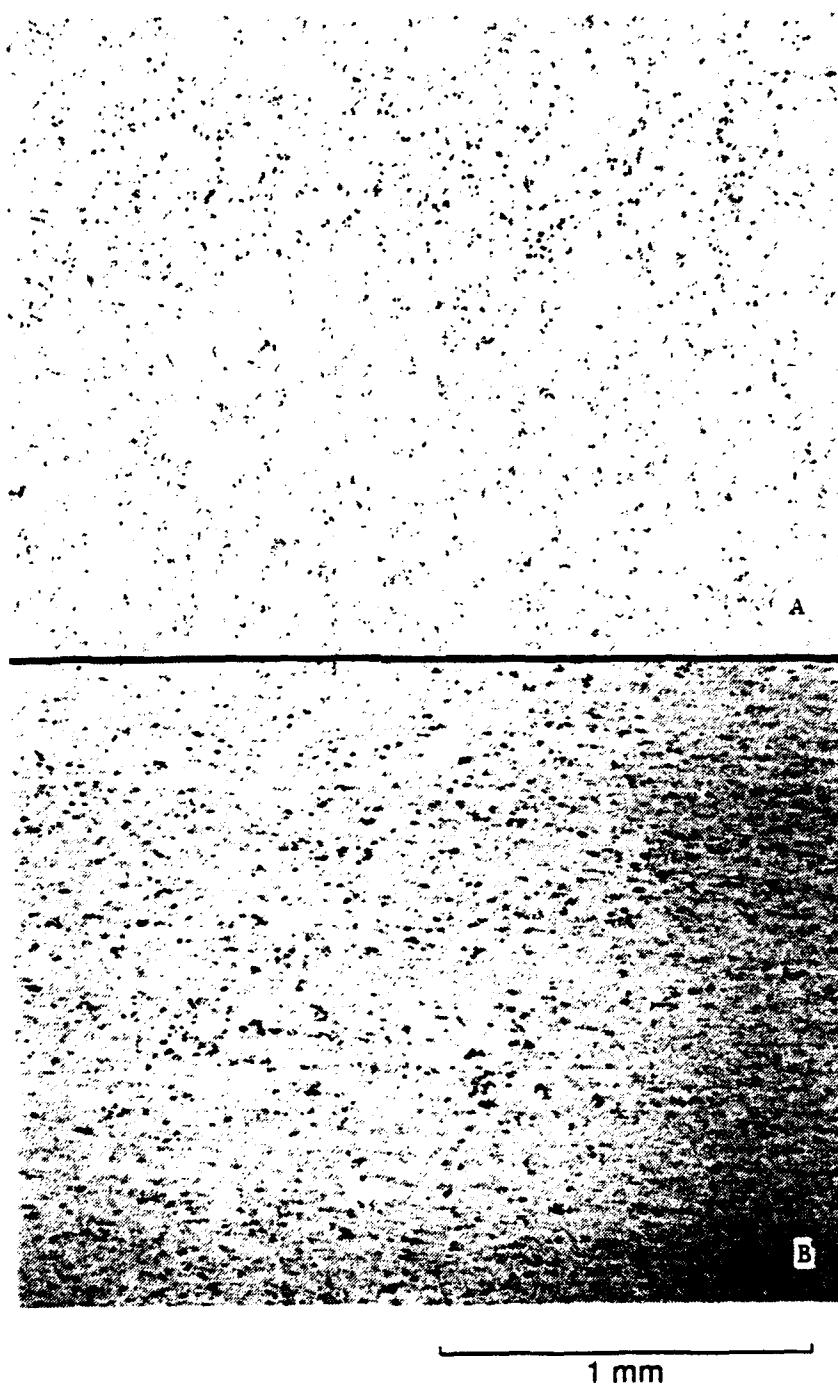
Figure I.3.26 The as-polished appearance of the inclusions in the (a)
2219-T37, and (b) 2219-T851 plates.

I.4. EXPERIMENTAL PROCEDURES

I.4.1. Impact Specimen Preparation

I.4.1.1. Test Specimen Machining and Surface Finish

Test specimens from all alloys were machined to a diameter of 11/16 in and thickness of 1/8 or 1/16 in. Tolerances on the specimen thicknesses were within ± 0.005 in, as specified in NHB 8060.1B[1] (a tolerance on the diameter is not specified in that document). Specimens were machined both from the factory surface and from the center of the plate.

Test specimens were machined from alloys 8090-T3, 2219-T37, and 2219-T851 by a private contractor. The quality of the surface finish was extremely variable. The 8090-T3 specimens had a surface finish in the range of 40—60 μin, and the 2219-T37 and 2219-T851 specimens had a surface finish in the 20—40-μin range. The NASA NHB 8060.1B[1] specification does not call for a tolerance on the surface finish. However, both MSFC and WSTF indicated that the surface quality was poor. Therefore the WSTF shop was chosen to machine the specimens for alloys 2090-T81 and WL049-T351. A sampling of the surface finish from the WSTF shop provided values for 2090-T81 in the 16—20-μin range.

I.4.1.2. Specimen Cleaning Procedure

The machined specimens were cleaned according to NASA NHB 8060.1B,[1] "Flammability, Odor, and Outgassing Requirements and Test Procedures for Materials in Environments That Support Combustion." A copy of the preface of that document and a portion of Paragraph 418, Test 13, relating to specimen cleaning, are found in Appendix I.A.

1.4.2. Open-Cup Mechanical Impact Testing at WSTF

I.4.2.1. Equipment and Procedures

WSTF uses an open-cup mechanical impact tester designed by the Army Ballistic Missile Agency (ABMA) for the evaluation of the LOX impact sensitivity of materials. This equipment has been previously described.[16,17,18]

The ABMA impact tester has a structural frame that consists of three vertical guides that maintain the vertical alignment of the plummet assembly as it falls onto the striker pin. The plummet is a 20-lb (9.09-kg) mass that falls from a maximum height of 43.3 in (1.1 m). The frame is mounted on a 4.0-in (100-mm) thick stainless steel plate, which in turn is mounted on a 2.0-ft (0.6-m) cube of concrete.

The plummet falls freely when released from the height corresponding to the desired impact energy, but is subject to minimal friction from the alignment guides. The drop time of the free-falling plummet is measured just prior to impact to ensure that ± 3% of the calculated totally-free-fall drop time is obtained. The plummet impacts the top of a striker pin of hardened 17-4 stainless steel that rests on the specimen. The plummet rebounds off the top of the striker pin. A rebound catcher is available to

prevent multiple impacts; however, it was not used on these tests.

The steel base plate is precooled to the desired temperature with liquid nitrogen (LN_2). The specimen, an Al specimen cup, a stainless steel cup insert, and the striker pin are precooled in the desired test environment (LOX or LN_2) and are kept submerged in a cryogen tray until ready for testing. These parts are then removed from the cryogen tray (using clean tongs) and installed in the impact machine. Care is taken to ensure that the cup is filled with the cryogen during the installation procedure. The specimen is impacted within 15 to 45 seconds of installation.

After impact, the specimen cup with the specimen, insert, and striker pin are removed from the machine. After every impact the used striker pin is inspected for damage and cleaned following NHB 8060.1B[1] specification procedures. The cup and the insert are discarded and a new cup and insert, cleaned according to specifications, are used for every impact.

The specimens are cleaned and packaged in heat-sealed bags according to NHB 8060.1B[1] and are NOT touched except by clean tongs. Teflon was chosen as the bagging material. The pins, cups, and inserts are touched only with clean tongs or by the rubber or low-lint white nylon gloves approved in NHB 8060.1B. All technicians wear the approved gloves while working in the ABMA test cell. Chances of contaminating the specimen, specimen cup, insert, or striker pin are minimal in the WSTF impact test cell due to safe and clean operating practices.

I.4.2.2. Materials

Six Al-Li and Al alloys, including different tempers and thicknesses, were machined, cleaned, and supplied to WSTF for open-cup oxygen compatibility evaluation. The Al-Li alloys were 8090-T3, 2090-T81 (1/2-in plate and 3/4-in plate), and WL049-T351. The other Al alloys were 2219-T851 and 2219-T37. All alloys except WL049-T351 were machined to provide two thicknesses (1/16 and 1/8 in) for evaluation.

I.4.2.3. Conditions

All alloys have been tested at WSTF in ambient pressure LOX and ambient pressure LN_2 at three impact energy levels: 72, 58, and 43 ft·lbs (10, 8, and 6 kg·m).

I.4.3.   Pressurized LOX and GOX Impact Tests at WSTF, MSFC, and SSFL

I.4.3.1. Equipment and Procedures

The pressurized mechanical impact testers at MSFC and at WSTF are designed to expose material specimens to mechanical impact in the presence of LOX or GOX at pressures from 0 to 10,000 psi (0 to 69 MPa). This equipment has been described previously.[16,17,18] The pressurized equipment at SSFL is identical to that at MSFC described below.

The designs of two testers at MSFC and WSTF are different, but both are similar to the ABMA tester above the test chamber and base plate. Both have

a rigid structural frame that consists of three vertical guides that maintain the vertical alignment of the plummet as it falls onto the striker-pin assembly. The plummet assembly, the plummet hold/release mechanism, and the rebound catcher are similar on both machines. The drop time is monitored for each test at WSTF and MSFC. The similarities end at this point: the designs of the pressurized test chambers and the mounting bases are different. These differences are shown in Figure I.4.1 (MSFC/SSFL) and Figure I.4.2 (WSTF).

The WSTF pressurized tester base differs from the MSFC tester in design and compliance. The WSTF tester uses graphite-filled ball seals whereas the MSFC tester uses Omniseals made of teflon. The specimen is inserted from the bottom of the base in the WSTF tester. In the MSFC tester, the specimen is inserted from above at the point where the base closure section attaches to the base section. The WSTF base is attached to a pedestal mount constructed from 4.25-in diameter x 0.25-in wall pipe, which, in turn is mounted on a 1.0-in thick steel plate that is attached to the floor. The MSFC tester base is attached to a 4.0-in thick steel plate, which sits on a 2 ft x 2 ft x 2 ft cube of concrete that is attached to the floor. The WSTF striker-pin design (long and slender) is more compliant than the short, stout design in the MSFC tester. The MSFC tester uses a one-piece cup where the WSTF tester uses a 3-piece cup design. Both testers utilize a balance chamber design in order to equalize the pressure between the test chamber area and the balance piston area.

The test procedures are somewhat different. The WSTF specimens and striker pin are first precooled in LOX (for LOX testing). The LOX-filled cup with specimen and precooled striker pin are installed in the room-temperature impact machine. The test chamber is pressurized and the specimen impacted within 15 to 45 seconds of installation. A thermocouple is attached inside the test chamber allowing the operator to verify the test temperature (nominally 113 K) before the test and to note the temperature within the chamber during and following impact. This thermocouple is located inside the cup, approximately 0.060 in above the specimen. Also located within the test chamber is a photocell used to detect flashes that may occur during impact.

At MSFC, the cup, specimen, and striker pin (all at room temperature) are installed after the machine base has been cooled to 77 K with continuously flowing LN_2. The test chamber is pressurized using GOX. The pressurized system is held for 2 min to allow the gaseous oxygen to condense and the pressure to stabilize before the specimen is impacted. The temperature is monitored in the precooled base by a thermocouple installed within the block at a distance of about 0.090 in from the test chamber wall. This block temperature, which is noted and recorded at the time of plummet release, typically ranged from 113 to 123 K during this series of tests. At SSFL, the location of the thermocouple is the same as at MSFC. .The detector for ob·erving flashes is not used at MSFC. However, the procedures for oxygen pressurization and cooldown are different. The specimen, cup, and striker pin are at room temperature when installed in the test block. The test chamber is evacuated and purged with GOX three times before cooldown of the machine base with LN_2 begins. Gaseous oxygen flows into the test chamber during the cooldown, which typically requires about 25 min. When the thermocouple indicates the temperature has reached 122 K, the plummet is released.
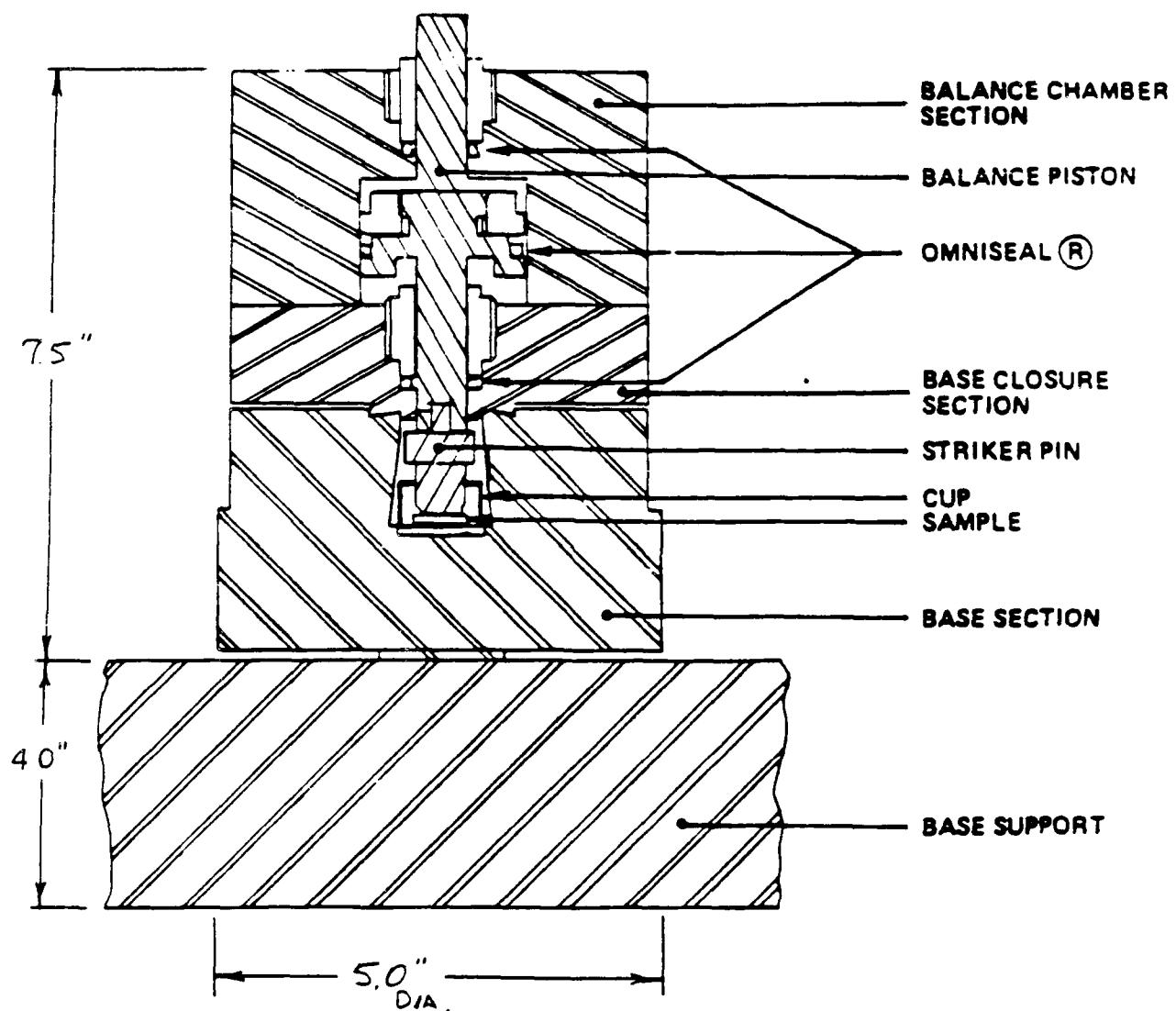
Figure I.4.1. MSFC/SSFL high-pressure tester detail. (Not to scale.)
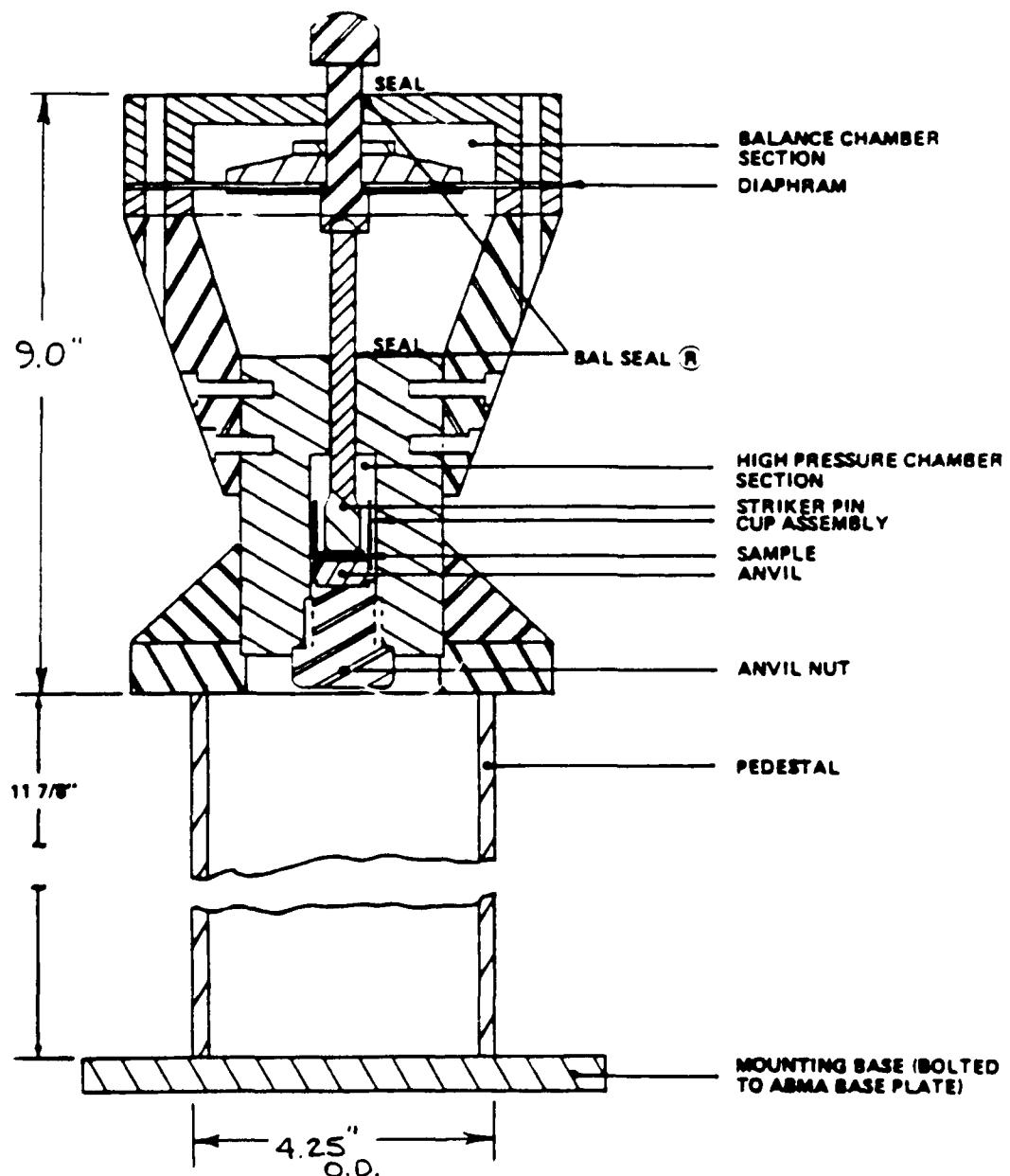
Figure I.4.2. WSTF high-pressure tester detail.   (Not to scale.)

43

The test temperatures monitored by the thermocouple at both MSFC and SSFL are within about 10 K of 113 K and the actual specimen temperatures are also probably quite similar, to within about 10 K, since the design of the test systems is identical. However, because the WSTF thermocouple is located in the test chamber, very close to the specimen, it represents the actual specimen temperature more accurately. At both MSFC and SSFL, the temperature reported by the thermocouple (located in the block) is intermediate between the true specimen temperature and the temperature at the heat sink of the machine base (about 77 K).

At WSTF, the specimens, cups, and striker pins are handled only with clean tongs or LOX-approved clean gloves per NASA specification NHB 8060.1B, Appendix C, Section 4.4.[1] A fresh three-piece cup and striker pin are employed for every sample, and the previously used pin and cup are inspected, cleaned and packaged before reuse. Specimens impacted at WSTF were packaged in heat-sealed teflon bags before installation in the tester.

At MSFC the specimens and cups are also only handled with clean tongs. The striker pins are handled using Kimwipe tissues. The striker pin and cup are replaced after every impact with a clean pin and cup. Specimens impacted at MSFC were packaged in heat-sealed teflon bags before installation in the tester.

Table I.4.1 (adapted from Ref. 18) summarizes the similarities and differences between the WSTF and MSFC pressurized impact testers. This table also includes comparable information on the SSFL pressurized impact tester, because results of a few tests from SSFL are reported in Section I.5. Both WSTF and SSFL have provisions for detecting flashes (a flash is accepted as a reaction under NASA NHB 8060.1B), but MSFC currently does not. Specimens impacted at SSFL were packaged in heat-sealed ACLAR bags before installation in the tester; effects of differences in specimen packaging material are addressed in Section I.5.4.

I.4.3.2. Materials

Six Al-Li and Al alloys, including different tempers and thicknesses were machined, cleaned, and supplied to WSTF and MSFC for open-cup oxygen compatibility evaluation.

The Al-Li alloys were 8090-T3, 2090-T81 (1/2-in plate and 3/4-in plate), and WL049-T351. The other Al alloys were 2219-T851 and 2219-T37. The WL049-T351 (machined to 1/16-in thick) was supplied only to WSTF. All alloys except WL049-T351 were machined to provide two thicknesses (1/16 and 1/8 in) for evaluation. Al-Li alloy 2090-T81 was supplied to SSFL in 1/8-in thick specimens by ALCOA for pressurized LOX-compatibility evaluation. Results of this testing program are included here through the courtesy of ALCOA.

I.4.3.3. Conditions

At WSTF tests were conducted at 500-psi pressure in LOX and GOX environments with a nominal impact energy of 72 ft·lbs. All alloys and tempers were tested as both 1/8- and 1/16-in thick specimens, except WL049-T351, which was tested using only 1/16-in specimens. The materials tested were 8090-T3, 2090-T81 (1/2- and 3/4-in-thick plates), WL049-T351,

Table I.4.1. High-Pressure Impact Tester Comparison[17]

		WSTF	MSFC	SSFL
Apparatus:				
A.	Pins			
	Material	17-4-SS	Inconel 718	Inconel 718
	Hardness	R_c43–45	R_c43–45	R_c36–45
	Diameter	0.500 in	0.500 in	0.500 in
	Change	Every drop	Every drop	Every 20 drops
	Shaft dia.	0.375 in	0.625 in	0.625 in
	Shaft length	$5.00 \pm {}^{0.000}_{0.100}$ in	0.590 in	0.590 in
B.	Cups			
	Material	Inconel 718	Inconel 718	Inconel 718
	Hardness	R_c43–45	R_c43–45	R_c43–45
	Inside Dia.	0.765 (ring) in	0.750 in	0.750 in
	Design	3 piece	1 piece	1 piece
C.	Base			
	Size	N/A (anvil nut)	4-in-thick steel	4-in-thick steel
	Mounting	Cylindrical pedestal to floor	concrete block	concrete block
D.	Plummet			
	Weight	20 lbs	20 lbs	20 lbs
	Drop	Free fall	Free fall	Free fall
	Rebound catcher	Yes	Yes	Yes
E.	Seals	2–15% graphite Filled ball seals	3 Omniseals teflon for low temperatures, 15% graphite filled for RT and above	3 Omniseals teflon and moly filled TFE

Table I.4.1. continued

		WSTF	MSFC	SSFL
Measurement and pressure control:				
A.	Temperature	TC in chamber	TC 0.090 in from wall	TC 0.090 in from wall
		TC/strip chart	TC/digital readout	TC/digital readout
B.	Pressure (readout)	digital	gage	—
C.	Pressure (control)	regulator	regulator	—
D.	Plummet speed	timer	timer	timer
Temperature control:				
A.	Base	none	continuous LN_2 flow	LN_2
B.	Precool sample, cup, pin	LOX (submerged)	No	No
C.	Temperature control of sample in base	none	condensed GOX	condensed GOX
D.	Hold time (after installation)	none	2 minutes	25 minutes cooldown
Cleaning:				
A.	Cups, pins, block	Freon	F-33 (O_2 compatible soap)	Freon
B	Sample	NHB 8060.1B 4.6-4.7 (soap, deionized H_2O, GN_2	F-33/ Distilled H_2O/Freon (Dry 150 °F overnite)	Freon (material dependent
C.	Packaging	Heat sealed teflon	—	Heat sealed ACLAR
Cleaned parts handling:				
A.	Pins/cups	cleanroom gloves	Kimwipes	—
B.	Samples	tweezers	tweezers	tweezers

2219-T851, and 2219-T37.

Tests at MSFC were carried out only in LOX (tests in GOX at MSFC are pending at this time) with a nominal impact energy of 72 ft·lbs (10 kg·m). Alloy 8090-T3, in 1/16-in thickness, was tested at 50 and 100 psi. Alloy 2090-T81, from 1/2-in plate, was tested in 1/16-in thickness at 100 and 500 psi, and in 1/8-in thickness at 50, 100, and 500 psi. Alloy 2090-T81, from 3/4-in plate, was tested in 1/16-in thickness at 500 psi and in 1/8-in thickness at 50, 100, and 500 psi. Alloys 2219-T851 and -T37 were tested in 1/16-in thickness at 500 psi.

The SSFL testing was performed in a pressurized LOX environment (100, 400, and 1000 psi) on alloy 2090-T81 (1/2-in plate). All the specimens were 1/8-in thick and were impacted with an energy of 72 ft·lbs (10 kg·m). Results and specimens were supplied by ALCOA.

I.4.4. Equipment Calibration

Early in this program it was recognized that there were significant differences in the relative impact depths in test samples run in the different testers. A method previously used by Bransford et al.[18] was employed to better assess those differences and to compare the tester variability. The intent of this effort is not to relate overall relative impact energies in the different testers, but rather to compare and verify recent impact depths with those reported ten years ago in the Bransford report.

Disks were fabricated from AISI 304 stainless steel rod. The disk thicknesses were 0.500 in (12.7 mm) and 0.350 in (8.89 mm) with a diameter of 0.6875 in (17.46 mm). The disks were annealed to R_B80 to remove work hardening and to produce uniform hardness.

The striker pin was modified by machining its flat tip to form a 0.500 in (12.7-mm) diameter hemisphere so that, when impacted, a spherical-type indentation is made in the 304 disk. The resulting impact diameter is measured, which is then converted to impact depth, using the following equation:

$$F(D) = [d(mm)]^2 = 80.645 - 0.25D^2 - 12.7(40.3225 - 0.25D^2)^{1/2} \quad (4-1)$$

where D = dent diameter, mm and d = penetration (impact depth), mm.

The indentation tests were conducted without sample cups (except as noted) and using the rebound catcher. Disks were impacted in LOX and at ambient temperature, and at elevated as well as ambient pressures. Test results are shown in Table I.4.2. The data are discussed below.

One note of caution: Bransford et al. report the use of 0.350-in thick specimens; the Bryan paper[16] reports the use of 1/2-in thick specimens for the same calibration data. We think that the Bransford information is correct and the following discussion reflects this.

I.4.4.1. Friction

One consideration is the effect of friction from the seals of the pressurized equipment on the absorbed energy (penetration depths). The earlier work by Bransford et al. had indicated very little effect of friction in the MSFC and SSFL equipment. The MSFC data in Table I.4.2 indicate no frictional losses when the tests are conducted at 500 psi.

I.4.4.2. Temperature

Testing at low temperatures under ambient pressure was shown by Bransford et al. to reduce penetration depths by 40% when the ABMA tester is used at MSFC and by 50% when the pressurized tester is used at MSFC. Data in Table I.4.2 suggest that the reduction in penetration depth (for AISI 304) when testing at low temperature with the WSTF equipment is about 20% at ambient pressure.

I.4.4.3. WSTF/MSFC Comparison

Bransford et al. have reported (for 0.350-in thick 304 specimens) that the penetration depths from WSTF were about 25% less than those from MSFC for the pressurized equipment at ambient temperature and pressure. Data in Table I.4.2 also show a reduction of depths of about 25% at ambient temperature and pressure for 0.50-in thick 304 specimens. Thus, for ambient conditions, the specimen absorbed energy distinctions between the two laboratories are much less than at low temperatures.

Comparison between the WSTF ABMA equipment and MSFC pressurized equipment was initially puzzling. Our data in Table I.4.2 indicate that the WSTF ABMA equipment produces about 15% less specimen absorbed energy than the MSFC pressurized equipment. We now attribute these results to the use of Al specimen cups in the WSTF equipment; this should result in increased resiliency and higher rebound heights in the WSTF tests.

I.4.4.4. Open Cup/Pressurized Equipment at WSTF

Even at ambient temperature and pressure, the penetration depths from the pressurized WSTF equipment are 10—20% less than the open-cup depths. At LOX temperature and ambient pressure, the penetration depths of the pressurized tests are almost 30% less than those of the open-cup tests.

Clearly, the number of tests were insufficient to place confidence in the quantitative percentages calculated in the above discussion. But, despite the low number of tests, the results are closely consistent with the earlier study of Bransford et al. The data do support the following conclusions: (1) The MSFC pressurized equipment delivers more absorbed energy to the specimen than do the ABMA and pressurized equipment of WSTF. (2) Tests at low temperatures produce less absorbed energy than tests at room temperature for equivalent conditions. (3) The pressurized equipment at WSTF produces less absorbed energy in specimens than does the ABMA equipment at WSTF, even at ambient temperature and pressure.

Table I.4.2 Calibration Block Results.

Facility	Machine	Energy Level, kg·m (ft·lb)	Block Thickness, in	Pressure, psi	Temperature	Penetration Diameter, mm (in)		Penetration Depth, mm (in)	
WSTF	open cup	10 (72)	0.500	ambient	ambient	7.640	(0.300)	1.278	(0.0503)
WSTF	pressurized	10 (72)	0.500	ambient	ambient	7.259	(0.286)	1.142	(0.0450)
WSTF	open cup	10 (72)	0.350	ambient	ambient	7.925	(0.312)	1.388	(0.0546)
WSTF	open cup	10 (72)	0.350	ambient	LOX	7.239	(0.285)	1.132	(0.0446)
WSTF	pressurized*	10 (72)	0.350	ambient	ambient	7.163	(0.282)	1.105	(0.0436)
WSTF	pressurized*	10 (72)	0.350	ambient	LOX	6.223	(0.245)	0.815	(0.0320)
MSFC	pressurized	10 (72)	0.500	ambient	ambient	8.204	(0.323)	1.503	(0.0592)
MSFC	pressurized	10 (72)	0.500	500	ambient	8.204	(0.323)	1.503	(0.0592)

*Calibration testing carried out with a Ni-based alloy cup. All other tests reported in this task were carried out without a cup.

I.4.5. Promoted Combustion Tests at WSTF

The promoted combustion test procedures are outlined in Appendix I.B, and are also discussed by Steinberg, Packer, and Beeson.[19]

I.5 EXPERIMENTAL RESULTS

I.5.1. Fracture and Deformation Modes: Common Features

In mechanical impact tests of Al alloys, the impact of the striker pin can result in splitting, cracking, delamination, and several types of localized shearing. The general sequence of modes is reasonably clear, although some of these deformation and fracture modes probably occur simultaneously.

I.5.1.1. Shear-Lip Formation

At impact, the specimen undergoes a gross diameter change if there is insufficient material outside the impacted region to offset the large radial tension stresses that result from the compression. As penetration of the striker pin into the specimen continues during impact, the diameter of the specimen is anisotropically increased further and the shear lips shown in Figure I.5.1 are formed. The position of the striker pin at its maximum penetration depth into the specimen is defined by the smaller diameter circle at the bottom edge of the shear lip. Ideally, if the striker pin impacts dead center on the specimen, a shear lip would form uniformly around the circumference of the penetration. If the striker pin impacts the specimen off-center (eccentric strike), there is less material surrounding the compression zone in some regions to resist deformation and shear lips are formed locally as shown in Figure I.5.1c.

The orientation of the shear lip, however, is not always determined by the position of the impact alone. The highly textured microstructure of the Al-Li alloys also influences the anisotropic nature of the local deformation. Specific examples of local deformation for the 2219, 2090, 8090, and WL049 alloys are discussed in Section I.5.3.2. of this report.

I.5.1.2. Splitting

The 2090-T81 specimens often split during LOX testing. In Figure I.5.2, a typical split is shown from several perspectives. As circumferential forces develop, due to the increase in the diameter of the specimen during impact, the specimens locally crack in tension and split at their outside diameters. The assertion that most splits originate near the outside diameter of the specimen is supported by the observation that many specimens have splits that do not even reach the impacted area. However, several specimens (Figure I.5.2d) have splits that may have started at cracks formed in the impacted zone. In either case, the splits propagate in the rolling direction and the failure is predominantly intergranular (Figure I.5.3a). This mode of failure exposes large areas of unoxidized surface to the oxygen environment. Commonly, the intergranular failure or delamination results in a step-like fracture surface that traverses the thickness of the specimen and forms a slanted fracture surface (Figure I.5.2d).

Splitting can occur very early during the impact. Striation marks,

51
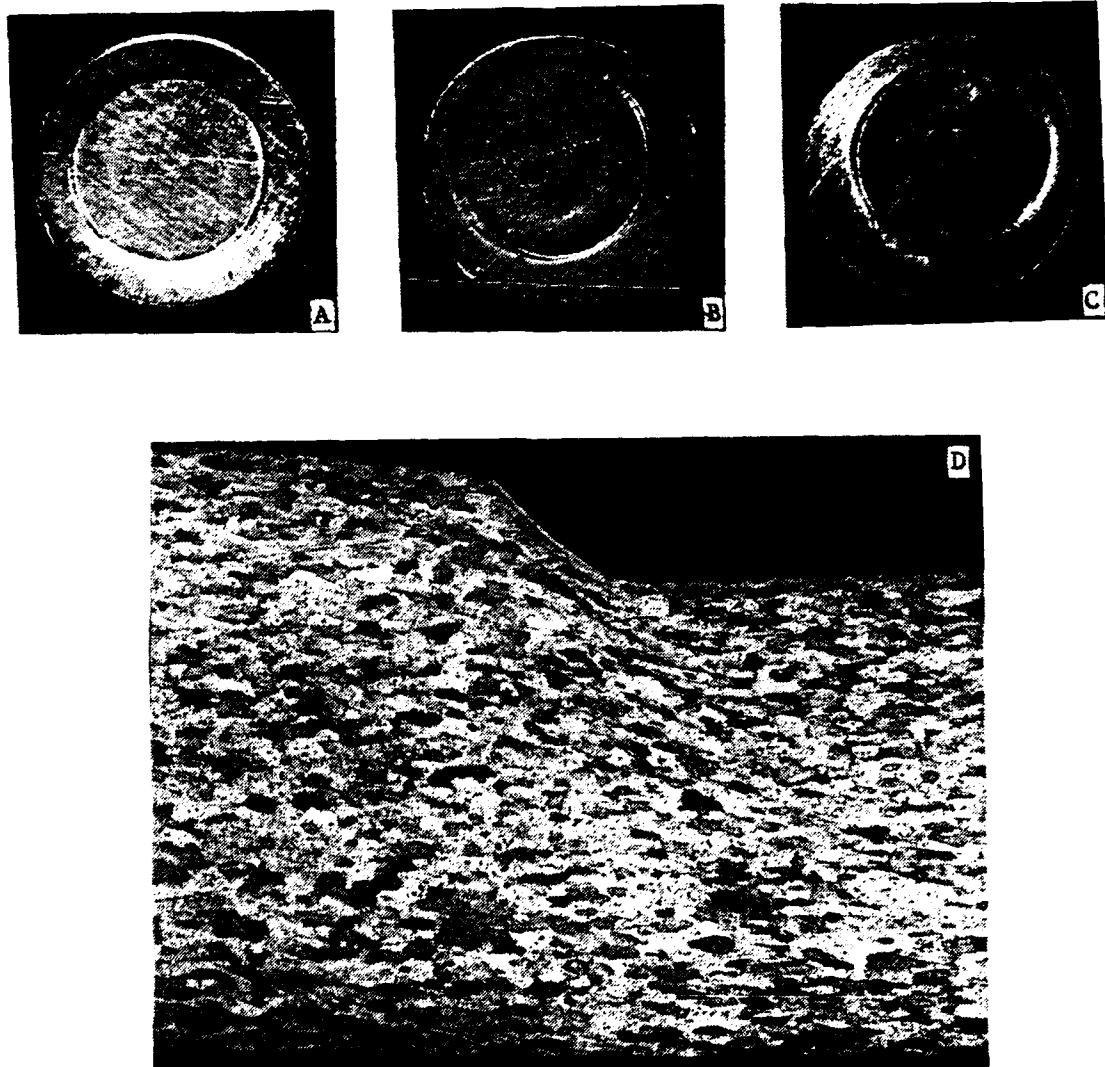
Figure I.5.1. The shear face formed during the 500 psi (LOX) testing
on the (a) 2219-T851, #20, 1/16-in specimen, (b) the
2219-T37, #17, 1/16-in specimen, (c) the 8090-T3, #2,
1/16-in specimen. In (d), a cross section of the shear
face for the 2219-T37, #10, 1/16-in specimen is shown.
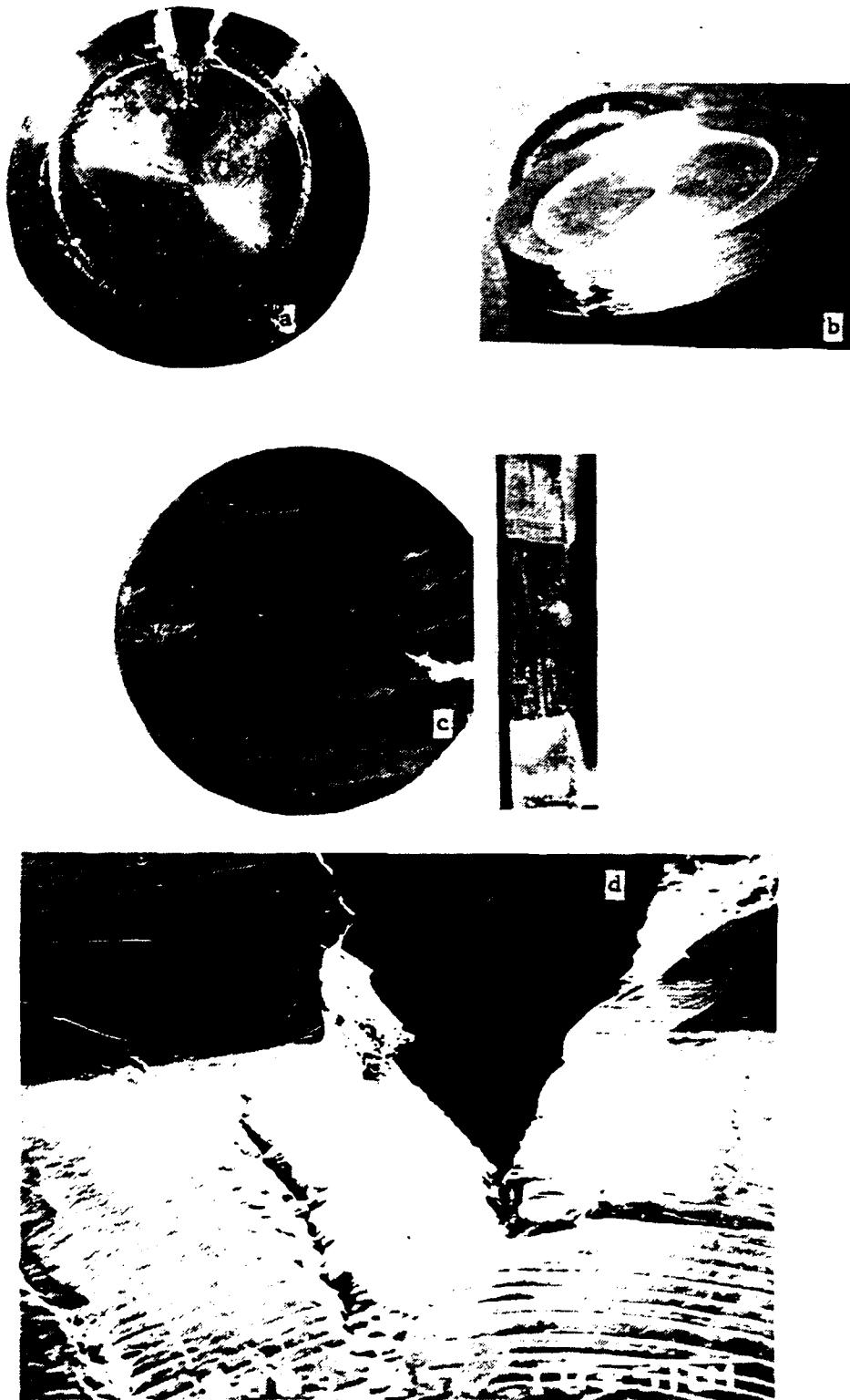
Figure I.5.2. The split morphologies characteristic of the 2090-T81 alloy: (a) top view showing split and shear face, (b) orthogonal view showing slant fracture through the specimen thickness, (c) plane polished near the cup side of the specimen showing orientation of split to the grains. In (d), cracking in the impacted zone that may lead to splitting is shown.

53
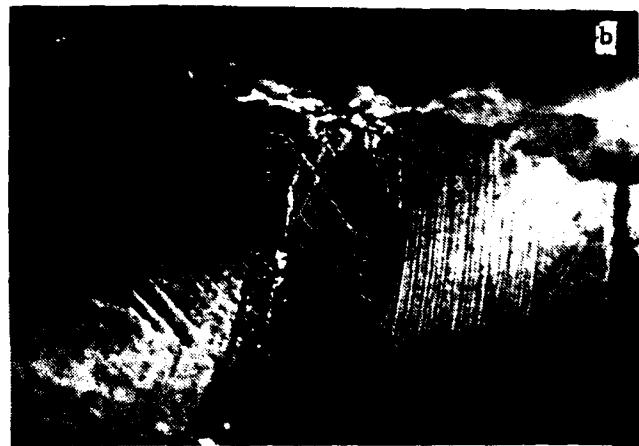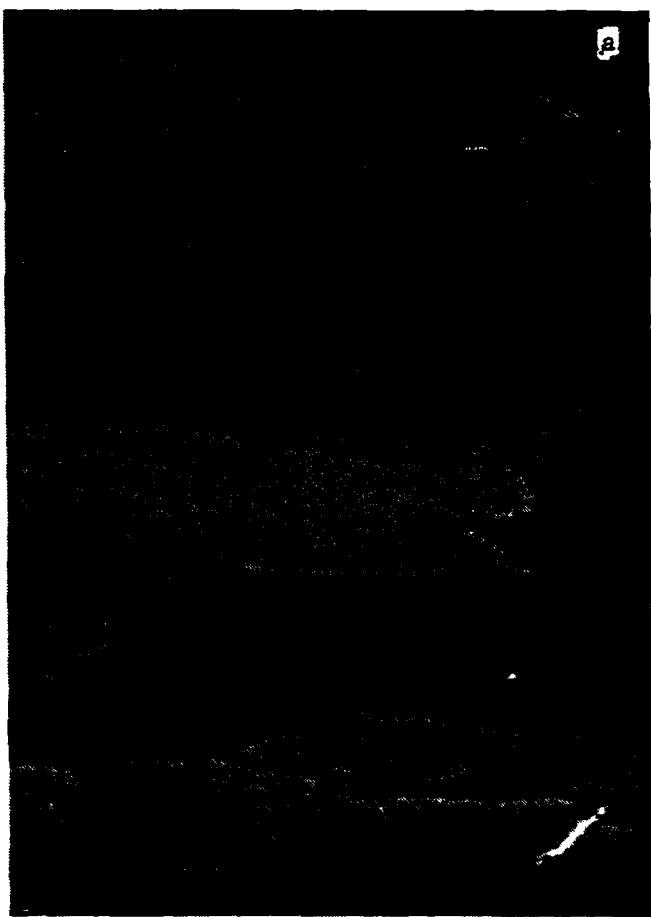
Figure I.5.3. The fracture during splitting in 2090-T81 is
intergranular. In (a), a cross section perpendicular to
the direction of splitting and the rolling direction is
shown. In (b), striation markings on a shear face and
cracking at the bottom of the shear face are shown.

left by the striker pin on the shear face in Figure I.5.3b, show a change in direction that identifies when this split occurred. As the specimen splits, it moves relative to the striker pin as the split opens. In this case, (Figure I.5.3b), splitting occurred soon after the initial impact.

I.5.1.3. Cracking

Cracks are most often found either on the outside diameter of the specimens where tensile stress is high, or within the impacted region of high compressive stress, or at the interface between the two. We leave the last two cases until the flow of material under the striker pin is discussed in the next section.

Cracking on the circumference of the 2219-T851 specimens, shown in Figure I.5.4, is accompanied by local extrusion of material. These surface cracks do not generally penetrate very far into the bulk of the specimen, but an oxide-free surface is exposed to the oxygen atmosphere during the process.

I.5.1.4. Deformation Under the Striker Pin—Adiabatic Shear

The flow of material under the striker pin during impact is extensive. For example, just under the impacted surface of the 2090-T81 specimen shown in Figure I.5.5a, the microstructure has been displaced dramatically by what appears to be an almost fluid-like flow process. Bands of intense local deformation (Figures I.5.5b and I.5.5c) follow the same general circular morphology as the microstructure and indicate the presence of adiabatic shear. In these regions, shear strain that would normally result in hardening, occurs so rapidly that the heat generated results in softening. This promotes further local shearing that is accompanied by more heat generation (90—95% of the deformation can be converted to heat as the temperature approaches ambient). The process is self-feeding and can lead to localized melting.

Much of the cracking visible in Figure I.5.5 is intergranular and often is linked to the adiabatic deformation bands. Cracking is also observed around the circumference of the compression zone (Figure I.5.5a) where the microstructure has been displaced in the through-thickness direction (Figure I.5.5d) as well as in the plane of rolling.

I.5.1.5. Microreactions

During examinations of the impacted specimens, small reacted areas were sometimes found on specimens from MSFC and SSFL. These areas are often not visible with the naked eye, so we refer to them as microreactions.. They most likely represent local melting, followed by oxidation that is rapidly suppressed by an unfavorable heat transfer balance. The most common site of microreactions was at the bottom of the shear lip where the striker pin reaches its maximum penetration into the sample. In Figure I.5.6, a microreaction observed on a 2090-T81 specimen, tested at 100 psi (LOX) is
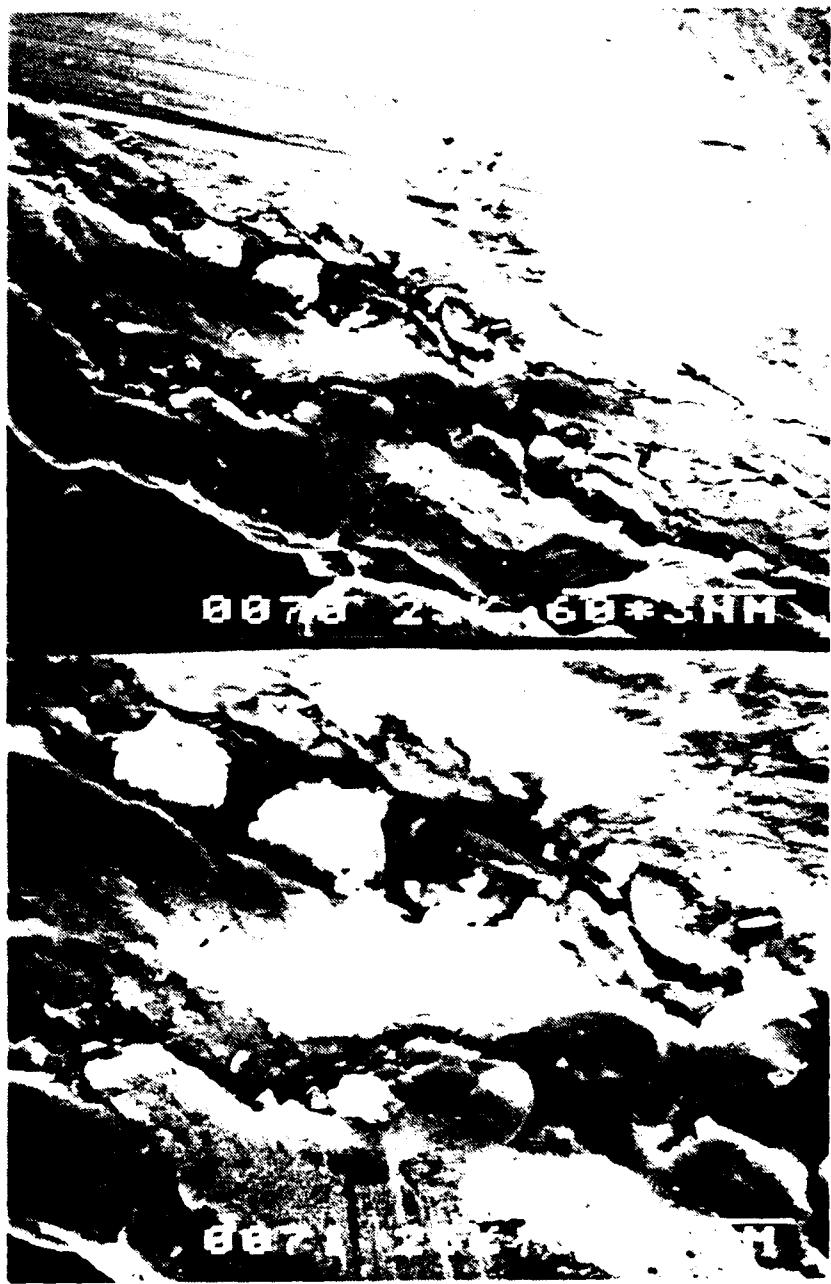
Figure I.5.4. On the outside diameters of the 2219-T851 specimens,
cracking was observed.

Figure I.5.5a. The "fluid-like" flow of material observed in 2090-T81
specimen on a plane polished very near the impacted
surface of the specimen.
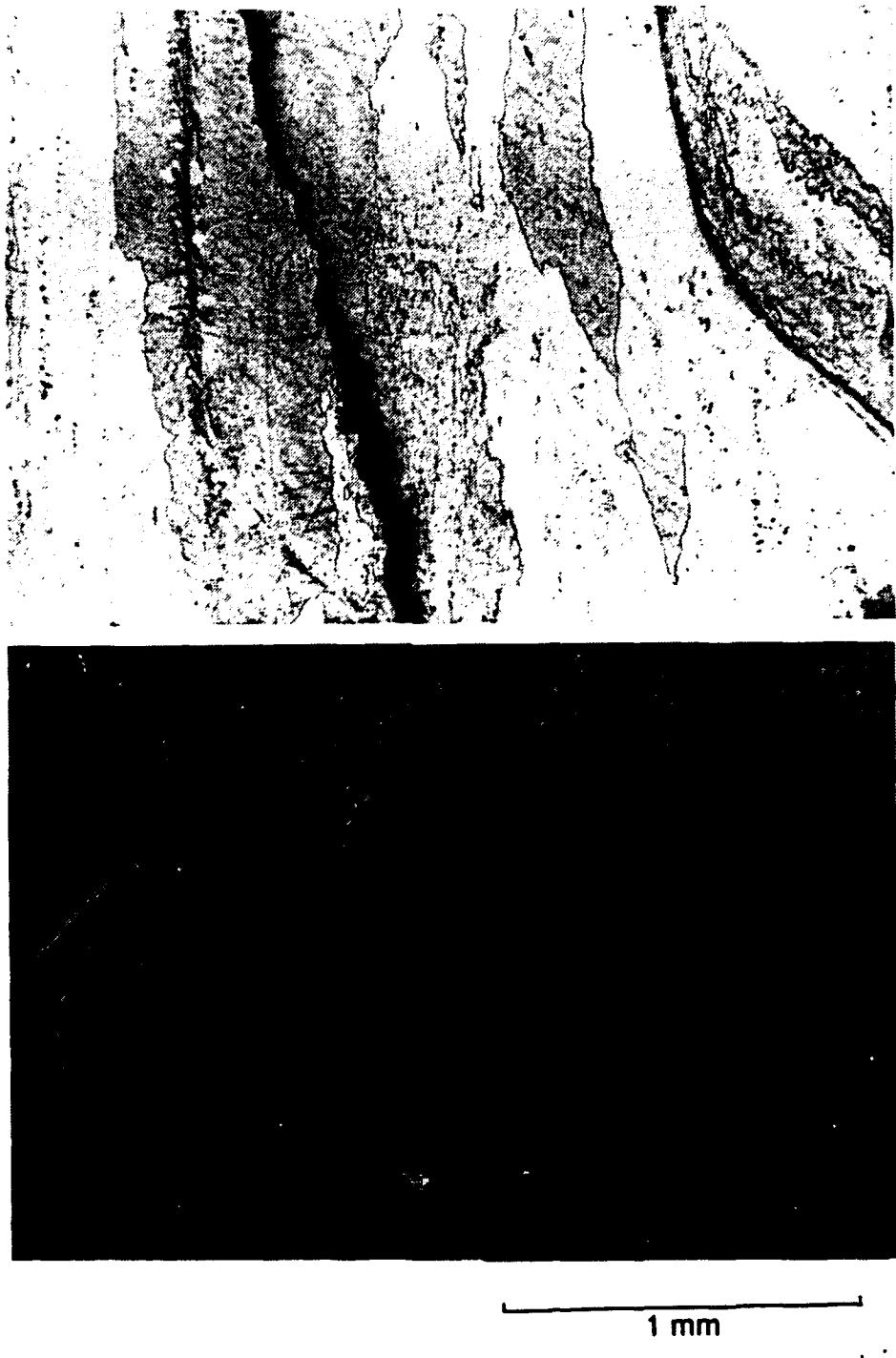
Figure I.5.5b. Adiabatic shear bands formed in the impacted zones of the 2090-T81 alloy. The cracking that occurs in these regions is often associated with the shear bands.
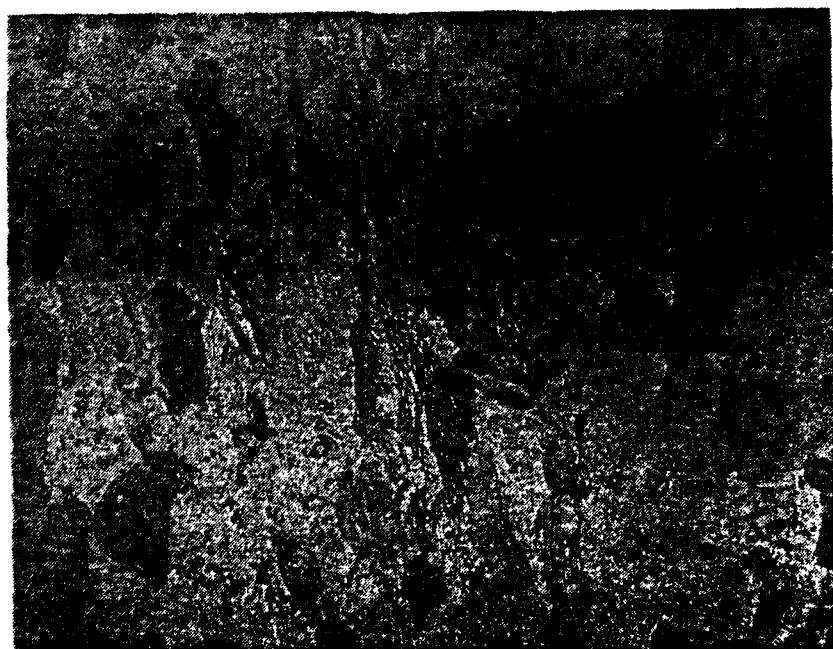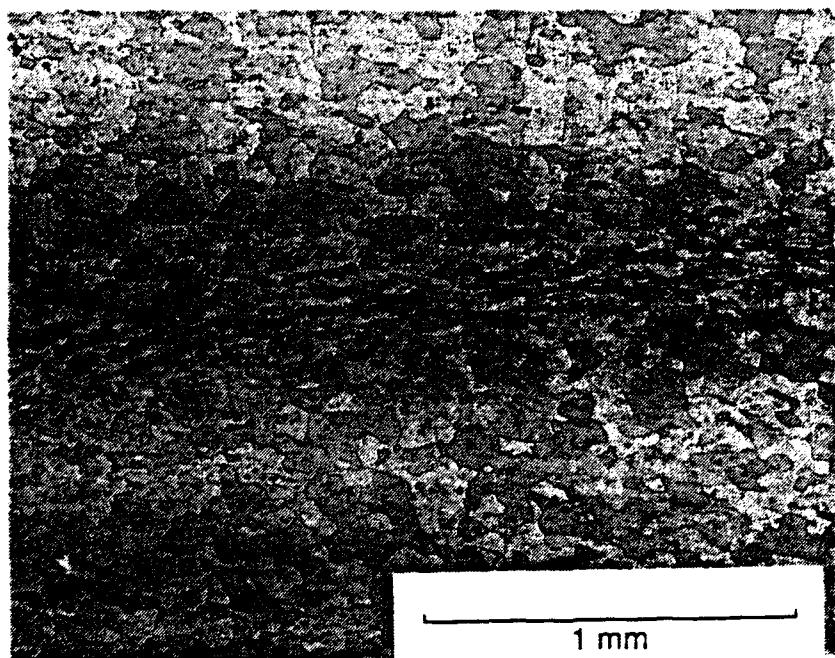
Figure I.5.5c. Planes polished slightly under the impacted surface in
the 2219-T37 specimens show the only area with high
local deformation is near the outside diameter of the
impacted area.

1 mm

Figure I.5.5d. Planes polished perpendicular to the impacted surface of
the 2090-T81 specimen show that large displacements in
the grains have occurred.

Figure I.5.6. Microreactions found on the 2090-T81 LOX specimen tested at 100 psi: (a) reaction is located at the bottom of the shear face, (b) reaction is located on the outer diameter of the specimen where contact between the specimen and the cup wall occurred.

shown. On the same specimen, another microreaction occurred where the specimen was pushed into the cup wall during deformation. Microreactions were observed in the following alloy specimens under the conditions stated: (1) 2090-T81, 1/8- and 1/16-in specimens taken from both 1/2- and 3/4-in plate at 100 and 500 psi (LOX); (2) 2219-T37 and 2219-T851, 1/16-in specimens at 500 psi (LOX); and (3) 8090-T3, 1/16-in specimens at 100 and 500 psi (LOX).

I.5.1.6. Localized Melting

The fracture surfaces on the splits of the 2090-T81 specimens have regions in which local melting may have occurred. In Figure I.5.7, the fracture surface of the split in a 2090-T81 specimen shows the typical delamination and transgranular shear observed for tensile failure in this alloy (Figures I.5.8 and I.5.9). Portions of the fracture surface on the splits, however, have very smooth, rounded features that do not exhibit the detail associated with tensile fracture. Definitive evidence of melting was not obtained during optical examinations on planes polished perpendicular to the fracture surfaces of splits. Evidence for localized melting was obtained by C.C. Wan (Aerospace Corporation), using SEM, on shear lips of MSFC specimens. He associated the local melting regions with striker-pin irregularities. He found no evidence of localized melting in the specimens tested at SSFL.

Probable localized melting areas on shear lips of specimens that were heavily deformed (8090-T3, 2090-T81, and 2219-T37) were observed during optical stereomicroscope examinations.

I.5.2. Open-Cup Mechanical Impact Testing, WSTF

I.5.2.1. Summary

The results of open-cup testing at WSTF in LOX and LN_2 are summarized in Table I.5.1. No ignitions were observed in any alloy at any energy level. Only very occasionally were cracks or splits observed; this is a good indication that MSFC and SSFL pressurized mechanical impact tests provided more absorbed energy to the specimens.

I.5.2.2. Physical Measurements on Specimens

I.5.2.2.1. Penetration Depths, Splits, Shear Lips, Eccentricity in Loading
The following parameters were measured on each impacted speciman: depth of impact, eccentricity of impact, and presence or absence of splits, cracks, delaminations, reactions, and shear lips. These measurements are presented in Appendix I.C in Tables I.C.1 and I.C.2 (8090), Tables I.C.3—I.C.5 (2090), Tables I.C.6 and I.C.7 (WL049), and Tables I.C.8—I.C.11 (2219). Eccentricity of impact is defined as the distance between the center of the specimen and the center of the striker-pin impact area. General descriptions of splits, cracks, and shear lips are given in Section I.5.1, accompanied by figures that illustrate typical features of each of these deformation modes. Section I.5.3.2, which describes the results

62
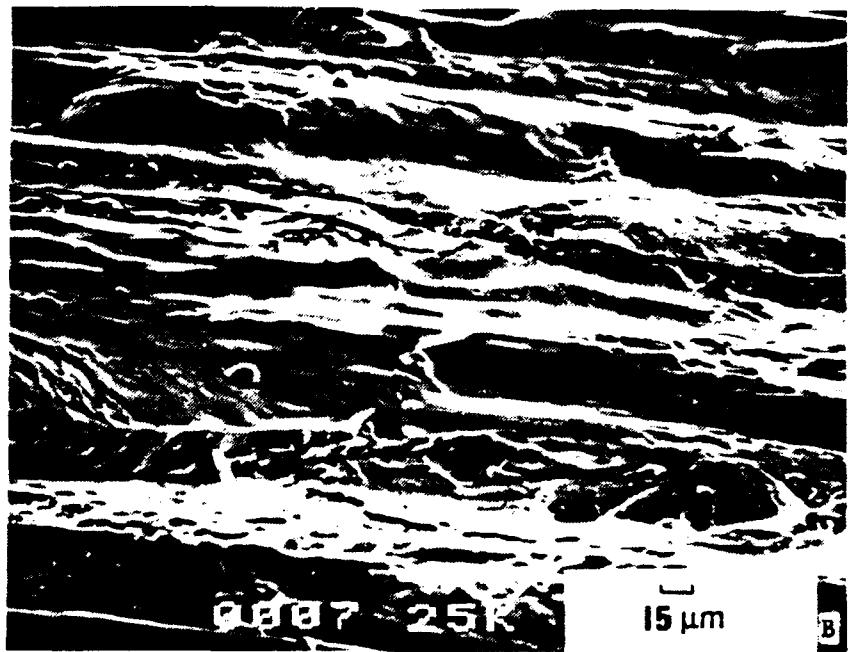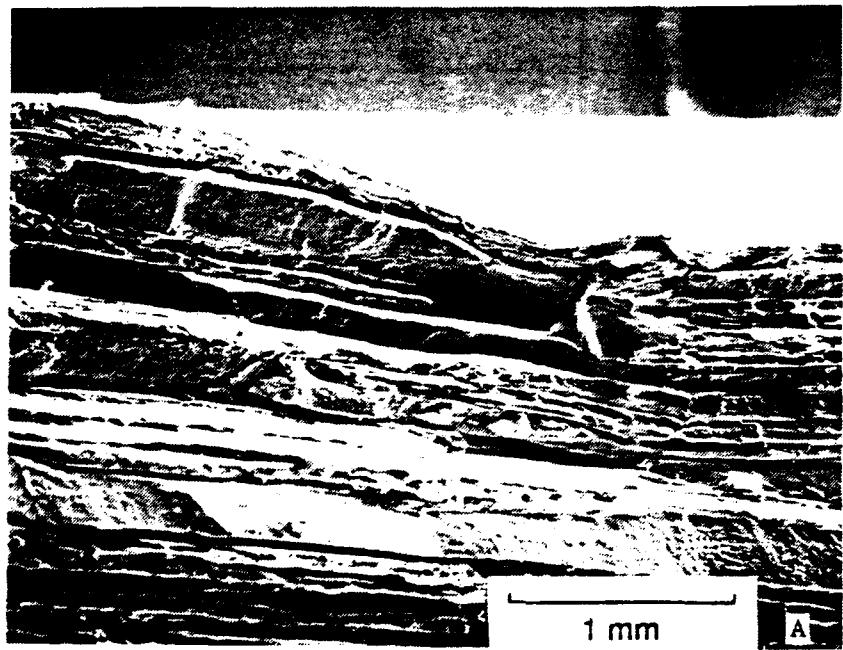
Figure I.5.7. The characteristic fracture surface of a split of the 2090-T81 LOX specimen: (a) low-magnification SEM micrograph of the general fracture morphology, (b) local, surface topography.
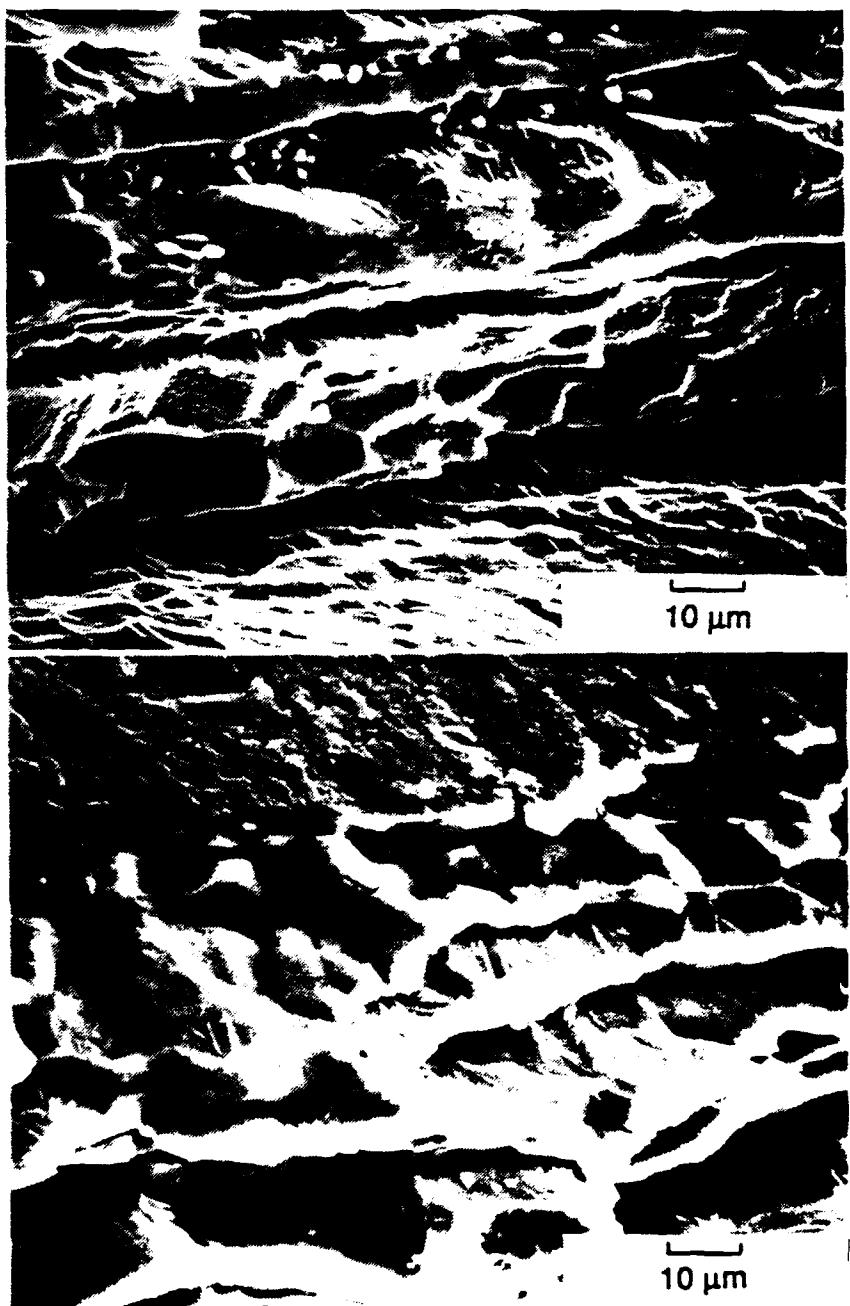
Figure I.5.8. The typical surface topography of a 2090-T81 tensile specimen fractured at 76 K.
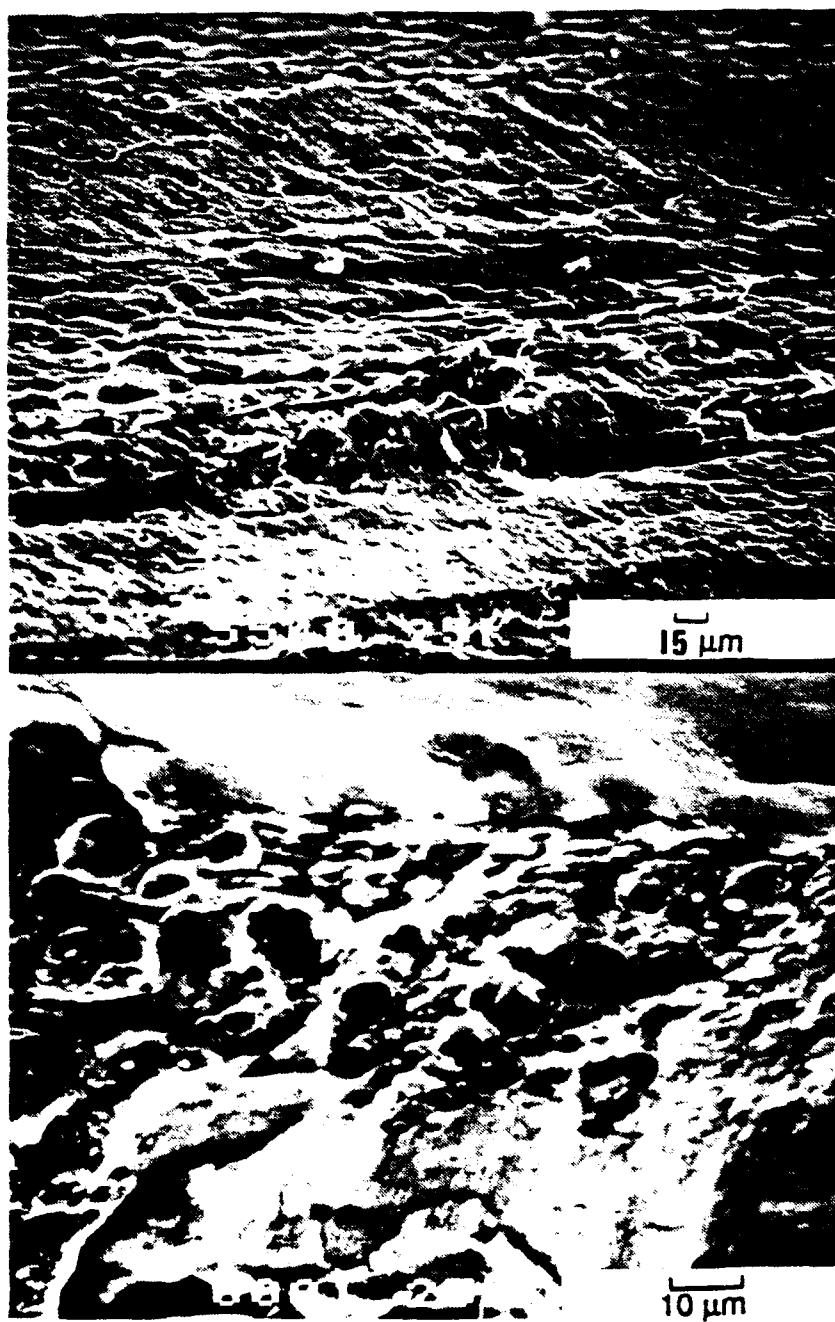
Figure I.5.9. The typical surface topography of a 2090-T81 tensile specimen fractured at 76 K.

65

Table I.5.1. Results of Open Cup Mechanical Impact Tests, WSTF:
Alloys 8090-T3; 2090-T81; WL049-T351; 2219-T851;
2219-T37.

Alloy	Specimen Thickness, in	Plate Thickness, in	Potential Energy, ft·lb(kg·m)	Environment, LOX, LN_2	No. of Impacted Specimens	Obser- vations
8090-T3	1/16	1/2	72.0 (10)	LOX	2	
8090-T3	1/16	1/2	57.6 (8)	LOX	2	
8090-T3	1/16	1/2	43.2 (6)	LOX	2	
8090-T3	1/8	1/2	72.0 (10)	LOX	2	
8090-T3	1/8	1/2	57.6 (8)	LOX	2	
8090-T3	1/8	1/2	43.2 (6)	LOX	2	
8090-T3	1/16	1/2	72.0 (10)	LN_2	2	1 split
8090-T3	1/16	1/2	57.6 (8)	LN_2	2	
8090-T3	1/16	1/2	43.2 (6)	LN_2	2	
8090-T3	1/8	1/2	72.0 (10)	LN_2	2	
8090-T3	1/8	1/2	57.6 (8)	LN_2	2	
8090-T3	1/8	1/2	43.2 (6)	LN_2	2	
2090-T81	1/16	1/2	72.0 (10)	LOX	2	
2090-T81	1/16	1/2	57.6 (8)	LOX	2	
2090-T81	1/16	1/2	43.2 (6)	LOX	2	
2090-T81	1/8	1/2	72.0 (10)	LOX	2	
2090-T81	1/8	1/2	57.6 (8)	LOX	2	1 cracked
2090-T81	1/8	1/2	43.2 (6)	LOX	2	
2090-T81	1/16	1/2	72.0 (10)	LN_2	2	
2090-T81	1/16	1/2	57.6 (8)	LN_2	2	
2090-T81	1/16	1/2	43.2 (6)	LN_2	2	
2090-T81	1/8	1/2	72.0 (10)	LN_2	2	
2090-T81	1/8	1/2	57.6 (8)	LN_2	2	
2090-T81	1/8	1/2	43.2 (6)	LN_2	2	
2090-T81	1/16	3/4	72.0 (10	LOX	2	
2090-T81	1/16	3/4	57.6 (8)	LOX	2	
2090-T81	1/16	3/4	43.2 (6)	LOX	2	1 cracked
2090-T81	1/8	3/4	72.0 (10)	LOX	2	
2090-T81	1/8	3/4	57.6 (8)	LOX	2	
2090-T81	1/8	3/4	43.2 (6)	LOX	2	
2090-T81	1/16	3/4	72.0 (10)	LN_2	2	
2090-T81	1/16	3/4	57.6 (8)	LN_2	2	
2090-T81	1/16	3/4	43.2 (6)	LN_2	2	

Table I.5.1. continued

Alloy	Specimen Thickness, in	Plate Thickness, in	Potential Energy, ft·lb(kg·m)	Environment, LOX, LN$_2$	No.of Impacted Specimens	Observation
2090-T81	1/8	3/4	72.0 (10)	LN$_2$	2	
2090-T81	1/8	3/4	57.6 (8)	LN$_2$	2	
2090-T81	1/8	3/4	43.2 (6)	LN$_2$	2	
WL049-T351	1/16	1/2	72.0 (10)	LOX	2	
WL049-T351	1/16	1/2	57.6 (8)	LOX	2	
WL049-T351	1/16	1/2	43.2 (6)	LOX	2	
WL049-T351	1/16	1/2	72.0 (10)	LN$_2$	2	
WL049-T351	1/16	1/2	57.6 (8)	LN$_2$	2	
WL049-T351	1/16	1/2	43.2 (6)	LN$_2$	2	
2219-T851	1/16	1/2	72.0 (10)	LOX	2	
2219-T851	1/16	1/2	57.6 (8)	LOX	2	
2219-T851	1/16	1/2	43.2 (6)	LOX	2	
2219-T851	1/8	1/2	72.0 (10)	LOX	2	
2219-T851	1/8	1/2	57.6 (8)	LOX	2	
2219-T851	1/8	1/2	43.2 (6)	LOX	2	
2219-T851	1/16	1/2	72.0 (10)	LN$_2$	2	
2219-T851	1/16	1/2	57.6 (8)	LN$_2$	2	
2219-T851	1/16	1/2	43.2 (6)	LN$_2$	2	
2219-T851	1/8	1/2	72.0 (10)	LN$_2$	2	
2219-T851	1/8	1/2	57.6 (8)	LN$_2$	2	
2219-T851	1/8	1/2	43.2 (6)	LN$_2$	2	
2219-T37	1/16	1/2	72.0 (10)	LOX	2	
2219-T37	1/16	1/2	57.6 (8)	LOX	2	
2219-T37	1/16	1/2	43.2 (6)	LOX	2	
2219-T37	1/8	1/2	72.0 (10)	LOX	2	
2219-T37	1/8	1/2	57.6 (8)	LOX	2	
2219-T37	1/8	1/2	43.2 (6)	LOX	2	
2219-T37	1/16	1/2	72.0 (10)	LN$_2$	2	
2219-T37	1/16	1/2	57.6 (8)	LN$_2$	2	
2219-T37	1/16	1/2	43.2 (6)	LN$_2$	2	
2219-T37	1/8	1/2	72.0 (10)	LN$_2$	2	
2219-T37	1/8	1/2	57.6 (8)	LN$_2$	2	
2219-T37	1/8	1/2	43.2 (6)	LN$_2$	2	

of pressurized testing, also defines and discusses these features in more detail.

I.5.2.2.2. Summary of Physical Measurements The statistical population for drawing conclusions is quite small for these tests. For instance, only one occurrence of a split was found in six samples of one alloy; similar results are found in the cases of cracks and delaminations. No shear lips were observed in any of the open-cup specimens. As discussed in the following section on pressurized testing, this is typical for tests conducted at WSTF.

From the summary tables on average indentation depths (Tables I.C.2—I.C.11) we conclude that the 8090-T3 alloy underwent the greatest penetration. This observation correlates well with yield strength data: the 8090 alloy has the lowest yield strength of the four alloys tested. Average penetration depths at constant potential energy are plotted versus yield strengths in Figure I.5.10 for 1/16-in thick specimens and in Figure I.5.11 for 1/8-in thick specimens. As the yield strength increases the penetration depth decreases. Data for both thicknesses of alloy 2090-T81 and for both tempers of alloy 2219 were combined to obtain the averages plotted in these figures. Data from tests in LOX and LN_2 were combined.

Finally,' the summary tables indicate that eccentric loading of the specimen was the rule rather than the exception. Although difficult to control in the open-cup tests due to the size difference between the sample and the cup, eccentric loading does increase the severity of the state of stress.

I.5.3. **Pressurized Mechanical Impact Testing, WSTF, MSFC, SSFL**

I.5.3.1. Summary

The results of the pressurized impact testing are summarized in Table I.5.2 (8090-T3), Table I.5.3 (2090-T81), Table I.5.4 (WL049-T351), Table I.5.5 (2219-T851), and Table I.5.6 (2219-T37). At WSTF there were no reactions in any alloy in either GOX or LOX at 500 psi at the nominal 72-ft·lb energy level. Likewise, no reactions were detected at SSFL for any alloy.

There were, however, reactions in all alloys that were tested at MSFC in LOX at the nominal 72-ft·lb (10 kg·m) energy level (Tables I.5.2—I.5.6). The 8090-T3 was tested only in the 1/16-in thickness and reactions were observed at both 500 and 100 psi. There were reactions in 2090-T81 at 500, 100, and 50 psi in both the 1/16- and 1/8-in thicknesses. The 2219-T851 and 2219-T37 were tested only in the 1/16-in thickness and two reactions were observed out of 20 specimens of each alloy tested at 500 psi.

Deviations from approved operating procedures have been examined as a possible cause of the reactions. Surface finish on the 2219 samples was 20—40 μin and on the 2090-T81 samples was 16—20 μin. The surface finish for test samples is not specified in the NASA NHB 8060.1B,[1] the ASTM G86-84,'
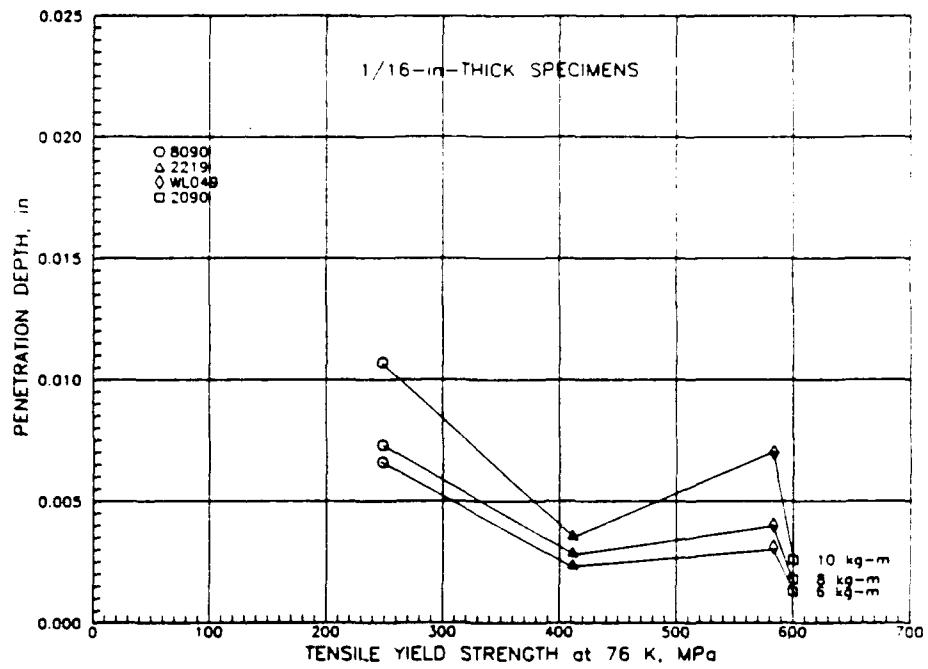
Figure I.5.10. Penetration depth vs. tensile yield strength at 76 K for
1/16-in thick specimens of alloys 8090-T3, 2090-T81,
WL049-T351, and 2219 (tempers T851 and T37).
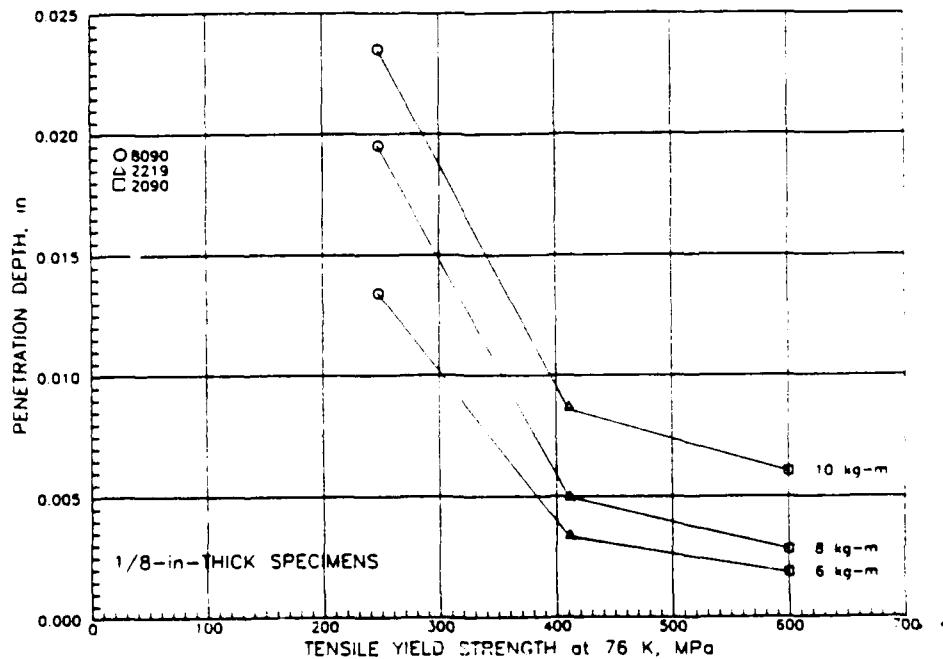
Figure I 5.11. Penetration depth vs. tensile yield strength at 76 K for
1/8-in thick specimens of alloys 8090-T3, 2090-T81, and
2219 (tempers T851 and T37).

69

Table I.5.2. Results of Pressurized Mechanical Impact Tests: Alloy 8090-T3.

	(1)	(2)	(3)	(4)*	(5)**
LOX/GOX	LOX	LOX	LOX	GOX	GOX
Pressure, psi	500	100	500	500	500
Potential Energy, ft·lbs	72	72	72	72	72
Nominal Temperature, K***	113	113	113	295	295
Specimen Thickness, in	1/16	1/16	1/16	1/16	1/16
Plate Thickness, in	1/2	1/2	1/2	1/2	1/2
Laboratory	MSFC	MSFC	WSTF	WSTF	WSTF
Reactions/tests	3/5	1/3	0/20	0/40	0/9

*   20 tests were run using the plummet catcher and 20 tests were
    run without it.
** Impacted factory surface.
*** System not in thermal equilbrium; temperature neat specimen
    not recorded at moment of impact.

Table I.5.3. Results of Pressurized Mechanical Impact Tests: Alloy 2090-T81.

	(1)	(2)	(3)	(4)	(5)	(6)	(7)	(8)	(9)	(10)	(11)	(12)	(13)	(14)	(15)	(16)	(17)	(18)
LOX/GOX	LOX	LOX	LOX	LOX	LOX	LOX	LOX	LOX	GOX	GOX	LOX	LOX	LOX	LOX	LOX	LOX	LOX	LOX
Pressure, psi	500	500	100	500	500	100	500	100	500	500	50	50	500	500	500	400	100	1000
Potential Energy, ft·lbs	72	72	72	72	72	72	72	72	72	72	72	72	72	72	72	72	72	72
Nominal Temperature, K*	113	113	113	113	113	113	113	113	295	295	113	113	113	113	113	113	113	113
Specimen Thickness, in	1/16	1/16	1/16	1/16	1/8	1/8	1/8	1/8	1/16	1/16	1/8	1/8	1/8	1/8	1/8	1/8	1/8	1/8
Plate Thickness, in	1/2	1/2	1/2	1/2	3/4	3/4	3/4	1/2	1/2	3/4	1/2	3/4	3/4	1/2	3/4	1/2	1/2	1/2
Laboratory	MSFC	WSTF	MSFC	MSFC	MSFC	MSFC	WSTF	WSTF	WSTF	WSTF	MSFC	MSFC	WSTF	MSFC	WSTF	SSFL	SSFL	SSFL
Reactions, tests	2/5	2/17	1/20	1/20	1/20	1/20	0/20	0/20	0/20	0/20	2/11	0/20	2/9	0/20	0/20	0/20	0/20	0/20

* System not in thermal equilibrium; temperature near specimen not recorded at moment of impact.

71

Table I.5.4. Results of Pressurized Mechanical Impact Tests: Alloy WL049-T351

	(1)	(2)
LOX/GOX	LOX	GOX
Pressure, psi	500	500
Potential Energy, ft·lbs	72	72
Nominal Temperature, K*	113	295
Specimen Thickness, in	1/16	1/16
Plate Thickness, in	1/2	1/2
Laboratory	WSTF	WSTF
Reactions/tests	0/20	0/20

* System not in thermal equilibrium; temperature near specimen not recorded
  at moment of impact.

Table I.5.5. Results of Pressurized Mechanical Impact Tests: Alloy 2219-T851.

	(1)	(2)	(3)*
LOX/GOX	LOX	LOX	GOX
Pressure, psi	500	500	500
Potential Energy, ft·lbs	72	72	72
Nominal Temperature, K**	113	113	295
Specimen Thickness, in	1/16	1/16	1/16
Plate Thickness, in	1/2	1/2	1/2
Laboratory	MSFC	WSTF	WSTF
Reactions/tests	2/20	0/20	0/40

* 20 tests were run using the plummet catcher, and 20 tests were run without it
** System not in thermal equilibrium, temperature near specimen not recorded
   at moment of impact.

Table I.5.6. Results of Pressurized Mechanical Impact Tests: Alloy 2219-T37.

	(1)	(2)	(3)
LOX/GOX	LOX	LOX	GOX
Pressure, psi	500	500	500
Potential Energy, ft·lbs	72	72	72
Nominal Temperature, K*	113	113	295
Specimen Thickness, in	1/16	1/16	1/16
Plate Thickness, in	1/2	1/2	1/2 .
Laboratory	MSFC	WSTF	WSTF
Reactions/tests	2/20	0/20	0/40

*System not in thermal equilibrium; temperature near specimen not recorded
at moment of impact.

nor the MSFC-SPEC-164A.[21] The pin and/or the specimen indentations were inspected for conformance to the recommended specifications. A sizable percentage of the MSFC impacted specimens had rough peripheral indentations and convex impacted surfaces. Investigation revealed that some of the pins were rough edged, concave, had diameters out of tolerance, and did not meet the recommended hardness values. These departures from accepted practice are quantified in Section I.5.3.3. and summarized in Section I.5.5.

Surface contamination of specimens was a possible cause for reactions. Results from chemical analysis of substances on the surface of similar, non-impacted specimens, and of reaction products are discussed in Section I.5.4. It was concluded that surface contamination cannot account for the ignitions at MSFC.

I.5.3.2. Physical Measurements of Specimens

The parameters described in Section I.5.2.1 for open-cup testing were measured for each specimen impacted in the pressurized tests. These parameters (from WSTF and MSFC) are presented in Appendix I.C Tables I.C.12—I.C.15 (8090-T3); Tables I.C.16—I.C.21 (2090-T81); Tables I.C.22 and I.C.23 (WL049-T351); Tables I.C.24 and I.C.25 (2219-T851); and Tables I.C.26 and I.C.27 (2219-T37).

The pressurized tests were conducted at all three laboratories, WSTF, MSFC, and SSFL. Since a significant number of specimens were tested at each facility, there is some basis for interlaboratory comparisons. Each of the characteristics noted in the summary tables are therefore discussed below from both an alloy and testing facility standpoint.

I.5.3.2.1. Penetration Depth Reviews of test data obtained from WSTF on the 1/16-in thick specimens indicated that specimens of alloy 8090-T3 exhibited an average penetration depth, $\bar{d}$, of 0.0135 in. This was the greatest average penetration depth of all alloys. Specimens of alloy 2090-T81 exhibited the smallest average penetration depth, $\bar{d}$, of 0.0012 in. This is consistent with yield strength values which are high for alloy 2090 and lowest for 8090 (87.0 and 31.5 ksi, respectively).

To assess differences between the test facilities, it is necessary to compare common alloys tested under common conditions. Unfortunately, only three alloy/environment/specimen thickness sets can be compared: 2219-T37 at 500 psi (LOX) tested at WSTF and MSFC (1/16-in specimens); 2219-T851 at 500 psi (LOX) tested at WSTF and MSFC (1/16-in specimens); and 2090-T81 at 500 psi (LOX), 1/2-in plate, 1/8-in specimens tested at all three facilities.

Histograms for each of the three tests are shown in Figures I.5.12—I.5.14. From these distributions we can draw the general conclusion that the MSFC and SSFL facilities are similar in terms of penetration depth, and the average WSTF penetration depths, $\bar{d}$, are consistently lower. Using the common 2090-T81 data as a basis for comparison, $\bar{d}$ = 0.0145 in at MSFC, $\bar{d}$ = 0.0132 in at SSFL, and $\bar{d}$ = 0.0032 in at WSTF. This indicates that the WSTF pressurized tester is supplying less energy to the specimens.

I.5.3.2.2. Splits, Cracks, and Delaminations Splitting is defined here as a through-thickness fracture of the specimen that usually is associated with

Figure I.5.12. Histogram of penetration depths for alloy 2090-T81, 500
psi (LOX) at 72 ft·lb potential energy level.

2219-T851 @ 500 PSI LOX

1/16 INCH THICK SPECIMENS
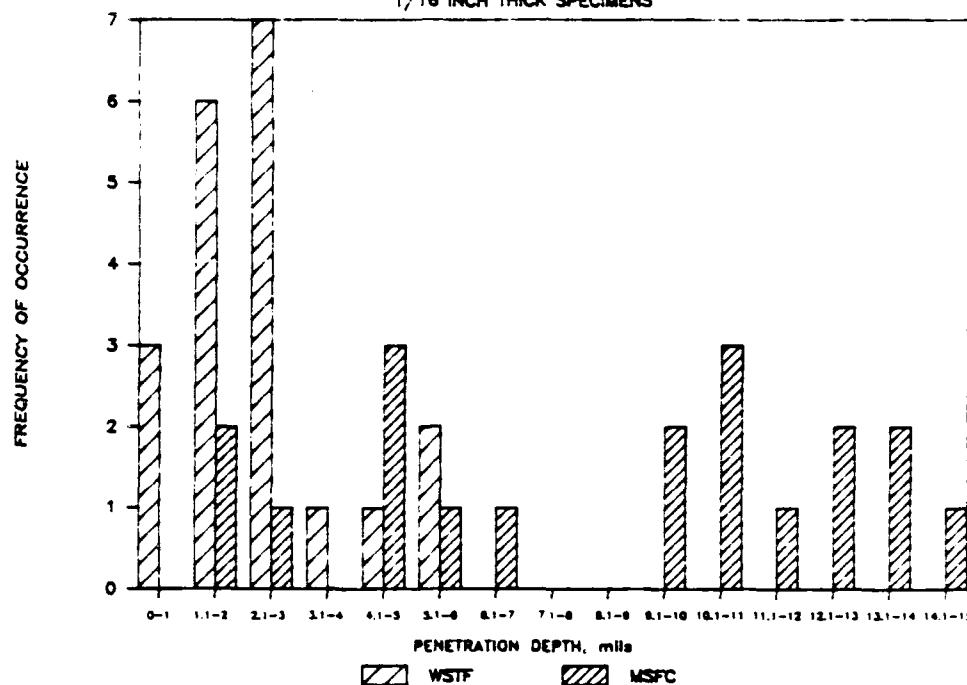
Figure I.5 13. Histogram of penetration depths for alloy 2219-T851, 500 psi (LOX) at 72 ft·lb potential energy level.

2219-T37 @ 500 PSI LOX

1/16 INCH THICK SPECIMENS
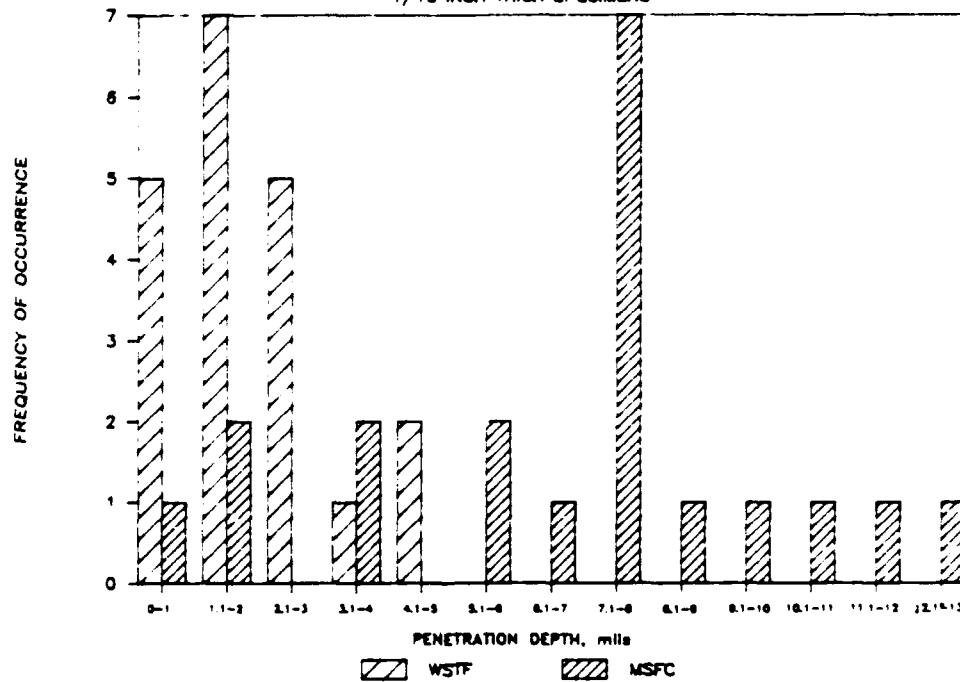
Figure I.5.14. Histogram of penetration depths for alloy 2219-T37, 500 psi (LOX) at 72 ft·lb potential energy level.

gross opening of the crack mouth. Cracks refer to smaller surface cracks visible to the unaided eye. Delaminations refer to cracking in a plane parallel to the specimen's top and bottom surfaces.

Splitting occurred in only one specimen tested at the WSTF. However, many splits occurred in 2090-T81 tested at both MSFC and SSFL. Little macroscopic cracking was found for all alloys and test facilities. Delaminations occurred primarily in the 2090 alloy when a split was present. This is consistent with fracture behavior in a laminated microstructure.

I.5.3.2.3. Shear Lips A shear-lip deformation at the edge of the impacted area was observed in most of the specimens tested at MSFC and SSFL. Of the 69 8090-T3 specimens tested at WSTF, only 15 (22%) showed evidence of this deformation. None of the 2090-T81, 2219-T851, or 2219-T37 specimens tested at WSTF had shear-lip deformations. Only 2090-T81 was tested at SSFL, but 88% of these specimens showed a shear lip at one side of the impacted area. The specimens from MSFC showed evidence of shear-lip deformation for every alloy tested: 100% of the 8090-T3; 40% of the 2219-T851; and 45% of the 2090-T81 specimens. A final observation pertains to those specimens from MSFC that split: splitting was always accompanied by a shear lip.

I.5.3.2.4. Eccentricity in Loading The pressurized impact testing machines have no provisions to maintain precise alignment after the specimen is placed in the test chamber. Therefore, it is difficult to ensure that the impact of the striker pin will be concentric with the specimen. This difference is quantified here as c, the distance between the center of the specimen and the center of the impact area. However, the WSTF pressurized tester was consistently more off center (average eccentricity, $\bar{c}$ = 0.0597 in) than the testers at the other two laboratories: $\bar{c}$ = 0.033 in at MSFC, and $\bar{c}$ = 0.0224 in at SSFL. The specimens from SSFL had impacts more consistently centered on the specimen.

I.5.3.3. Striker Pin and Specimen Cup Evaluation

Drawings and specifications on the WSTF and MSFC pins and cups are included in this report (Figures I.5.15 and I.5.16). Table I.5.7 lists these specifications and actual measurements made on available cups and pins.

Only one striker pin and two specimen holder plates were available from WSTF to evaluate. Hardness values and diameters were checked on the pieces. The WSTF pin had a slightly lower hardness value than specifications called for, as did the WSTF specimen holder plates. The diameter of the pin was within the specified tolerance and the pin had no concavity.

Of the 19 cups from MSFC available for evaluation, two had hardness values that were outside the specifications (14 and 28 R_c). The impact diameters of five pins from MSFC were measured and three of the five fell outside the specified tolerance. All of the MSFC pins inspected were found to have rough, nicked peripheral edges. Four of the six pins tested did not meet the hardness
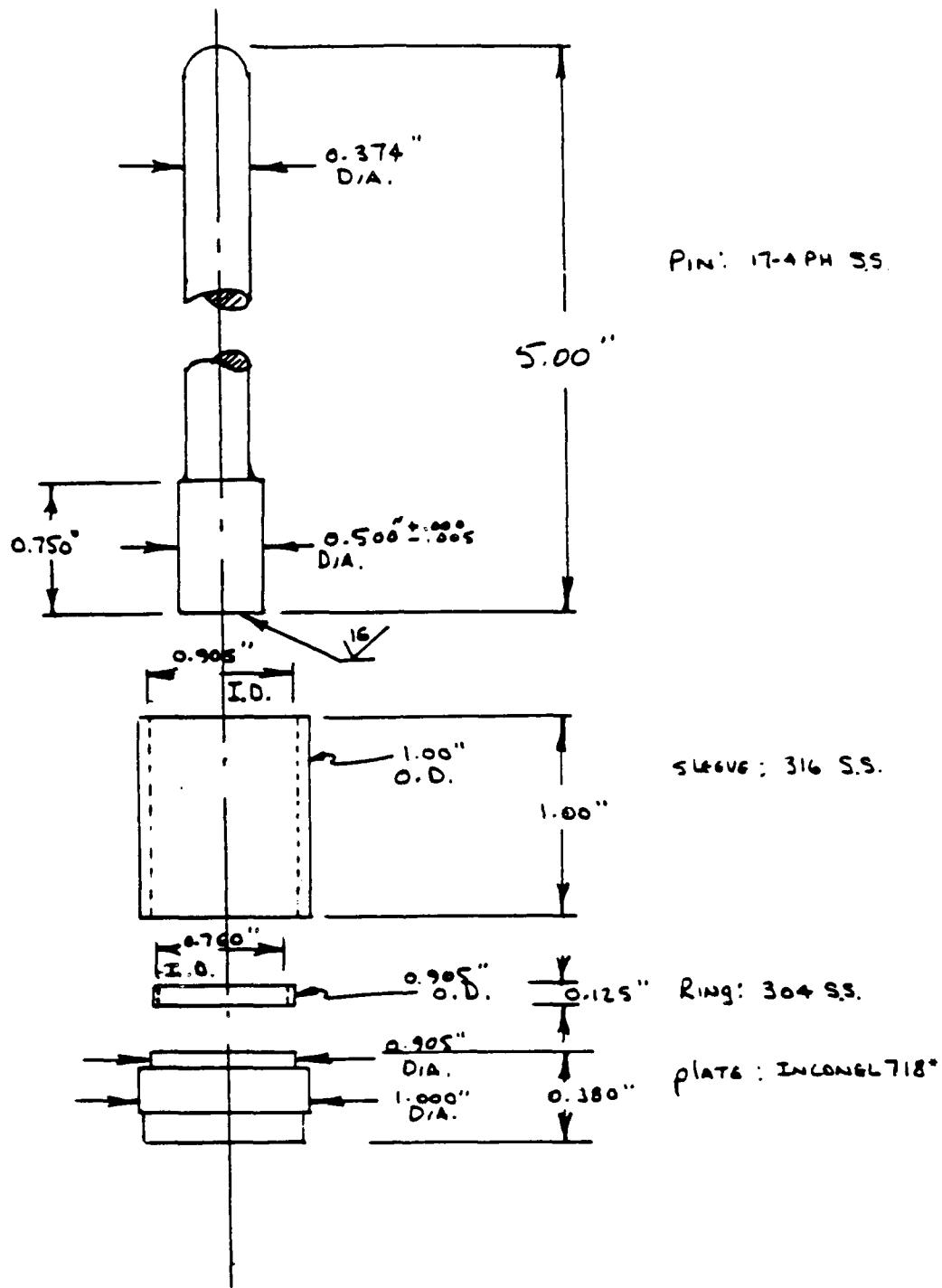
Figure I.5.15   WSTF pin and cup detail with specifications.

* Trade names are furnished to identify the material adequately.   Such
  identification does not imply recommendation or endorsements by NIST,
  nor does it imply that the materials identified are necessarily the
  best available for the purpose.

(INCONEL 718*)

(ACTUAL MEASUREMENTS)
FROM MSFC PIN
DIMENSIONS IN INCHES
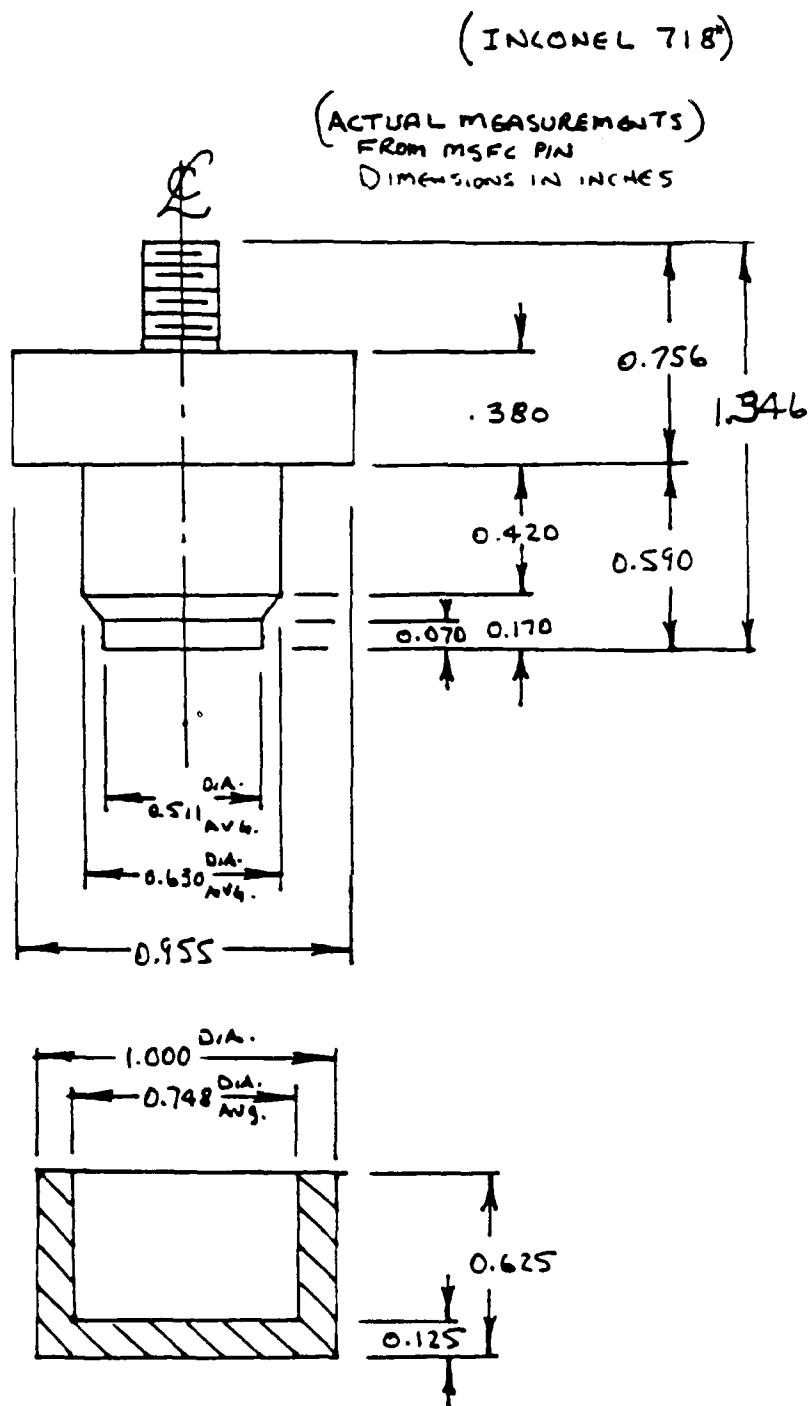
Figure I.5.16. MSFC pin and cup detail with specifications.

* Trade names are furnished to identify the material adequately. Such
  identification does not imply recommendation or endorsements by NIST,
  nor does it imply that the materials identified are necessarily the
  best available for the purpose.

79

Table I.5.7. Specifications and Measurements on Striker-Pins and Cups.

Test Facility	Item	Specified/ Actual	Material	Hardness,* R_C	Impact Diameter, in	Impact Surface Finish, μin	Concavity of Impacting Surface, in
WSTF	pins	specified	17-4 pH stainless steel	40-43	0.500 +0.000 / −0.005	16	—
		actual	not determined	37 (1 pin)	0.498	not determined	pins not examined
WSTF	cups**	specified	Ni-based alloy†	53-54	—	—	—
		actual	not determined	45, 45.5 (2 cups)	—	—	—
MSFC	pins	specified	Ni-based alloy†	36-45	0.500 ± 0.005	16	0.001,0.003,<0.001
		actual	Ni-based alloy†	23,24,20, 27,40,38 (6 pins)	0.499, 0.502, 0.514,0.518, 0.522 (5 pins)	all pins had nicked edges	0.003,0.003, 0.004,0.005, (7 pins)
MSFC	cups	specified	Ni-based alloy†	36-45	—	—	—
		actual	not determined	41,42,14, 45,43,40, 41,46,44, 41,47,47, 28,42,46, 42,43,47, 46 (19 cups)	—	—	—

* Average of three measurements
** Specimen holder plate
† Inconel 718. Trade names are furnished to identify the material adequately. Such identification does not imply recommendation or endorsements by NIST, nor does it imply that the materials identified are necessarily the best available for the purpose.

80

specification minimum, and three of the five pins tested exceeded the diameter
specification maximum. Another feature found on six of seven pins evaluated
was a concave impact surface. The concavity is defined as the maximum depth of
the curved surface on the impact face of the striker pin. Chemical analysis of
a striker pin used by MSFC confirmed that it was Inconel 718; the analysis is
reported in Appendix I.D.

I.5.3.4.   Ignition Results

Common to all ignitions in the Al alloys are these factors:
(1) there must be sufficient localized deformation to promote localized
specimen heating; (2) oxygen must be accessible; and (3) the oxide layer must
be removed to expose the local heated area to oxygen. The presence of these
three conditions was also suggested by Kasen (Appendix I.E).

Ignition characteristics are discussed for each specimen in possession of
NIST in the following sections. Some specimens were not released by MSFC;
photographs of ignitions in some specimens are presented in Appendix I.F.
Tables I.5.8 and I.5.9 briefly summarize the ignition characteristics for
alloys 8090-T3, 2090-T81,and 2219.

I.5.3.4.1. Alloy 8090   Four 8090 specimens reacted during the LOX
compatibility testing at MSFC (Figure I.5.17). Specimen 3 was tested at 100
psi (LOX) and specimens 1, 4, and 5 were tested at 500 psi (LOX). All
specimens were 1/16-in thick.

Specimens 3 and 4 (Figures I.5.17a and I.5.17b) both have extensive
melting that, for the most part, occurred in regions not under the final impact
area. There is extensive cracking in the reacted areas; however, we think that
the cracking is due to shrinkage effects during solidification of the melted
regions. The reaction morphology of specimen 4 (Figure I.5.17b) has a curious
straight side that runs from one shear lip to the other. This feature has a
smooth, planar face through the thickness of the specimen. Examination of the
striker pin and specimen suggests that this is the point where the reaction was
quenched. The pin has a melted region that becomes less severe in the location
that matches the line on the specimen. This indicates that the reaction did
initiate under the pin. The reaction apparently began before impact was
complete, because the shear-face striations change direction near the bottom
portion of the penetration. The outside diameter of the indentation made by
the striker pin is irregular and the edge of the striker pin was chipped in
several locations. Several small reactions, (one located at about 11 o'clock)
are visible near the bottom of the shear face. In specimen 5 (Figure I.5.17c),
the specimen, cup, and pin were all welded together. The reaction in specimen
1 can be seen in Figure I.5.17d.

I.5.3.4.2. Alloy 2090   Five 2090-T81 specimens react ᴊ during testing at MSFC
(Figure I.5.18). Reactions occurred at 100 psi (LOX) for specimens 14 and 17,
and at 500 psi (LOX) for specimens 2, 3, and 5. These specimens were taken
from the 1/2-in 2090 plate. Four of the specimens were 1/16-in thick (3, 5,
14, and 17); specimen 2 was 1/8-in thick.

The reacted regions on the two specimens tested at 100 psi (LOX) are on

Table I.5.8 Ignition Summary: 8090-T3 and 2090-T81.

Specimen No.	Initiation Site	Irregularities	Comments
		8090-T3	
3	Multiple ignition sites on shear lip	Shear lip, striker-pin dents	Local melting on shear lip, heavy deformation
4	Shear lip	Shear lip, striker-pin dents	Heavy deformation, evidence of local melting on shear lip
		2090-T81	
14	Shear lip at split	Shear lip striker pin dents, eccentricity = 0.5 mm concavity = 0.003 mm	Ignition during final splitting, pin clean, evidence of local melting on shear lip, horizontal ignition direction
17	Shear lip at split	Shear lip, striker-pin dents, concavity = 0.008 mm	Shear followed by ignition during descent of striker-pin, pin melted and burned

Table I.5.9   Ignition Summary: 2219-T37 and 2219-T851.

Specimen (Temper)	Initiation Site	Irregularities	Comments
12(T37)	Bottom of shear lip	Shear lip, eccentricity = 1.0 mm, striker-pin dents, concavity = 0.008 mm	Local melting on shear lip, striker-pin irregularity at ignition site, little debris on striker-pin, horizontal ignition direction
20(T37)	1/2 down, along shear	Shear lip eccentricity = 0.5 mm, striker-pin dent, concavity = 0.008 mm	Smaller multiple ignitions on shear lip, little debris on striker-pin, horizontal ignition direction
15(T851)	bottom of shear lip or below	Shear lip eccentricity = 1.0 mm, striker-pin dent, concavity = 0.010 mm	Striker-pin irregularity at ignition site, little debris on cup, extensive debris on side of striker-pin, no debris on bottom of striker-pin, vertical ignition direction
19(T851)	Microignitions on perimeter	Microcracks (vertical) on perimeter, eccentricity = 1.5 mm, striker-pin dents	Very small areas of apparent melting on specimen perimeter
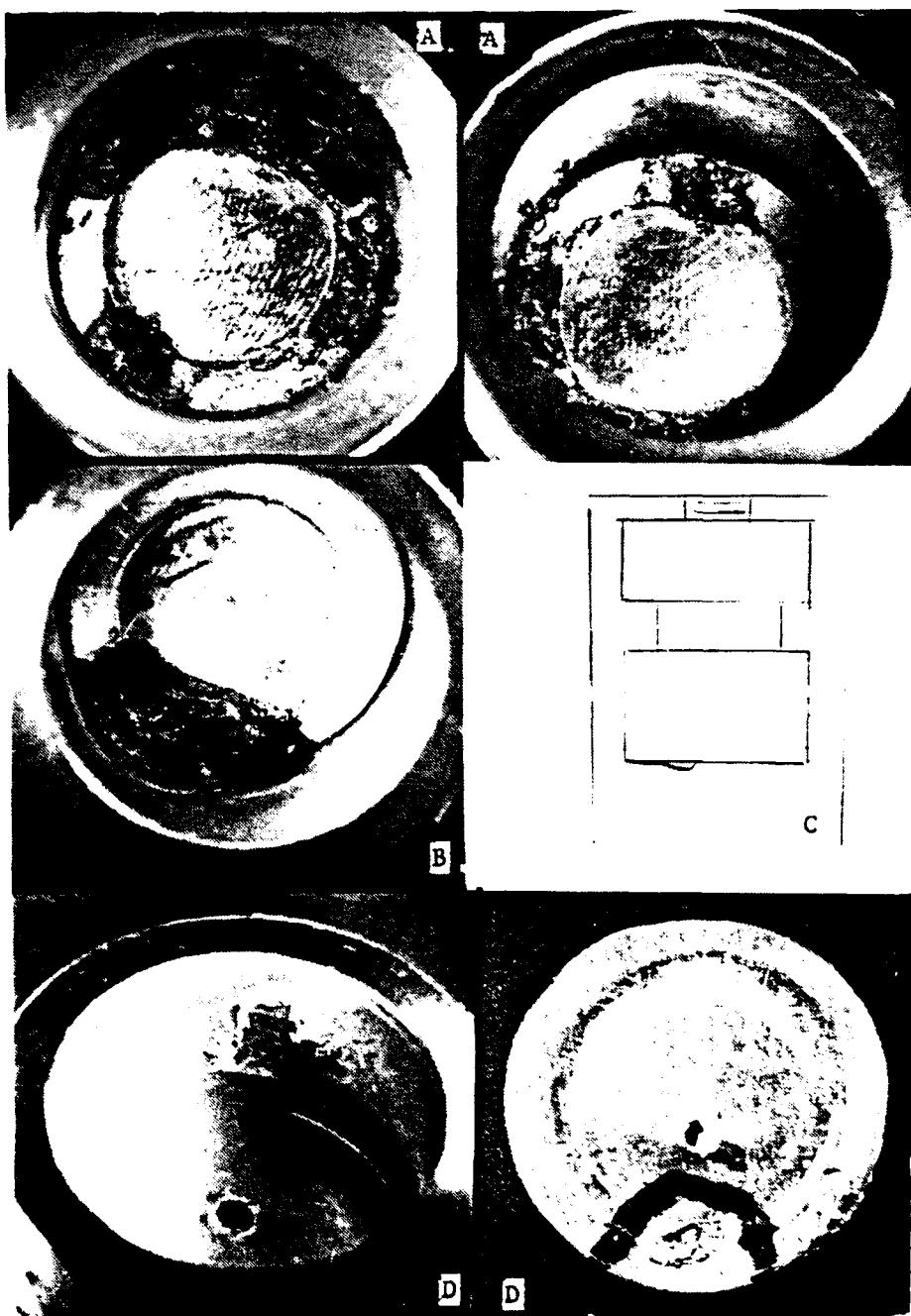
Figure I.5.17. The four 8090-T3 specimens that reacted during LOX
testing were: (a) #3, (b) #4, (c) #5 (sent out for
analysis), welded with the cup and pin during the
reaction, and (d) #1.
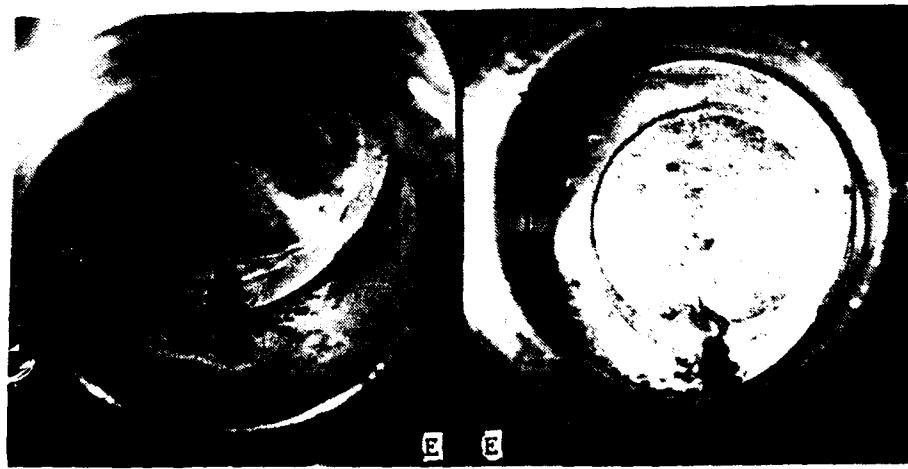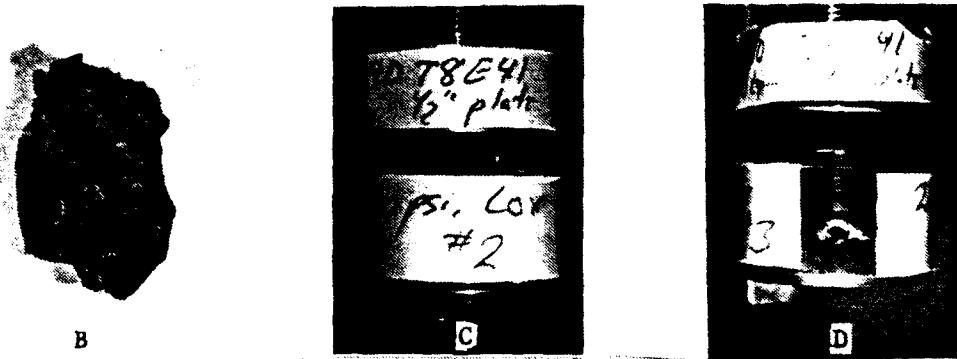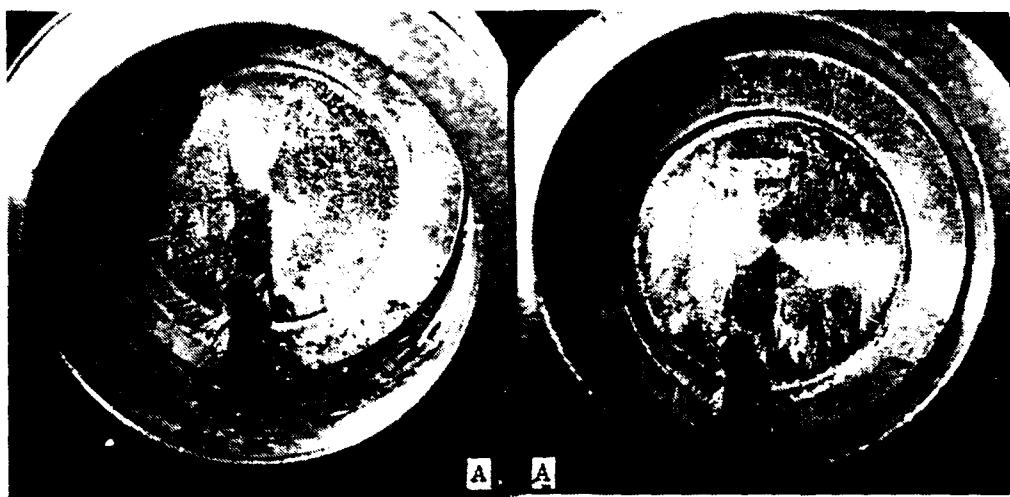
Figure I.5.18. The five 2090-T81 specimens that reacted during LOX
testing were: (a) #17, (b) #5, (c) #2, (d) #3, and (e)
#14.

the fracture surfaces of splits. The reaction on specimen 14 (Figure I.5.18e) was mild. The reacted surface retained most of the features characteristic of the fracture morphologies common to splits, but the details of the fracture surface were altered. The split occurred on specimen 14 before impact was completed because the direction of the striations changes at a position approximately half way down the shear face. The reaction appears to have occurred during splitting and to have quenched before splitting was completed: no reaction products are observable in the final portion of the split or the bottom of the pin.

Splitting occurred in specimen 17 (Figure I.5.18a), during the initial stages of deformation and the reaction was slightly more severe than that for specimen 14. The areas showing the greatest signs of melting are in the final portion of the split under the striker pin. Notable differences between specimens 14 and 17 are: (1) the impact markings at the bottom of the shear face on 17 indicate an edge was present on the radius of the pin; (2) the eccentricity of the impact corresponds to the rolling direction on 17 and was transverse to the rolling direction on 14.

The reactions were severe in the 2090-T81 specimens tested at 500 psi (LOX). The cup and pin were welded together by the heat produced during reaction for specimens 2 and 3 (Figures I.5.18c and I.5.18d), and specimen 5 (Figure I.5.18b) was consumed during the reaction.

I.5.3.4.3. Alloy 2219 The four 2219 specimens that ignited in the LOX compatibility tests at MSFC are shown in Figure I.5.19. Specimens 12 and 20 were taken from 1/2-in 2219-T37 plate. Specimens 15 and 20 were taken from 1/2-in 2219-T851 plate. All four test specimens were 1/16-in thick.

The factor common to these reacted specimens is that ignition occurred in the region of the specimen for which the distance from the outside diameter of the specimen to where the striker pin initially impacted is near its minimum value. For specimens 12, 15, and 20, the reacted zones are closely associated with the shear regions that form as material flows from under the striker pin during impact. The striated appearance of the shear lip indicates that there was a significant amount of friction between the striker pin and the specimen during impact, and the eccentricity of the specimen diameters shows that material adjacent to these shear lips deformed preferentially. The more uniform shape of the remaining specimen circumference indicates that, although there is some evidence of preferential flow due to the texture of the microstructure, the principal cause of the localized deformation is due to the off-center impact. The occurrence of reactions only in regions of the specimens for which deformation was highest suggests that these ignitions are dependent on the level of stress, strain, and strain rate.

The morphology and apparent initiation site varies for the four reactions. The reaction in specimen 12 (Figure I.5.19a) initiated somewhere near the bottom of the shear face. There is a crack or delamination at the bottom of the V shaped reacted area that is visible for several millimeters along the circumference of the final striker-pin mark. The reaction is deepest near the bottom of the V and its surface has indentations that are similar in size and shape to the grains in the 2219 alloy. The surface of the reaction forms a

Figure I.5.19. The four 2219 specimens that reacted during LOX testing were: (a) #12, (b) #15, (c) #20, and (d) #19.

plane at roughly 45° through the specimen thickness and is shallow near the outside diameter of the specimen.

The V-shaped reaction morphology for specimen 20 (Figure I.5.19c) is quite similar to that of specimen 12, but the bottom of the V is located approximately halfway down the shear face. No visible cracks were observed near the reacted surface. The shear surface appears uniform and there were no indications of gouging by the indentor near the reacted region.

The reaction in specimen 15 (Figure I.5.19b) resulted in a hole having a depth of approximately half the specimen thickness (top, dark, circular area) and a reacted zone trailing away from the hole that follows the shear face circumference. The markings on the shear face and along the bottom circumference show many irregularities. Extensive deformation occurred in the region along the impact radius. The bottom surface of the striker pin used for impacting specimen 15 was concave near its outer diameter and had numerous chips around its circumference. There appears to have been a chip in the striker pin near the "reaction hole." The reaction for specimen 19 (Figure I.5.19d) occurred along the outside diameter of the specimen. Judging from the amount of reaction debris on the cup and the direction of the spray pattern, there are reacted regions in this specimen that are not observable (because the specimen is wedged into the cup).

I.5.4. Surface Chemistry of Specimens

Specimens of alloy 2090-T81 and 2219-T851 were examined with IMMA by MSFC. They found F traces on all specimens. Fluorine is thought to be introduced by the deionized water used for cleaning of the specimens. On "factory" surfaces of alloy 2219-T851, traces of C were found. Carbon may be introduced from the oil used for protection by the suppliers during shipping and storage. Apparently, the NASA NHB 8060.1B[1] detergent-cleaning procedures do not remove all of the hydrocarbons introduced during handling.

Surface chemistries of specimens provided by NIST were also obtained, using the IMMA technique, by C. C. Wan of the Aerospace Corporation. The Interim Report of these results is included as Appendix I.F.

Organic contamination, especially on "factory" surfaces, was considered a possible reason for the MSFC ignitions. However, the heaviest organic contamination peaks included two specimens tested by SSFL. Therefore, organics that remained on the specimen surfaces are not likely to be responsible for ignitions, since two of the SSFL specimens were the most heavily contaminated with these compounds.

On impacted specimens at MSFC and WSTF Ba was identified, but was not found on other specimens that had not been tested. One very tenuous explanation is that this element is a trace impurity in the LOX or GOX used at these laboratories.

The possibility of contamination from various packaging techniques was studied in detail. Although small chemical variations were found, it was our conclusion that there was no measurable effect of the packaging technique on surface chemistry. (WSTF and MSFC specimens were packaged in teflon; SSFL specimens were packaged in ACLAR.)

The effects of cleaning procedures as recommended by NASA NHB 8060.1B[1] were examined. All specimens cleaned with this procedure had trace amounts of Na, K, Ca, Mg, and F, H, and C. One would expect presence of the alkali metals if the specimens were exposed to tap or deionized water. The presence of F, H, and C could be accounted for if a common degreaser, such as Freon, had been used. We do not attribute any ignition to these trace surface impurities.

I.5.5. Summary of Comparison of Mechanical Impact Equipment and Procedures at WSFL, MSFC, and SSFL

Comparisons of the three pressurized mechanical impact testers at WSTF, MSFC, and SSFL have been made previously (Bransford et al.,[18] and Bryan[16]).

The present summary is based on conclusions from the Al alloys that were tested at WSTF, MSFC, and SSFL. The ABMA-designed open-cup tester at WSTF is used as a baseline comparison for the pressurized testers. Because the ABMA tester uses an essentially free-falling plummet, and the striker pin is unrestrained, it was expected to deliver the highest impact energy on a test sample.

A series of impact tests in LOX and LN$_2$ were made on alloys 8090-T3, 2090-T81, 2219-T851, and 2219-T37 in the ABMA tester at 72, 58, and 43 ft·lbs (10, 8, and 6 kg·m). Average values, for each alloy, of the impact depth versus impact energy are shown in Figure I.5.20. The same alloys were impacted in LOX under pressure at both WSTF and MSFC. Indentations depths made in the samples by the 0.500-in diameter (12.5-mm) striker pins were measured and compared between WSTF and MSFC test machines. Also included in this summary are some indentation comparisons from the SSFL apparatus.

From Tables I.C.12–I.C.27 in Appendix I.C of this report, it can be seen that the average impact depths on the various alloys for the same energy levels were different for the different testers. For an impact energy of 72 ft·lbs (10 kg·m) the average depth on the ABMA impacted 2090 T81 Al-Li test specimens was 0.1295 mm (0.0051 in), whereas the average impact depths on the specimens from the pressurized testers at WSTF, MSFC, and SSFL were 0.0813 (0.0032), 0.3683 (0.0145), and 0.3454 mm (0.0136 in), respectively.

Comparing the results from WSTF on the ABMA tester and the pressurized tester, we see that the ABMA tester delivers more energy to the specimen. If we consider the relationship between impact energy and penetration depth to be linear, the ABMA tester delivers 59% more energy to the specimen than the pressurized tester. The energy losses in the pressurized tester can be attributed to greater compliance of the support structure for the specimen. Table I.5.10 compares the results from MSFC's pressurized tester with the ABMA tester at WSTF. The penetration depths of the ABMA tester are lower than the MSFC tester. Both machines have very rigid bases and similar striker-pin geometries, so machine compliances are similar. However, the ABMA tests were
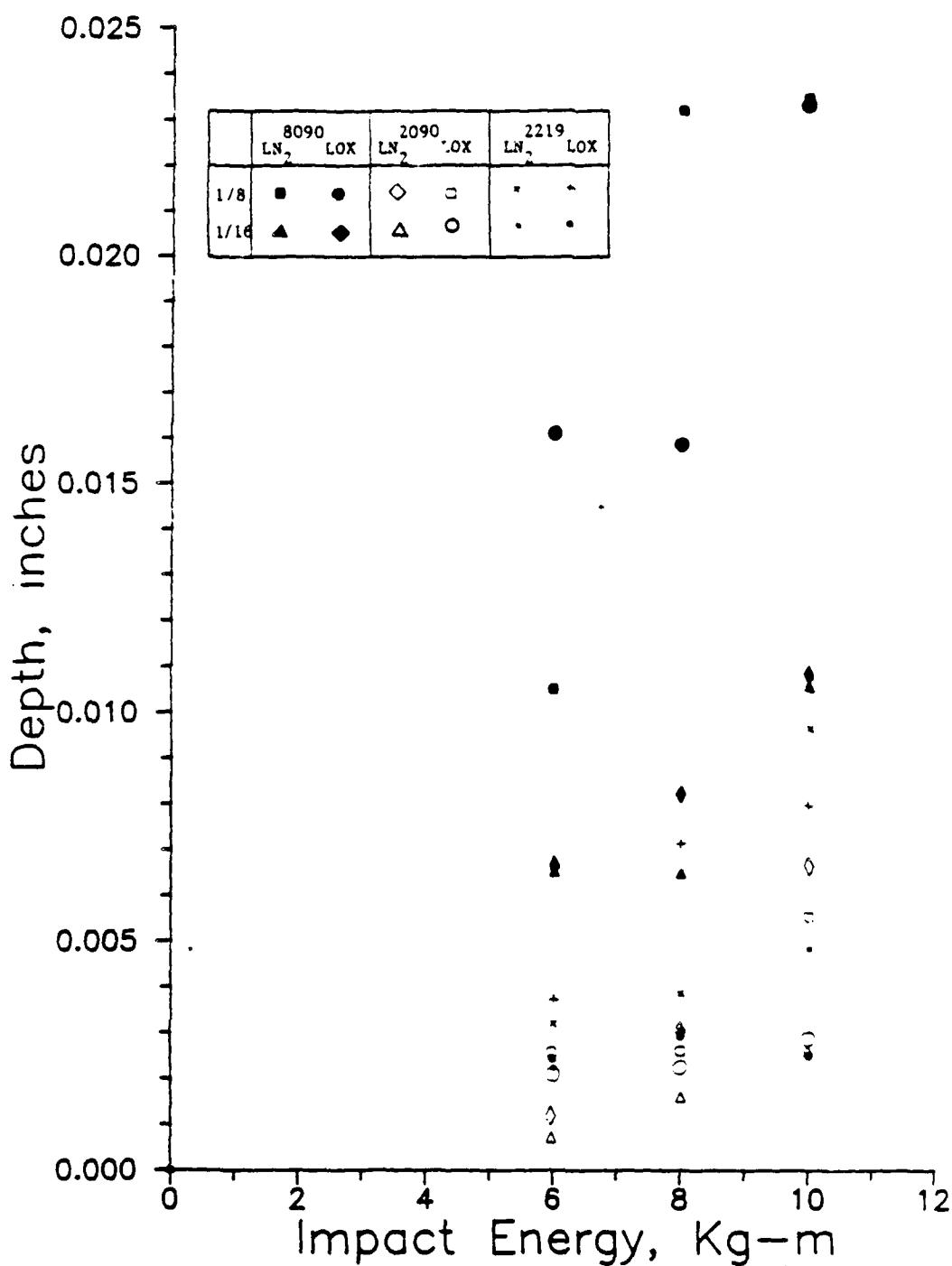
Figure I.5.20. Penetration depth vs. impact energy for alloys 8090, 2090, and 2219; 1/8- and 1/16-in thick specimens tested in LN_2 and LOX.

Table 5.10. Summary of Comparable Impact Penetration Depths and Ratios (LOX Environment) at 72 ft·lb Potential Energy Level

Alloy	Specimen Thickness, in	Pressure, psi	WSTF in	MSFC in	MSFC/WSTF	MSFC/SSFL	SSFL	SSFL/WSTF	SSFL/MSFC	ABMA, WSTF in	MSFC/ABMA	WSTF/ABMA
8090-T3	1/16	500	0.0114(20)*	0.0165(1)	1.4	—	—	—	—	0.0108(2)	1.53	1.06
2090 T81 3/4-plate	1/8	500	0.0017(20)	0.0114(20)**	6.7	—	—	—	—	0.0037(2)	3.08	0.46
2090 T81 3/4-plate	1/16	500	0.0012(20)	0.0078(7)**	6.5	—	—	—	—	0.0009(2)	8.67	1.33
2090 T81 1/2-plate	1/8	500	0.0032(20)	0.0145(17)	4.5	—	0.0136	4.25	0.94	0.0072(2)	2.01	0.44
2090 T81 1/2-plate	1/16	500	0.0016(20)	0.0082(3)	5.1	—	—	—	—	0.0046(2)	1.78	0.35
2090 T81 1/2-plate	1/8	100	—	0.0115(20)	—	—	0.0110	—	0.96	0.0073(2)	1.58	—
2219-T851	1/16	500	0.0025(20)	0.0085(19)	3.4	—	—	—	—	0.0010(2)	8.50	2.50
2219-T37	1/16	500	0.0019(20)	0.0068(20)	3.6	—	—	—	—	0.0037(2)	1.84	0.50

* Values in parentheses indicate the number of specimens tested.
** Measured by MSFC.

conducted using an Al cup; the MSFC tests used Inconel cups. The Al cup provides a much less rigid support for the specimen and is the primary reason for the shallower penetration depths in the ABMA tester.

The reasons for the differences in the impact depths were noted in the aforementioned reports. Most notably, the design differences in the pressure-chamber seals, the striker-pin assembly, and the base contribute to the impact-depth differences. The design of the WSTF pressure chamber is such that the actual impact energy delivered to the sample is lower than that delivered by the MSFC and the SSFL test machines. All three machines have high-pressure seals on the striker-pin assembly, permitting pressurization of the test chamber area. The WSTF machine uses two 15% graphite-filled ball seals, whereas the MSFC and the SSFL machines use three teflon seals for cryogenic tests. The WSTF machine has a long, small-diameter, compliant striker pin as compared to the short, larger diameter, low-compliance striker pins on the MSFC and SSFL testers. The WSTF machine has a cylindrical pipe pedestal base, utilizing a threaded anvil nut as a base for the sample cup. The MSFC and SSFL machines have a 4.0-in (100-mm) thick base with a 2.0-ft (0.6-m) cube concrete pad under that. Overall, the design of the three machines is such that the MSFC and SSFL machines deliver a higher absorbed energy to the sample than the WSTF machine.

Differences were found in the striker pin impact surfaces of the laboratories. The NASA NHB 8060.1B[1] states that the impact-pin surface areas must be 0.500 ± 0.005 in diameter and have a 16-μin surface finish. The WSTF impacts were typically very uniform in cross sectional profile with approximately 94% of the impacts having a flawless peripheral contact. The MSFC impacts were non-uniform in profile and some profiles indicated that the striker pins had concave striking surfaces. The depths of the concavity were measured on seven striker pins associated with ignitions at MSFC and found to range from 0.001-in to 0.005-in deep. The diameters of five of the seven pins were measured and found to vary from 0.499 to 0.522 in. The diameter differences result in impact stress differences of $\pm$ 5%. Approximately 64% of the MSFC impacts had flawless peripheral contacts. The SSFL impacted samples had very uniform cross-sectional impact profiles with nearly flawless peripheral contact. Measured hardness values on the MSFC cups ranged from R_c 12 to R_c 43. The pin hardness values ranged from R_c 20 to R_c 43. The only WSTF cup and pin hardness values measured were R_c 45 and R_c 37, respectively. Hardness values for the pins and cups at MSFC are both specified to be R_c 36 to R_c 45 (SSFL machine drawings and Reference 19). WSTF hardness values on the pins and cups are specified to be R_c 40 to R_c 43 (WSTF machine drawings and Reference 19) and R_c 53 to R_c 54 (WSTF machine drawings), respectively.

Notice in Table I.5.10 that the ratios of the MSFC/WSTF impact penetration depths are distinctly higher for alloy 2090-T81 than for both conditions of alloy 2219. The explanation for this involves the relationship between absorbed energy and specimen deformation (σ-ϵ curves). This is described below (see Section I.8.5).

I.5.6. Results of Promoted Combustion Tests

Promoted combustion test procedures and results are described in Appendix
I.B. At present, the following alloys have been tested: 8090-T3, ⁻⁻⁻⁻-T81,
WL049-T351, WL049-T651, 2219-T851, 2219-T37, and 2219-T87. Burn l. . versus
oxygen test pressure has been plotted, using the data of Appendix I.., ' or each
alloy in Figure I.5.21a–I.5.21d. The curves fitted to these data are plotted
in a summary graph, Figure I.5.22, which permits comparison between the alloys.
The Al-Li alloys have a relatively small initial increase in burn length with
oxygen pressure and at all pressures the burn is not sustained. Alloy 2219 in
both tempers has much larger burn lengths for equivalent pressures. It is
clear that the critical GOX pressure to sustain combustion of the Al-Li alloys
is above 80 psi. But, the critical GOX pressure to sustain combustion in both
tempers of alloy 2219 is only about 40 psi.

We tentatively conclude from these data that Al-Li alloys are less
flammable than alloy 2219 in the presence of gaseous oxygen under pressure.
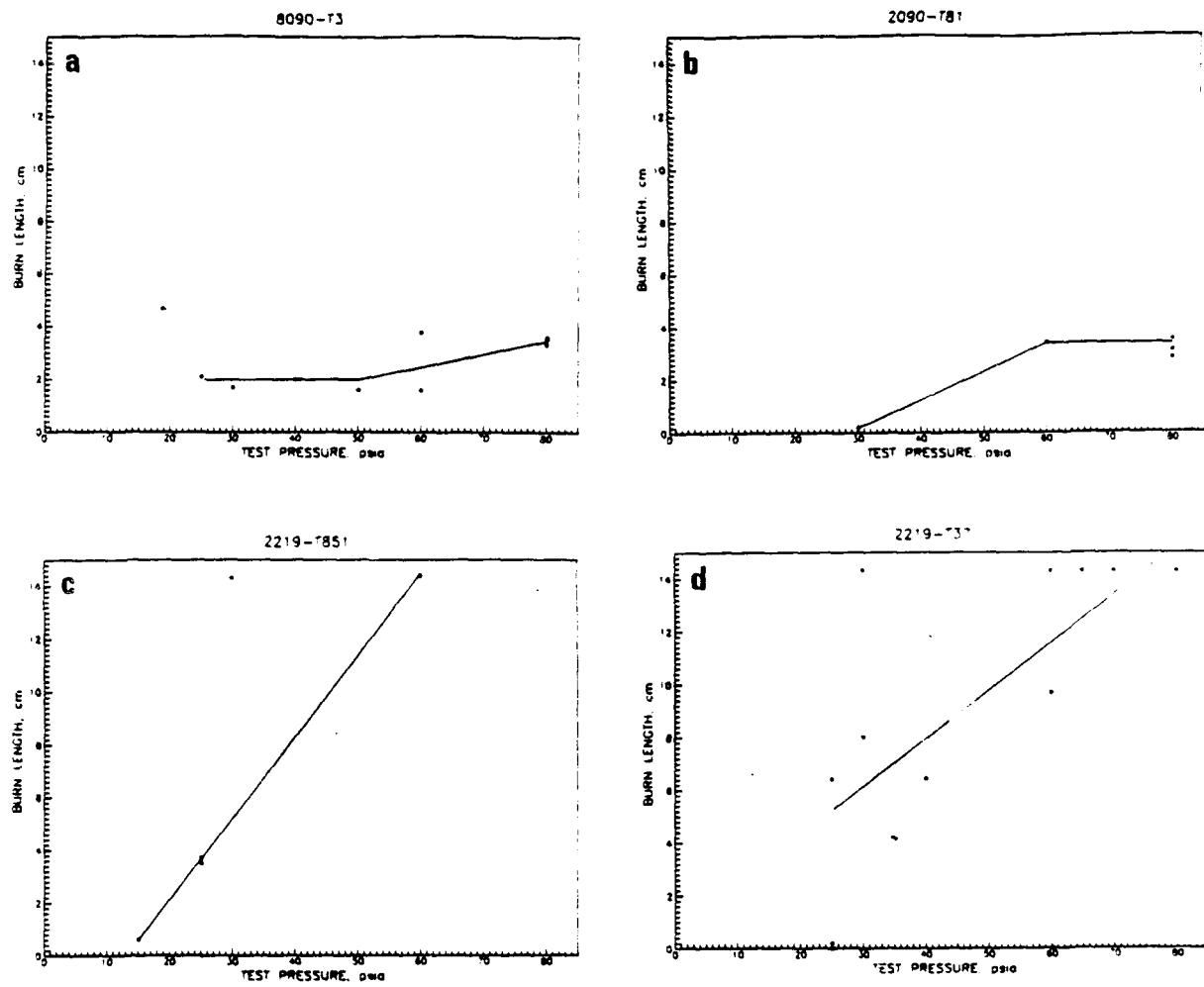
Figure I.5.21. Burn length vs. oxygen test pressure for alloys 8090-T3 (a), 2090-T81 (b), 2219-T851 (c), and 2219-T37 (d).

94
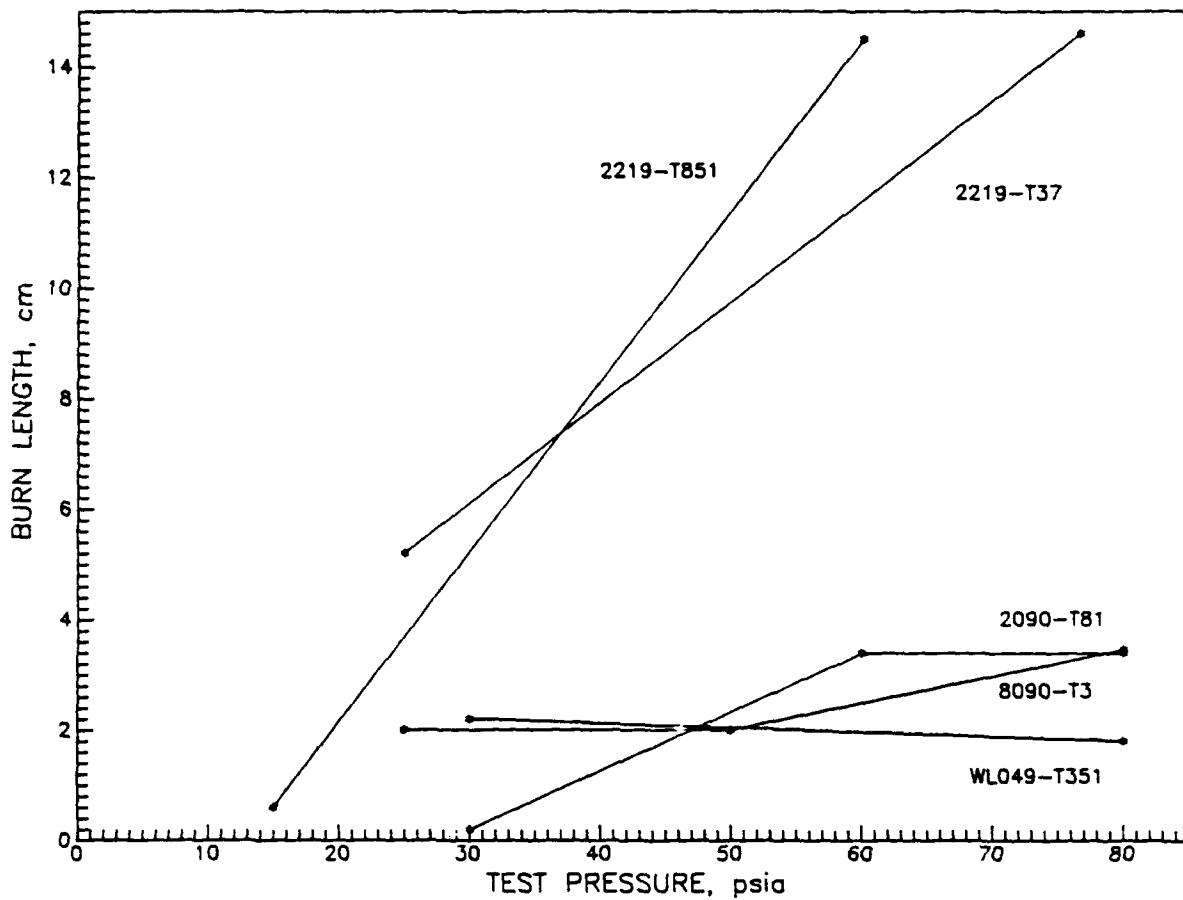
Figure I.5.22. Summary plot of burn length vs. oxygen test pressure
with curves fitted to data for alloys 8090-T3, 2090-T81,
WL049-T351, 2219-T851, and 2219-T37.

I.6. IGNITION MECHANISMS

I.6.1. Analysis of Metal Ignition Process*

Metal ignition may be viewed as a heat transfer process that involves complex chemical and material property interactions. The number of properties that can be involved are significant, and apply to each component in the oxidation process, whether reactant or product. Mass transfer is also involved. The most important mass transfer process, oxygen transport to the oxidizing interface, is part of the heat generation process due to oxidation. Other mass transfer processes are, in general, of minor importance for the ignition process, except when involved in cooling of the oxidation interface.

Borrowing from chemical reaction rate theory, an illustrative chemical reaction heat flux, Q_c, curve can be constructed as a function of the oxidizing interface temperature, T_s. An illustrative heat loss flux loss, Q_c, curve from conduction, natural convection, and radiation can also be constructed as a function of the oxidizing interface temperature. These two curves are illustrated in Figure I.6.1a.

For our development we consider only an external flux, Q_e, that is sufficient to gradually raise the temperature of the oxidizing surface. Clearly, if the external heat flux is intense enough to melt or vaporize the oxidizing material, the destruction of the material is externally controlled and the contribution from oxidation heating to the ignition process may be inconsequential. Therefore, the effects of massive external heat fluxes will not be considered. The discussion of the *effects of gradual heating* on the oxidation of a solid phase metallic material assumes an initial microlayer of surface oxide at ambient temperature.

With the application of a constant external heat flux the temperature of the surface will increase to an equilibrium value, T_{eq}, as illustrated in Figure I.6.1b. The Q_e curve is shifted vertically by the addition of the external heat flux and becomes the total input heat flux, Q_i, curve. The final equilibrium temperature will depend upon the heat loss flux. The oxidation rate of the material will increase during this heating process by one of two general oxidation mechanisms; protective or nonprotective. If the oxidation mechanism is protective, the oxide layer, which is increasing in thickness, will progressively impede transport of oxygen or metal atoms, whichever applies, to the oxidation zone. The result will be a nonlinear decrease in oxidation rate over time for a constant temperature. If the oxidation mechanism is nonprotective, the oxide layer, which is increasing in thickness, will not significantly impede the transport of oxygen or metal atoms, whichever applies, to the oxidation zone. The result will be that no substantial decrease in oxidation rate will occur over time. If the oxidation mechanism at the equilibrium temperature is protective, then the surface temperature will slowly decrease with time. Otherwise, the surface temperature will remain constant. If the slope of the Q_i curve is less than the slope of the Q_l curve at T_{eq}, then T_{eq} can be considered to be a stable temperature since a small increase in surface temperature, which would initiate an increase in oxidation heating, would be more than offset by an

*The treatment of the ignition process in this section is from Bransford et al.[22]
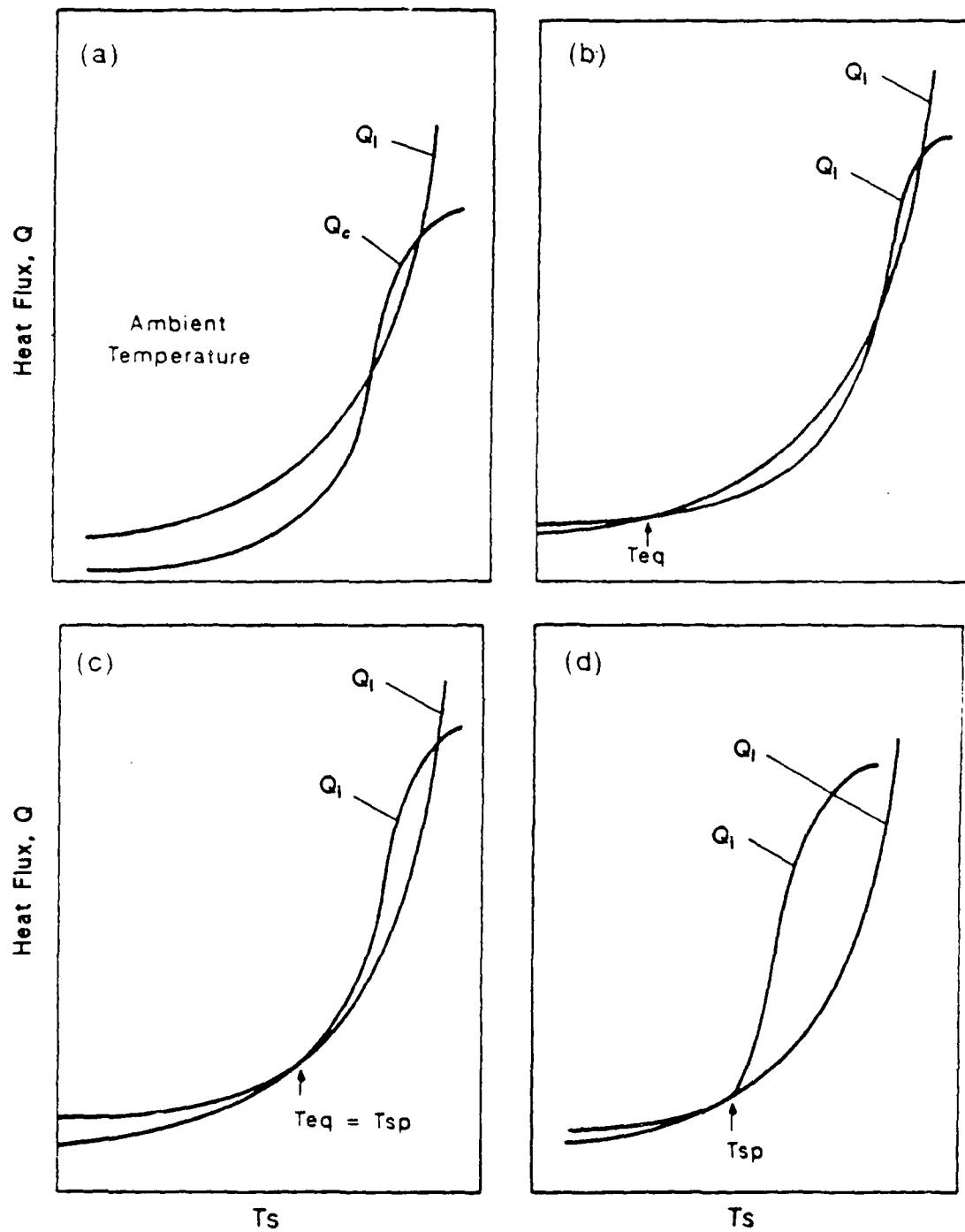
Figure I 6.1.   Illustrations of a theoretical relationship between heating rate and cooling rate vs. oxidizing surface temperature. (After Bransford and Hurley[22])

increase in the cooling rate.

As the external heating flux is systematically increased, an equilibrium temperature will ultimately be reached where the slope of the Q_i curve is equal to the slope of the Q_l curve, Figure I.6.1c. This equilibrium temperature is defined as the spontaneous ignition temperature, T_{sp}. At T_{sp}, a small increase in surface temperature, which would initiate an increase in oxidation heating, cannot be offset by an equal or greater increase in cooling rate and the material will autoheat, probably to destruction. Thus, T_{sp} should be considered an unstable temperature.

A complicating factor in this development is the effect of the transition temperature. This is the temperature where the protective oxide layer, if it exists, begins to or does break down and the oxidation rate becomes independent of time. The oxidation rate may also increase abruptly. The Q_i curve would reflect these oxidation rate changes by the appropriate changes in slope as illustrated in Figure I.6.1d. If spontaneous ignition occurs at the transition temperature, combustion would probably develop very rapidly.

Spontaneous ignition can occur while the material is in the solid phase if the cooling rate is sufficiently low. However, combustion does not commence until the material (1) melts, (2) vaporizes and oxidizes in sufficient quantities to maintain fluid oxides, as is the case, for example, with Al and Al alloys. or (3) flow develops that exposes unoxidized material, as is the case, for example, with Fe, Ni, Co and many other base metal alloys; also including Al alloys.

The ignition of Al and Al alloys is complicated by the low porosity of the protective oxide layer. The layer, which is refractive, effectively reduces the oxidation rate of the metallic material to a very small fraction of the true oxidation rate of the material. The protective nature of the oxide exists until melting occurs. This occurs many hundreds of degrees beyond the melting range of the alloy. Should an event occur that removes the protective oxide layer, the shape of the Q_i curve would change as if a transition from protective to nonprotective oxidation had occurred, Figure I.6.1d. Because of the large heat of oxidation of Al and Al-based alloys and the significant increase in oxidation rate, the material could undergo immediate combustion due to the oxide layer removal.

I.6.2. Ignition Experiments in Al and Al Alloys

Ignition experiments using Al* are strongly influenced by the very tightly adhering oxide layer which is resistant to further oxidation at temperatures up to and beyond the melting point. The melting point of Al is 932 K (659 °C) and the melting point of the oxide is 2318 K (2045 °C).[24] There are no literature references to the combustion of solid Al but molten Al can ignite and burn. For experiments performed on bulk specimens, the ignition temperature of Al is reported[25,26,27] to vary from about 1300 K to the melting point[28] of the oxide or the boiling point[26] of Al (2740 K).[24] Even single Al particles, of 35–45-μm diameter, ignited in oxygen only when the oxide layer began to break up, exposing the melted Al.[29,30] A slight decrease in the ignition temperature (below the oxide melting point) with increasing partial pressure of oxygen was noted, but pressure in the experiment was not increased above 1.7 atm.[24] Very finely divided

98

(atomized) Al has, however, been shown to ignite in air at 923 K (650 °C).[31] Experiments in which the adherent oxide layer was mechanically removed do not appear to have been carried out.*

Impact projectile tests on the Al alloy 2024 in gaseous and liquid oxygen have given conflicting ignition results. When 2024-T3 diaphragms (0.016 in) were pressurized to 60 psi in both LOX and GOX and impacted by projectiles at velocities of 6000 and 11,600 ft/sec, no combustion occurred.[32] But in tests in which thin-walled tanks of 2024 were impacted with high-velocity projectiles, combustion was observed both with GOX and LOX in contact with the Al alloy.[33] Alloy 2024 has a composition somewhat similar to 2219, except that 2024 includes 1.5% Mg. Al-Mg wires 40-100 μm in diameter have been found to ignite when electrically heated in oxygen, whereas pure Al wires tested under the same conditions did not.[34] A sample of Al-2.5 Li subjected to an oxygen/acetylene torch flame also ignited and it was believed that the Li ignited first[35] from a pool of the molten alloy. The bulk Li ignition temperature in oxygen is 463 K (190 °C), considerably below that of Al.

---

*Much of the information in this section is derived from a review of Al combustion.[23]

I.7. THERMAL-MECHANICAL IMPACT CONDITIONS

1.7.1. Analysis of the Impact

Thermal-mechanical calculations are presented here that lead to estimates of the temperature rise in impacted Al-alloy specimens. For these calculations alloy 2090-T81 physical and mechanical properties are used (or estimated). We use the physical features and measurements of specimens impacted by the MSFC and SSFC pressurized mechanical-impact equipment to estimate strain and impact penetration. These calculations should be considered approximate, since many of the impact parameters have to be estimated. They are presented in the hope that future research will establish more exact values.

I.7.1.1. Potential Energy of the Plummet

The potential energy (E_p) of the plummet is

$$E_p = MgH \qquad (7-1)$$

where M is the mass of the plummet, g is the acceleration of gravity, and H is the height of the plummet above the striker pin assembly. All of the three laboratories have identical parameters for the plummet potential energy; $M = 9.07$ kg, $g* = 9.8$ m/s^2, and $H = 1.1$ m. Using these values, $E_p = 98$ J. Since the kinetic energy of the plummet on impact with the striker pin cannot exceed this potential energy, the calculated E_p represents the maximum possible energy that could be imparted to the specimen.

In practice, this imparted energy is reduced by the following conditions: (1) The nature of the elastic/inelastic impact interactions of the plummet, striker pin, and specimen. The impact of the plummet with the striker-pin assembly, and of this assembly with the specimen are not completely inelastic and energy is consumed in their rebounds. The amount of rebound is expected to be different in the WSTF equipment compared to the MSFC and SSFL equipment because the resiliencies of the load-sustaining structures are different. (The resiliency losses of the specimen are negligible; 1-2 J.) (2) The pressure-chamber seals add a frictional force during the fall of the plummet and striker pin. The frictional losses from the three vertical guidance assemblies that ensure proper centering of the plummet are small, less than 3% of E_p. (3) The ratio of the masses of the striker-pin assembly (m) and the plummet reduces the kinetic energy imparted, even if the collision were completely inelastic (no rebound). Since $m \sim 0.04M$, this effect is small.

I.7.1.2. Velocity of the Striker-Pin Assembly

Neglecting frictional losses due to air and the guidance systems, the maximum impact velocity of the plummet, V_i, is obtained by equating the initial potential energy [Eq. (7-1)], to the increase in kinetic energy, $1/2 MV_i^2$.

---

*The variation in g with altitude between WSTF and MSFC is not significant for the discussion that follows.

$$V_i = \sqrt{2gH} \tag{7-2}$$

Using the parameters noted above, $V_i = 4.6$ m/s.

I.7.1.3. Strain Rate in the Specimen

If we assume that the maximum velocity of the plummet is translated to the striker pin and, thus, into the specimen, the resultant maximum strain rate (ϵ) of the plastic deformation in the specimen may be estimated. Here

$$\dot{\epsilon}_d(\text{max}) = \frac{V_i}{G.L.} \tag{7-3}$$

where G.L. is the apparent gage length of the deformed specimen. From optical microscopy it is evident that the entire through-thickness of the specimen deforms extensively and hardness measurements indicate that constant hardness is maintained throughout the specimen thickness; therefore, a gage length of 1/16 in (1.59×10^{-3} m) is used for the 1/16 in specimens. Using $V_i = 4.6$ m/s and Eq. (7-3), we calculate that $\dot{\epsilon} = 2.9 \times 10^3$/s. This strain rate is approximately five orders of magnitude greater than that achievable from conventional servo-hydraulic tensile machines, but about two orders of magnitude less than that obtained from impacted projectiles in high-strain-rate studies.

I.7.1.4. Time of Specimen Deformation

The duration of the impact test may be estimated by considering that the time (t_d) is

$$t_d = \frac{\epsilon}{\dot{\epsilon}} \tag{7-4}$$

where ϵ is the effective strain of the specimen. We estimate ϵ by considering that many specimens exhibit splitting. Splitting is essentially failure under primarily tensile loads, initiating near the circumference of the specimen. Strain to failure in tensile specimens in the temperature range 100–300 K is about 0.1. We consider that $\dot{\epsilon}$ is an average strain rate, and here we use $\dot{\epsilon} = \dot{\epsilon}_d(\text{max})/2$. Using these values, the test duration is estimated to be 6.9×10^{-5} s.

Another way to estimate the compressive specimen strain is to consider that $\epsilon = x_d/h$ where x_d is the depth of identation and h is specimen thickness. From Table I.C.18, a reasonable estimate of x_d is 0.013 in (3.3×10^{-4} m) and we continue to use $h = 0.0625$ in (15.9×10^{-4} m). From these values, $\epsilon = 0.21$ and, hence, from Eq. (7-4) $t_d = 1.4 \times 10^{-4}$ s.

I.7.1.5. Time for Propagation of Thermal Transient in the Specimen

To estimate a characteristic time necessary for propagation of the thermal transient (t_c) one can set the Fourier number[36] equal to one. In this approach

$$t_c = \frac{x_t^2 C\rho}{K} \tag{7-5}$$

where x_t is the length of the path of interest for thermal transient propagation, C is the specific heat, ρ is the density and K the thermal

conductivity. To obtain an estimate of t_c, we use $x_t = 0.013$ in (3.3×10^{-4} m), the average depth of impact penetration of the specimens, $\rho = 2.57 \times 10^3$ kg/m^3 (see Table I.3.10), $C = 0.5 \times 10^3$ J/kg·K (see Figure I.3.14), which represents an average specific heat for an estimated temperature rise, ΔT, of 200 K, and $K = 50$ W/m·K (see Figure I.3.15), an average thermal conductivity for an estimated ΔT of 200 K. With these values, $t_c = 2.8 \times 10^{-3}$ s.

The largest estimated time of deformation is 1.4×10^{-4} s while the estimated thermal propagation time is 28×10^{-4} s. Thus, thermal transient propagation lags specimen deformation by a factor of twenty. This leads one to expect some evidence of adiabatic shear bands, since they are known to occur at higher strain rates when thermal equilibrium lags mechanical equilibrium.

I.7.1.6. Absorbed Energy

The impact of the striker pin with the specimen results in two prominent deformation modes. (1) The striker pin causes a permanent deformation depression in the specimen and, (2) hoop stresses around the circumference of the specimen, caused by outward expansion of the specimen, are sufficient to cause specimen splitting and cracking. In some cases the specimen split continues well under the impact penetration, implying the existance of strong hoop stresses well into the interior of the specimen. However, for these calculations, we assume that the compressive mode occurs only under the striker pin, and the tensile mode occurs in the portion of the specimen outside the striker pin radius. There is a third deformation, the radial strain of the specimen. Our calculations indicate that this contribution to the absorbed energy is relatively small and it is, therefore, ignored.

Thus, the absorbed energy of an impacted specimen (E_a) may be calculated by considering that

$$E_a = \sigma_c \epsilon_d V_c + \sigma_h \epsilon_t V_t \qquad (7\text{-}6)$$

where σ_c is the average compressive flow stress, ϵ_d is the compressive specimen strain, V_c is the compressed volume, σ_h is the average tensile hoop stress, ϵ_t is the tangential specimen strain, and V_t is the tensile-stressed volume. We use $\sigma_c = 800$ MPa, $\sigma_h = 800$ MPa, $\epsilon_d = 0.21$ (considering that the average penetration depth is 0.013 in and that the effective compressive gage length is 0.0625 in (1.6×10^{-3} m)), $\epsilon_t = 0.12$ (considering that tensile failure occurs during splitting), $V_c = \pi r^2 h = 2 \times 10^{-7}$ m^3 and $V_t = 1.8 \times 10^{-7}$ m^3. Thus, $E_a = 53$ J, about 1/2 of the original potential energy of the plummet. Equation (7-6) is a static, order-of-magnitude approximation of the total energy that is absorbed by the specimen; during the actual deformation process, σ and ϵ will differ over various parts of the total deformed volume.

I.7.1.7. Rate of Energy into the Specimen

The rate of energy imparted into the specimen from impact, $\dot{q}_{in}$, may be calculated using three different approaches: (1) Reed and Simon[37] calculated energy fluxes in deforming specimens using

$$\dot{q}_{in} = \dot{\epsilon}_d(max) \, \sigma_f V \qquad (7\text{-}7)$$

102

where σ_f is an average flow stress and V is the specimen volume. We choose to use $\sigma_f = 800$ MPa for these calculations since an average ultimate strength of 2090-T81 is about 800 MPa at 76 K. There is ample evidence of extensive plastic deformation throughout the specimen, and many of the specimens exhibited splitting (fracture). From two-dimensional static stress analyses in Section I.7.2. we obtain pressure values varying from 633 to 1690 MPa. The volume of the specimen is $\pi r^2 h$ where $r = 0.34$ in (8.6×10^{-3} m) and h is 0.0625 in (1.6×10^{-3} m). Using $\dot{\epsilon}_d(max) = 2.9 \times 10^3$ s^{-1} (from Section I.7.1.3.), we calculate that $q_{in} = 86 \times 10^4$ W.

(2) A maximum value may be estimated using the potential energy of the plummet, E_p. Then,

$$\dot{q}_{in}(max) = E_p/t_d. \qquad (7-8)$$

From previous calculations we know that $E_p = 98$ J and that estimates of t_d are 0.69 and 1.4×10^{-4} s. Using $t_d = 1 \times 10^{-4}$ s, we obtain $\dot{q}_{in} = 98 \times 10^4$ W. (3) A more realistic E_p may be estimated by considering the two factors that reduce the translation of potential energy to kinetic energy to impact energy: (1) elastic rebound of plummet; and (2) frictional effects.

The contribution of the pressure seal to friction of the falling striker pin assembly is thought to be small. The Bransford, et al.[18] data show no differences in penetration depths for tests in the MSTF and SSFL equipment when pressure and seals are used, compared to tests without. This stongly suggests that the Omniseal piston seals of these systems contribute insigniticant frictional losses. Therefore, we assume that E_p is not affected by the friction of the seals.

Rebounds are observed during testing and both MSFC and SSFL have rebound catching devices to preclude additional impacts. Typical rebound heights at MSFC are considered to be about 1/3 of the original height; at WSTF we recorded one rebound of 2/3 of the original height of the plummet. Therefore, for these calculations, it is considered that 2/3 E_p is transferred to the specimen during the first (and only) impact strike in the MSFC tests and that 1/3 E_p is transferred to the specimen in WSTF tests.

Thus, $\dot{q}_{in}(max)$, at MSFC, is reduced by approximately 1/3 from the sum of these effects, or $\dot{q}_{in}(adj) = 65 \times 10^4$ W. Considering the estimates required for this calculation, this value is in reasonable agreement with that value of $\dot{q}_{in}$ (86×10^4 W) calculated from specimen deformation using Eq. (7-7).

I.7.1.8. Heat Transferred Out of the Specimen

While it is reasonable to consider that adiabatic heating conditions exist in the Al-alloy specimens during impact, several simple heat transfer calculations support this assumption.

Surface Heat Transfer:

The heat flux ($\dot{q}_s$) from the specimen surface to the outside coolant (LOX) is[38]

$$\dot{q}_s = A_s h_s \Delta T \qquad (7-9)$$

where A_s is the surface area of the specimen, h_s is the heat transfer coefficient, and ΔT is the temperature gradient. Using $\Delta T = 200$ K, $\dot{q}_s/A$ may be found from Figure I.7.1 to be about 2×10^4 W/m^2 and $A_s = 2.3 \times 10^{-4}$ m^2 for 0.0625-in (1.6×10^{-3}-m) thick specimens. Thus, $\dot{q}_s = 4.6$ W, clearly minuscule compared to $\dot{q}_{in}$.

Solid Heat Transfer:

The heat flux ($\dot{q}_L$) carried within the solid(s) may be estimated using

$$\dot{q}_L = \frac{2K \, \Delta T A}{\Delta x} \qquad (7\text{-}10)$$

where the factor of 2 is used to estimate the maximum $\dot{q}_L$ carried in both directions of the specimen to the cup and striker pin. Again, we use $\Delta T = 200$ K. The distance of heat transfer, Δx, is assumed to be 0.0312 in (0.8×10^{-3} m) and the area through which the flux is carried is $A = \pi r^2 = 2.3 \times 10^{-4}$ m^2. An average thermal conductivity of the Al alloy (over the temperature range) equals 60 W/m·K. With these estimates, $\dot{q}_L = 6.9 \times 10^3$ W, which is also very low compared to $\dot{q}_{in}$.

I.7.1.9. Stored Energy in the Specimen

In the process of plastic deformation, defects are created. These include dislocations, vacancies, and interstitials. If not annihilated, they remain after deformation. The energy required to create these defects is essentially stored in the deformed alloy. A review of stored energy measurements and mechanisms has been presented by Bever et al.[39]
The few experimental data at low temperatures differ with respect to absolute values of the percentage of the energy of deformation that remains stored, but most data suggest a value of about 70 percent for face-centered cubic alloys at 4 K. This is much larger than that typically reported for room temperature, about 10 percent. The increase of stored energy at very low temperatures is generally attributed to the contributions from interstitials and vacancies; at higher temperatures these diffuse and annihilate. The dependence of stored energy (E_{se}) on temperature in the range 4 to 77 K is very steep; for these calculations we assume a value of $0.2\dot{q}_{in}$ to represent an average E_{SE} between 100 K and the highest temperature reached by the specimen during the impact event.

I.7.1.10. Energy per Unit Mass from Homogeneous Specimen Deformation

Several different approaches may be used to estimate the temperature rise of the specimen during impact. These are discussed below:

(1) From Read and Reed,[40]

$$C\Delta T = \frac{P\Delta x}{V\rho} \qquad (7\text{-}11)$$

where P is the maximum load on the specimen, Δx is the specimen deformation, and ΔT is the rise in specimen temperature that is estimated considering the average specific heat, C, over the temperature range. Here the volume of the deformed region, $V = Ah$ and $P = \sigma A$ where σ is taken as 800 MPa. We estimate that $\Delta x/h = 0.22$. Hence, $C\Delta T = 7 \times 10^4$ J/kg from these values.
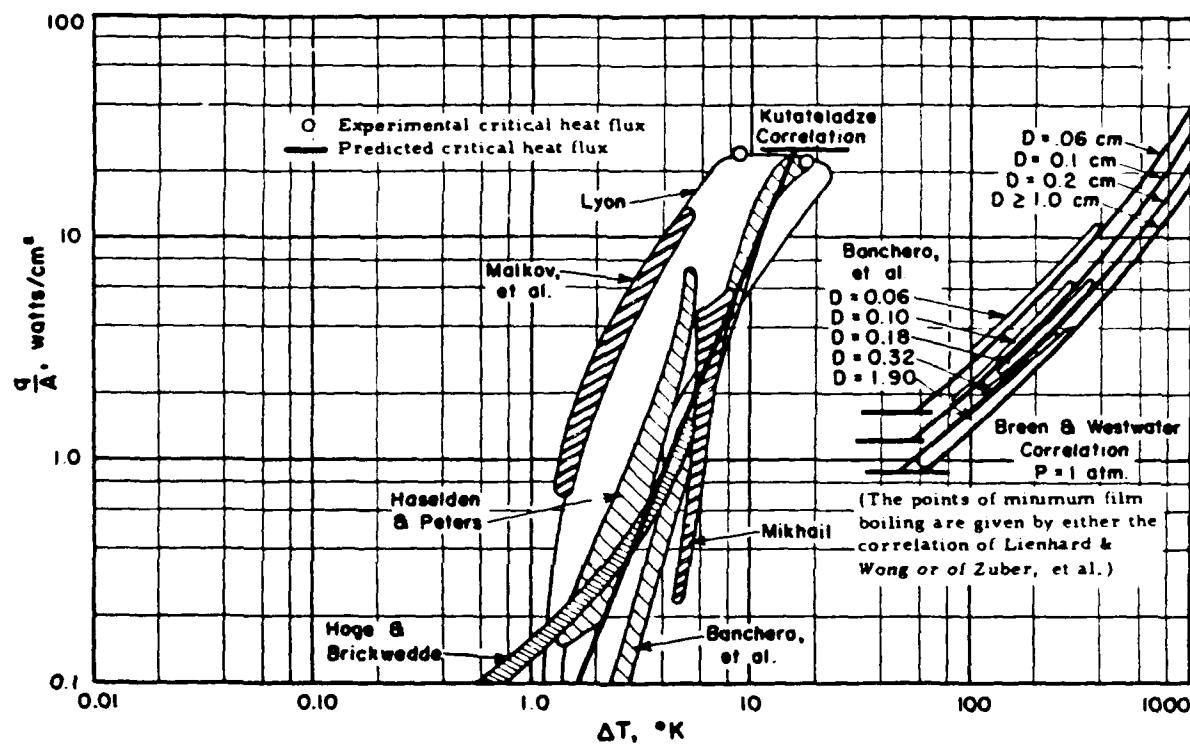
Figure I.7.1. Experimental nucleate and film pool boiling of oxygen at one atmosphere compared with predicted correlations of Kutateladze, and Breen and Westwater. (Figure adapted from Reference 38.)

(2) From Reed and Simon,[37] who considered the rates of energy in, out, and stored during tensile deformation at low temperatures,

$$C\Delta T = [\dot{q}_{in} - \dot{q}_{out})t_d]/V\rho, \qquad (7\text{-}12)$$

where $\dot{q}_{in} = \dot{\epsilon}_d(max)\sigma V = 86 \times 10^4$ W (from Section I.7.1.7., approach 1) and $\dot{q}_{out} = \dot{q}_s + \dot{q}_L + \dot{E}_{se} = 0.2\dot{q}_{in}$ since $\dot{q}_s$ and $\dot{q}_L$ are very small (adiabatic conditions).

Using $t_d = 1.4 \times 10^{-4}$ s, $V = \pi r^2 h = 3.7 \times 10^{-7}$ m^3, where $r = 0.34$ in $(8.6 \times 10^{-3}$ m), $h = 0.0625$ in $(1.6 \times 10^{-3}$ m), and $\rho = 2.57 \times 10^3$ kg/m^3, we find that $C\Delta T = 10 \times 10^4$ J/kg.

(3) Finally, we know that

$$E = mC\Delta T \qquad (7\text{-}13)$$

where m is taken as the mass of the specimen $(9.5 \times 10^{-4}$ kg) and $E = 65$ J from the earlier discussion of potential energy and the estimate of energy reduction from rebound effects at MSFC (Section I.7.1.7., approach 2). Therefore,

$$C\Delta T = 6.8 \times 10^4 \text{ J/kg.} \qquad (7\text{-}14)$$

Thus, from three different approaches, we find close similarity of calculated results for $C\Delta T = 7$, 10, and 6.8×10^4 J/kg. In the subsequent calculations of the temperature rise, we use $C\Delta T = 7.9 \times 10^4$ J/kg.

I.7.1.11. Specimen Temperature Rise

An estimate of the instantaneous temperature rise of an impacted specimen requires integration of a C(T)dT term to a temperature commensurate with the values calculated from the previous section. The polynomial fitted to the synthesized curve described in Section I.3.4.2. was used for C(T) in this integration. The initial temperature is taken as 113 K, because thermocouples in the test block record this value just before impact

from T = 113 K to 200 K, $\int C(T)dT = 6.1 \times 10^4$ J/kg $\qquad (7\text{-}15)$

from T = 113 K to 300 K, $\int C(T)dT = 15 \times 10^4$ J/kg. $\qquad (7\text{-}16)$

Thus, if the entire specimen heated up uniformly, it would only reach a temperature near ambient. Homogeneous deformation of the specimens would not result in a temperature rise to the melting point.

To achieve melting, anisotropic flow (such as adiabatic shear bands) must concentrate the deformation by a factor of about 8. This considers that $T_m = 933$ K for pure Al, and that $\int C(T)dT$ needed to reach this temperature is about 68×10^4 J/kg. Adiabatic shear bands are thought to result in a stress focus of the order of 8. These calculations have assumed a specimen thickness of 0.0625 in $(1.6 \times 10^{-3}$ m). For a specimen thickness of 0.125 in $(3.2 \times 10^{-3}$ m), the rates of energy and energies per unit mass of the thicker specimens would be about half those of the thinner specimens. Therefore, localized temperatures in the thicker specimens would tend to be lower.

I.7.1.12. Summary

Temperature increases in the impacted specimen of over 150 K have been calculated for 0.0625-in (1.6 x 10^{-3}-m) thick Al alloys. Calculated impact energies are in good agreement using both estimates from the kinetic energy of the striker-pin assembly and from specimen deformation. Use of a rather high impact stress level of 800 MPa produces good agreement of data. Localization of the impact stress by a factor of about 8, either by imperfect striker-pin geometry or by planar or delaminar deformation, would result in local melting.

The calculation of energy absorbed and estimates of energy losses from collison and rebound suggests that about 2/3 of the original potential energy is absorbed by the specimens in the MSFC tests.

From earlier discussions of the ratio of penetration depths of impacted specimens from MSFC and WSTF, we conclude that the energy absorbed by MSFC specimens was at least a factor of 3.5 higher than the energy absorbed by the WSTF specimens. Thus, we may conclude that the WSTF specimens absorbed approximately 1/5 of the original potential energy of the plummet.

I.7.2.   Stress Analysis of Specimen Deformation

The analysis of the stress distribution in the impact specimen is complicated. Among the items which must be considered to properly perform the stress analysis are: dynamic loading, elastic and plastic wave propagation, plasticity, finite boundaries, elastic support foundation, and the details of the development of contact between the striker pin and the specimen. Clearly, to properly model the impact event would require an extensive elasto/plastodynamic investigation using finite element methods. However, some insight can be gained into the stress state by considering a fully plastic analysis of the event and from a planar static analysis of the stress distribution.

I.7.2.1. Plastic Analysis: The Rigid Die Problem

Hill[41] considers the indentation of a finite-thickness medium by a rigid die to analyze indentation hardness testing. Following a velocity solution procedure, a slip-line field was constructed under the assumption that the rigid die radius was much smaller than the specimen thickness. Although this assumption is violated for the problem considered here, some of the results of Hill's analysis are of interest.

The first feature of Hill's analysis applicable here is the effect of a frictional resistance between the specimen and the (rigid) support plane. Hill found that the effect of such a resistance was to elevate the mean compressive stress at every point in the field by an amount F/h, where F is the frictional resistance and h is the specimen thickness. We can conclude that friction between the specimen and supporting cup in the oxygen compatibility test tends to aggravate the already severe stress state.

The second relevant feature of Hill's analysis is the calculation of the dependence of the resistive pressure (to penetration) on material properties. Hill found that $p \sim 2.97\sigma_{ys}$ after the yield point is reached.

107

The penetration pressures then vary from approximately 1690 MPa (245 ksi) for 2090-T81 to 633 MPa (92 ksi) for 8090-T3. In addition to the aforementioned assumption concerning specimen thickness, Hill also used the fact that the variation of the resistive pressure with depth (after the yield point) can often be neglected.

Finally, it should be noted that Hill found the calculation of load versus penetration depth to be meaningless since it can only be accomplished analytically by assuming the indenting surface remains flat. The calculation of the surface distortion and its effect on the load is the fundamental issue to properly calculate load-penetration behavior.

I.7.2.2. Static Analysis

To assess the difference in stress distribution caused by differences in the contact surface between the striker pin and the specimen surface, three finite element analyses were conducted. Although the dynamics of the problem are ignored here, some understanding can be gained concerning the influence of the striker-pin-end geometry on the stress distribution. As will be discussed, the differences are large.

The first analysis performed modeled the response of a 3.2-mm thick (0.125-in) impact specimen subjected to a uniform pressure loading over 12.7 mm (0.50 in) of its 17.5-mm (0.69-in) top surface. Vertical displacements were constrained to be zero across the bottom surface. Two hundred elements were used for the analysis. The specimen geometry and loading are shown in Figure I.7.2.

Results of the static analysis are presented in Figure I.7.3. The contours shown represent contours of constant equivalent (von Mises) stress. Recall that this analysis is elastostatic so the absolute values of stress are suitable only for comparison with subsequent analyses. Note in Figure I.7.3 that the maximum equivalent stress occurs over a broad region essentially beneath the loading area. The stresses then decrease as the vertical boundaries are approached.

The second analysis used the same geometry as above but with the loading shown in Figure I.7.4. This simulates the situation where the end of the pin is concave with the loading becoming point-like. Results for the equivalent stress distributions are shown in Figure I.7.5. Note in this case the maximum stresses occur under the point loads, as expected. However, the stress state in the rest of the body is quite different than the distributions from the uniform loading. With uniform loading, maximum stresses occurred over a broad region; under point loading, the maximum stresses are localized to an inverted cone extending from the lower surface to the load. Even at the bottom surface, a magnification of approximately two occurs in the stress with point loading.

A third static analysis was performed in order to assess the difference in stress distribution when the impact loading was eccentric, i.e., off the center of the specimen. As illustrated in Figure I.7.6, only the uniform-pressure case was considered. Results for the equivalent stress distribution are shown in Figure I.7.7. Stresses at the edge of the specimen closest to the impact show an increase in magnitude of approximately four over the on-center impact stresses.

108

We conclude from these brief analyses that the striker-pin geometry has considerable impact on the stress state in the specimen both in magnitude and in distribution. Also, off-center impacts can significantly alter the magnitude of stress at the edges of the specimen. Unless the pin geometry and loading eccentricity are close to being identical between tests, it is doubtful that similar states of stress are being imposed on the specimens.

I.7.2.3. Resiliency

The amount of rebound the impacting weight undergoes is a function of the moduli of resiliency of all the material stressed by the impact. The modulus of resilience of a material, U_R, is a measure of the stored elastic strain energy per unit volume. A simple definition of U_R is

$$U_R = \frac{\sigma_y^2}{2E} \qquad (7\text{-}17)$$

Note that both the yield stress and modulus of elasticity appear in this definition of U_R. Furthermore, in an energy calculation, recall that U_R is a volume quantity; in order to fully assess the stored elastic strain energy it is necessary to know the volume, or three-dimensional, distribution of stress. However, simplifying the stress distribution to a known, two-dimensional distribution can provide an estimate of the elastic energy.

I.7.2.4. Summary and Conclusions

Before stating the conclusions of the stress analysis, it is important to review the discrepancies between the actual problem and what was analyzed. Specifically, two aspects of the actual problem were not addressed quantitatively: (1) dynamic stress wave propagation, and (2) the elasticity of the supporting plane. Stress-wave effects are particularly important since the arrival time of the first reflected stress wave, estimated to be 1.2 μs, is well within the duration of the impact loading. The stress-wave interaction with the static stress field should therefore be considered.

Although the elastic properties of the supporting plane will not influence the static stress distribution to any great degree, it can have a large influence on the dynamics of the test. In terms of energy input into the specimen/support plane system, the elastic properties of the support can absorb a portion of the energy. Depending on the modulus of resilience of the particular support plane material, most of this energy would be returned in an elastic rebound of the impacting mass.

Our conclusions from the preliminary stress analysis are:

o Penetration pressures range from 1690 MPa (245 ksi) to 633 MPa (92 ksi). Calculation of load versus penetration depth was not possible.

o Friction forces aggravate the already severe stress state.
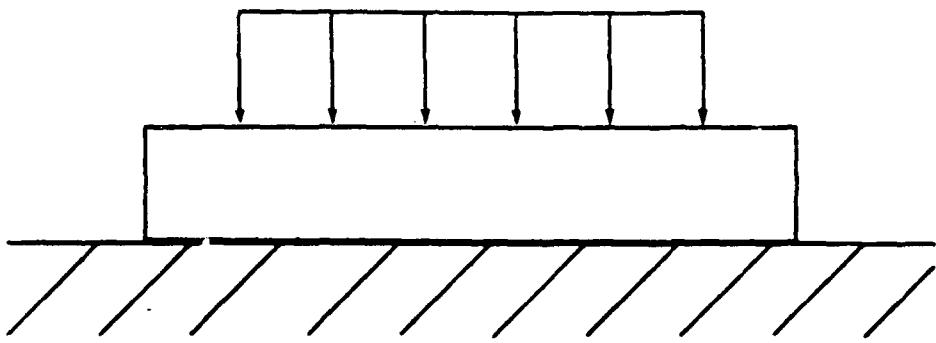
Figure I.7.2. Uniformly loaded impact specimen.
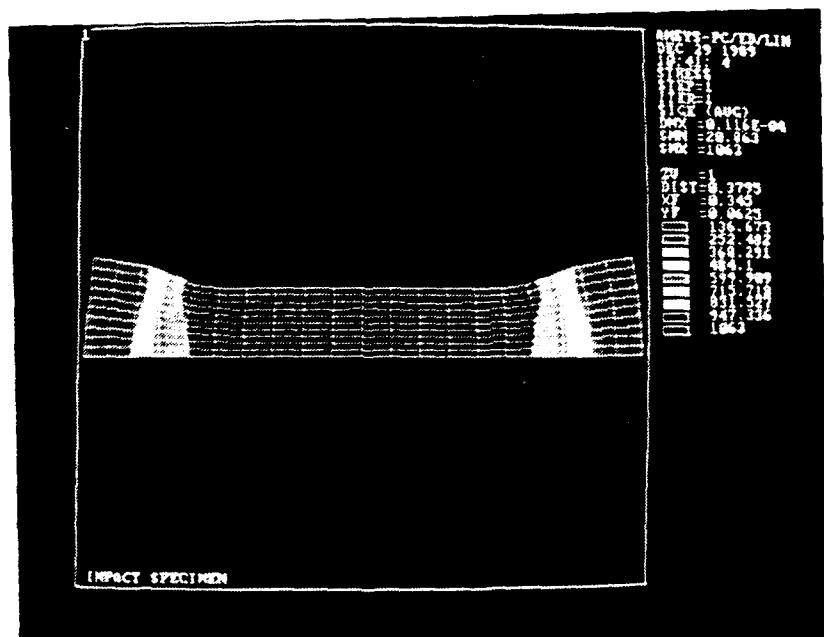
Figure I.7.3. Static von Mises stress distribution for the uniform
loading.

110
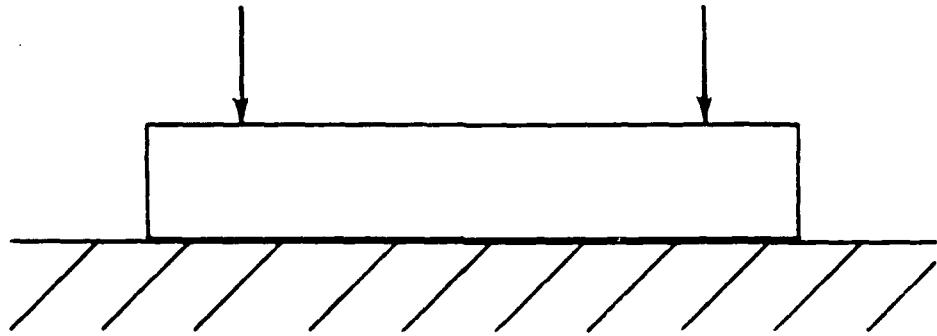
Figure I.7.4. Point loaded impact specimen. Point loading is due to striker pin concavity.
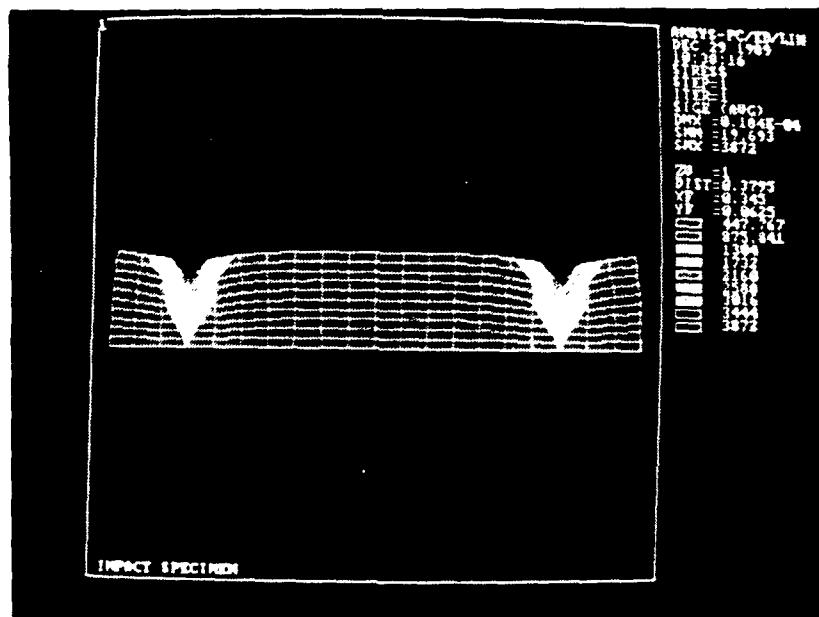
Figure I.7.5. Static von Mises stress distribution for the point loading.
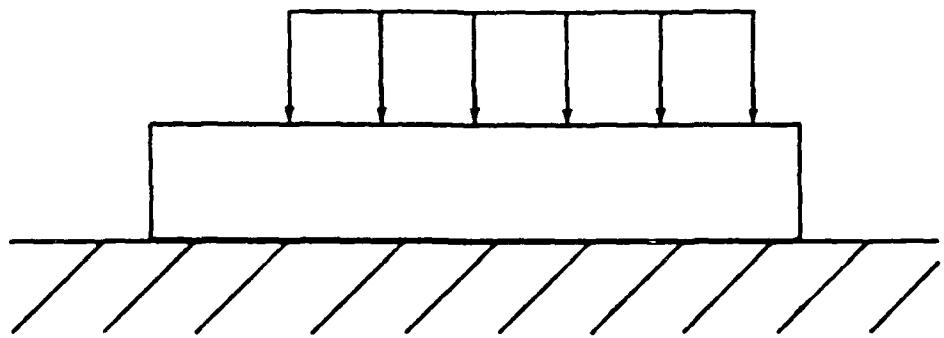
Figure I.7.6.   Eccentric, uniformly loaded impact specimens.
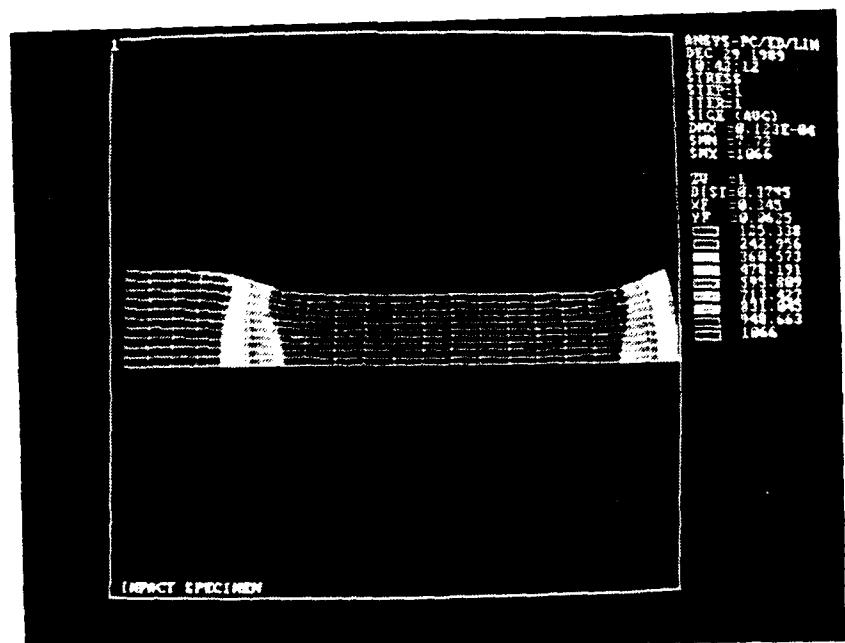
Figure I.7.7.   Static von Mises stress distribution for the eccentric
uniform loading.

112

o Striker-pin geometry and loading eccentricity can significantly
   alter the stress distribution.

o Stresses can be amplified as much as 10× from the concavity of the
   striker pin and 4× from loading eccentricity of 0.38 in (1.5 mm).

o An elasto-plastodynamic finite-element analysis is required
   to further assess the stress state.

I.8. DISCUSSION

I.8 1. Impact Energy

An overall energy balance of the mechanical impact test is

$$E_p - E_f - E_r + E_a \qquad (8\text{-}1)$$

where E_p is the potential energy of the plummet, E_f represents the combined frictional energies from plummet-guidance and pressure-seal contributions, E_r is the rebound energy of the plummet–striker-pin assembly that is dependent on the resiliency of the specimen/cup/support system, and E_a is the energy absorbed by the specimen. The impact energy to the specimen (E_i) is $E_p - E_f$ where E_f has been estimated to be zero for MSFC and SSFL equipment.

I.8.2. Absorbed Energy

The energy absorbed (E_a) by Al alloys of this study has been calculated (Section I.7.1.6.) from measurement of striker-pin penetration depth (to estimate specimen strain) and from an estimate of the stress in the specimen during impact from MSFC tests. From this calculation, E_a - 53 J was obtained.

Another estimate of E_a may be obtained using Eq. (8-1). We discussed the effect of rebound height on the rate of energy into the specimen in Section I.7.1.7. Similar arguments can be applied to calculate E_a with Eq. (8-1). In the MSFC tests E_r - 1/3 E_p and E_f - 0. Thus, E_a - E_p - E_r - 2/3 E_p - 65 J. The two estimates compare favorably, considering the approximations that are required for their calculation.

The estimated absorbed energies of specimens from WSTF are lower. In Section I.5.5. (Table I.5.10) our measurements of impact penetration depths suggest that E_a from WSTF is at least a factor of 3.5 less than that of MSFC for the Al alloys in our series of tests. Thus, from penetration depth measurements E_a - 65 J/3 5 - 19 J. Limited rebound height information from WSTF indicated that E_r - 2/3 E_p. Thus, considering rebound effects, but no friction, E_a - E_p - E_r - 1/3 E_p - 33 J.

We may assume that the distinctions between the two values (19 J and 33 J) from the two approaches are within data scatter. Or, we may use the difference to estimate a possible frictional losses. Following this course, E_p - 98 J, E_r - 2/3 E_p - 65 J, and we can let E_a - 19 J. Then, E_f - E_p - E_r - E_a - 14 J. Thus, the frictional losses of the WSTF pressurized mechanical impact facilities for LOX tests are estimated at about 15% of the potential energy of the plummet. A note of caution about this tentative conclusion: the variability of impact penetration depths exceeds 14% and the information on rebound heights at WSTF is limited. Thus, for this Interim Report our calculations must be assumed to be estimates.

Absorbed energy is suggested for uniform usage in the reporting of mechanical impact test results. Use of impact energy is not generic, since available test equipment does not have uniform specimen support and base structure. Thus, the resiliencies of the test equipment differ and the

114

absorbed energies of the specimen differ. Furthermore, calculation of impact energy in failure analysis of cryogenic tankage does not consider tank-wall resiliencies. The resiliencies are likely to differ considerably from that of test equiment. This makes test simulation extremely difficult in terms of impact energy, and consistent only in terms of absorbed energy. The absorbed energy of the specimens is the principal variable that affects heating and, thus, ignition.

Striker-pin irregularities, such as nicks, concavity of the impacting surface, and eccentricity of the impact with respect to the center of the specimen promote the localized deformation and heating.

I.8.3.   Localized Absorbed Energy
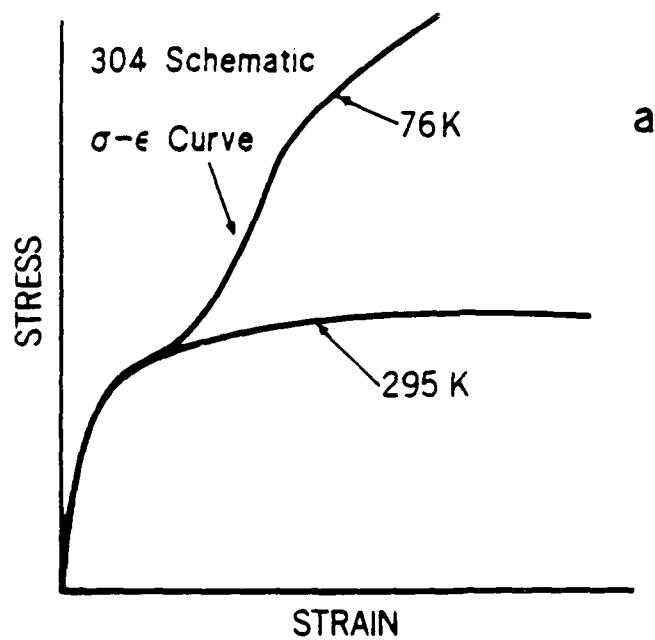
In most specimens tested at MSFC with impact energies of 98 J (corresponding to absorbed enegies of 65 J), the absorbed energy in the specimen was localized, not homogeneous. Most specimens at this high impact energy (from MSFC and SSFL tests) showed shear lips, indicative of macroscopic anisotropic plastic deformation. Many MSFC specimens had irregular impact perimeters, caused by large nicks on the circumference of the striker pin. Additionally, the striker pins used in tests that produced ignition, which were examined by NIST, had concave impact surfaces. We have estimated the possible increases of absorbed energies from these test inconsistencies: eccentricity (of 1.5 mm)—4×; concavity—10×; shear lip—reduction at bottom of penetration depth, but indicative of an increase in anisotropic flow stress of about 1.5×.

I.8.4.   Specimen Deformation
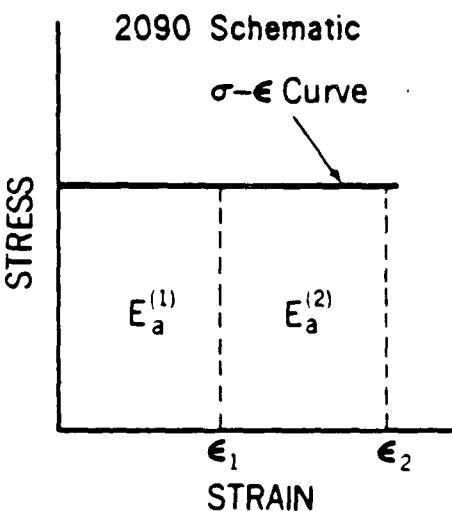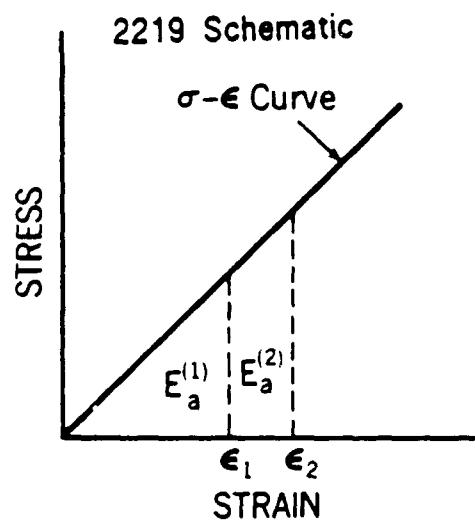
All specimens exposed to absorbed energies of about 65 J showed extensive deformation, similar to tensile or fracture toughness specimens near (or at) fracture. Deformation features of each alloy are summarized: 8090-T3—extensive deformation with large shear lips and specimen perimeter microcracking; 2090-T81—splitting, intragranular delaminar cracking; 2219-T851—extensive vertical microcracking on specimen perimeter; 2219-T37—extensive shear at indentation lip and macroscopic delamination(s).

I.8.5.   Influence of Alloy Stress-Strain Curves

Several apparent anomalies in the Bransford et al.[18] report and in our data can be explained if one considers the stress-strain curves of the alloy specimens. In the Bransford et al. report the values of energy absorbed when testing at cryogenic temperatures are consistently about half of those absorbed at room temperature for equivalent impact energies. We have concluded earlier in this report that friction is not a factor in MSFC and

Figure I 8 1. Alloy 304 stress-strain curves (a). Conceptual stress-strain curves illustrating the distinction between 2219 and 2090 alloys (b).

SSFL tests. One would expect the resiliency to increase at low temperatures as the ratio σ_y^2/E increases, where E is the Young's Modulus. This ratio increases for 2219 by about 10%; for 2090 it remains almost constant. Therefore, increased rebounds cannot account for the difference in absorbed energy. The temperature-dependent effects must come from the change of mechanical response of the specimens; i.e., the temperature dependence of the strain-stress curves. Figure I.8.1a schematically portrays the differences between room temperature and 76 K stress-strain characteristics for alloy 304. If there are equivalent impact energies (and equivalent absorbed energies) at each temperature, and if the energies are sufficiently high, the resultant strain at 76 K will be much less (considering only equivalent areas under the stress-strain curves). Thus, for equivalent absorbed energies, the depth of striker pin penetration is less at 76 K, compared to room temperature.

Another "anomaly" which initially puzzled us was the difference in the ratios of impact penetration depths at MSFC and WSTF for the two alloys 2219 and 2090 (see Table I.5.10). These also can be explained if one notes the differences in the stress-strain curves of the two alloys. Alloy 2090-T81 exhibits very little work hardening; its stress-strain curve in the plastic deformation region is practically horizontal. In contrast, both 2219 alloys show much more work hardening; their average ratios of σ_u/σ_y are about 1.3. Schematically, we exaggerate the stress-strain curve distinctions in Figure I.8.1b. In the first stress-strain curve (more typical of alloy 2219), if $E_a^{(1)} = 1/2\ E_a^{(2)}$, the resultant strain ratios, (ϵ_2/ϵ_1), will be about 1.4. In the second type of curve, more indicative of alloy 2090, if $E_a^{(1)} = 1/2\ E_a^{(2)}$, $\epsilon_2/\epsilon_1 = 2$. In comparing MSFC with WSTF calibration block tests, E_a (MSFC)= $3.5 E_a$ (WSTF). Thus, differences in ratios from 3.5 (for 2219 alloys) to 5—8 (for 2090 alloys) reflect the influences of the absorbed energy differences on the two types of stress-strain curves.

I.8.6. Statistical Problems with Impact Tests

The NASA NHB 8060.1B document for LOX compatibility requires no reactions of the material in 20 tests at an impact energy of 98 J (72 ft·lbs). The probability, P, of k reactions in a number of tests, n, for a material with a reaction probability, p, is

$$P = \frac{n!}{k! \cdot (n-k)!} \cdot p^k \cdot (1-p)^{n-k} . \qquad (8-2)$$

This equation is derived in many statistics textbooks, and may be used, for example, to determine that the probability, P, is 0.00000095 that in a series of 20 coin tosses (n=20), heads (p = 0.50) would never come up (k = 0). Such an occurrence would be very rare, in accord with common sense. However, when considering material reactivity, if the probability of a reaction at an absorbed energy of 65 J (72 ft·lbs) is 10% (p = 0.10), then in 20 tests, the probability that no reactions would be observed and that the NASA requirement would be met is P = .12 or 12%. A p of 0.05 (5% reaction probability) would give a 36% chance that the requirement of no reactions in 20 tests would be met. Thus, comparing materials at an absorbed energy level where the reaction probability is significantly below 50% is inherently difficult under NASA NHB 8060.1B. One solution is to increase the number of tests: if 60 tests are carried out on a material with a 5% reaction probability at a given energy level, P = 0.05, so that

one could state that with a 95% confidence level, the material was not reactive when impacted at that energy level. Another alternative, obviously, is to increase the absorbed energy level so that p ~ 0.50, as in the coin toss example above. Several statistical methods can be used to determine the 50% reaction energy from a smaller number of tests (see Moffett et al.[17]).

I.8.7. Specimen Ignition

Ignition of specimens that were tested at MSFC required three ingredients: (1) extensive local deformation, (2) the presence of oxygen, and (3) an oxide-free surface. The ignition sources are summarized: most of the ignitions of alloys 8090-T3, 2219-T851, and 2219-T37 originated at shear lips; the position provides heavy localized deformation, exposure to oxygen, and an oxide-free surface from the scraping of the pin on the deforming specimen. One ignition (2219-T851) originated on the specimen perimeter: in this alloy there was extensive microcracking on the perimeter coupled with microscopic metal pultrusion. The pultruded metal provides a region of heavy deformation, oxygen accessibility, and an oxide-free surface. The third source of ignitions were splits (2090-T81, 8090-T3) where the open crack led to the presence of oxygen, the extensive local deformation provided specimen heating, and the entire fresh crack was free of oxide.

Specimens tested at SSFL experienced most of the conditions described above, but they failed to ignite. This leads us to the conclusion that, for ignition, the amount of local deformation was not sufficient in the SSFL specimens. To produce localized melting, as our calculations and observations indicated, the deformation needed an additional stress concentration. This was provided by the striker-pin irregularities and/or the added eccentricity of impact to the specimens in the MSFC tests. The more ideal test conditions of SSFL did not produce sufficient local deformation in the specimens to produce ignition.

I.8.8.   Comparison of Al-Li Alloys with 2219

From mechanical impact tests, Al-Li alloys (2090, 8090) are comparable, but not superior to, alloy 2219. Under absorbed energies of about 13 J (WSTF), no ignitions were observed. Under absorbed energies of 53–65 J with superior test control (SSFL) no ignitions were observed in 2090. Under absorbed energies of 53–65 J with test variables conducive to highly localized stresses (and thus, localized deformation and heating) at MSFC, some specimens of all alloys ignited.

From promoted-combustion tests, the flammability of Al-Li alloys is superior to that of alloy 2219. The critical GOX pressure to sustain combustion in Al-Li alloys is above 80 psi; for both tempers of 2219 this critical GOX pressure is about 40 psi.

I.8.9. NASA Standard NHB 8060.1B (Paragraph 413, test 13)

This standard currently has deficiencies that permit wide variations in significant test parameters between the test laboratories. The major in-adequacies are listed here:

1. Specifications are required for striker-pin geometry and surface finish.

2. Specifications are required for maximum allowable eccentricity of striker-pin impact area with specimen center.

3. Specimen-cup width should be increased by about 0.0625 in $(1.6 \times 10^{-3}$ m) to prevent frictional effects for specimens that deform extensively.

4. New cleaning and quantitative surface-finish specifications for metallic specimens are recommended.

5. Temperature measurement and control of the specimen and its environment are not adequately defined.

6. Impact energy (E_i) should be redefined; it should include the frictional contributions. That is, $E_i - E_p - E_f$.

7. Results should be stated in terms of absorbed energy, $E_a - E_i - E_r$, not impact energy. Knowledge of the absorbed energy of the specimen permits comparison between laboratories and application to failure analyses.

8. Use of absorbed energy as a basis for reporting test results and for specifying test requirements will have beneficial results: (1) interlaboratory results will be comparable, (2) failure analyses can be realistically compared to test data, (3) alloy-to-alloy comparisons will be meaningful. (Currently, Al alloys are judged inferior, but, if their lower resiliency is considered, this would probably not be the case.)

9. Twenty specimens are not sufficent, statistically, when the probabililty of ignition is less than about 0.20 (the case of Al alloys at 65 J and LOX environment). As discussed in Section 8.6, more specimens or an increased energy are required to increase the confidence level of the results.

10. Cup material should be standarized among test facilities to ensure comparable absorbed energies.

I.8.10. Laboratory Testing Procedures

Currently, there are major differences in the test procedures and equipment of the laboratories that perform LOX and GOX pressurized mechanical impact tests for material qualification following NASA specification NHB 8060.1B. Major areas of disparity are: (1) impact energy and absorbed energy (WSTF is lower by at least a factor of 3.5 than MSFC in absorbed energy); (2) quality control of striker-pin surface finish

119

and concavity of impact surface (MSFC impacted specimens showed more evidence of lack of control of these variables); (3) better or more consistent control of eccentricity of striker-pin impact indentation with specimen (WSTF has less control of this variable); and (4) temperature control of specimen prior to impact (currently only WSTF has a thermocouple in position close to the specimen).

Revision of NASA NHB 8060.1B (Paragraph 413, test 13) following the recommendation of this report would ensure better laboratory conformance in the above parameters.

I.10.   ACKNOWLEDGMENTS

I.11. REFERENCES

1. Weeks, L. M., "Flammability, Odor, and Offgassing Requirements and Test Procedures for Materials in Environments That Support Combustion, NASA, Office of Space Transportation Systems, Washington, DC, Report No. NHB 8060.1B, 107 pp. (1981).

2. Reed, R. P., and Walsh, R. P., "Low-Temperature Deformation of Copper and an Austenitic Stainless Steel," in Advances in Cryogenic Engineering, Vol. 32, Eds. R. P. Reed and A. F. Clark, Plenum Press, NY, 303-312 (1986).

3. Willner, E., "Aluminum-Lithium Alloy 8090," Structural and Materials Engineering Bulletin, Lockheed Missiles and Space Company, Huntington Beach, CA, 27 pp. (1989).

4. Wan, C. C., Carter, R. V., Henderson, G. W., Uht, J. C., "Tensile Properties of 8090 Al-Li Alloy at Elevated and Cryogenic Temperatures," Aerospace Corporation, El Segundo, CA, Report No. ATM-89(8486)-1, 48 pp. (1989).

5. Goodyear, M. D., "ALCOA Alloy 2090," ALCOA Green Letter, Aluminum Company of America, Alcoa Center, PA, Report No. GL 226 (1989).

6. Tack, W. T., and Loechel, L. W., "Weldalite 049: Applicability if a New High-Strength, Weldable Al-Li-Cu Alloy," in Aluminum-Lithium Alloys V, Eds. E. A. Starke, Jr. and T. H. Sanders, Jr., Materials and Components Engineering Publications Ltd., Birmingham, England, 1457-1467 (1989).

7. "Metallic Materials and Elements for Aerospace Vehicle Structures, Vol. 1," Department of Defense, Washington, DC, MIL-HDBK-5E (1987).

8. Walsh, R. P., and Reed, R. P., National Institute of Standards and Technology, Boulder, CO, private communication (1989).

9. Sato, T., Takahashi, T., "Precipitation Phenomena and Mechanical Properties in an Al-Li-Cu-Mg-Zr Alloy," Journal of the Japanese Institute for Light Metals 36, 728-736 (1986).

10. Papazian, J. M., Bott, G. G., and Shaw, P., "Influence of Forming in the T3 Condition on Properties of 2090-T8X, 2091-T8X, and 8090-T8X," Journal de Physique, Colloque 3 48-C3, 231-237 (1987).

11. Lucks, C. F., Matolich, J., and Van Valzor, J. A., "The Experimental Measurement of Thermal Conductivities, Specific Heats, and Densities of Metallic, Transparent, and Protective Materials, Part III," Battelle Memorial Institute, Columbus, OH, Report No. TR 6145, 72 pp. (1954).

12. Lucks, C. F., and Deem, H. W., "Thermal Properties of Thirteen Metals," ASTM Special Technical Publication No. 227, American Society for Testing and Materials, Philadelphia, PA (1958).

13. Corruccini, R. J., "Properties of Materials at Low Temperatures, Part I," Chemical Engineering Progress 53, 262-267 (1957).

14. Rhodes, B. L., Moeller, C. E., and Sauer, H. J., "An Apparatus for Determining Thermal Conductivity of Solids from 20 to 600 K," Cryogenics 5, 17-20 (1965).

15. Hust, J. G., and Lankford, A. B., "Thermal Conductivity of Aluminum, Copper, Iron, and Tungsten for Temperatures from 1 K to the Melting Point," National Bureau of Standards, Boulder, CO, Report No. NBSIR 84-3007, 256 pp. (1984).

16. Bryan, C. J., "NASA Mechanical Impact Testing in High-Pressure Oxygen," in Flammability and Sensitivity of Materials in Oxygen-Enriched Atmospheres, ASTM Special Technical Publication 812, Ed. B. L. Werley, American Society for Testing and Materials, Philadelphia, PA, 9-42 (1983).

17. Moffett, G. E., Schmidt, N. E., Pedley, M. D., and Linley, L. "An Evaluation of the Liquid Oxygen Mechanical Impact Test," in Symposium on Flammability and Sensitivity of Materials in Oxygen-Enriched Atmospheres: 4th Volume, ASTM Special Technical Publication 1040, Eds. J. M. Stoltzfus, F. J. Benz, and J. S. Stradling, American Society for Testing and Materials, Philadelphia, PA (1989).

18. Bransford, J. W., Bryan, C. J., Frye, G. W., and Stohler, S. L., "LOX/GOX Mechanical Impact Tester Assessment," National Aeronautics and Space Administration, Washington, DC, Report No. NASA TM 74106, 104 pp. (1980).

19. Steinberg, T. A., Rucker, M. A., and Beeson, H. D., "Promoted Combustion of Nine Structural Metals in High-Pressure Gaseous Oxygen: A Comparison of Ranking Methods," in Symposium on Flammability and Sensitivity of Materials in Oxygen-Enriched Atmospheres: 4th Volume, ASTM Special Technical Publication 1040, Eds. J. M. Stoltzfus, F. J. Benz, and J. S. Stradling, American Society for Testing and Materials, Philadelphia, PA (1989).

20. "Standard Test Method for Determining Ignition Sensitivity of Materials to Mechanical Impact in Pressurized Oxygen Environments," American Society for Testing and Materials, Philadelphia, PA, 996-1007 (1984).

21. "Cleanliness of Components for Use in Oxygen, Fuel, and Pneumatic Systems, Specification for," George C. Marshall Space Flight Center, Huntsville, AL, Report No. MSFC-SPEC-164A, 28 pp. (1970).

22. Bransford, J. W., and P. A., Hurley, "High Pressure DTA/TGA System for Studying the Oxidation of Metallic Materials," National Institute of Standards and Technology, Boulder, CO, Personal Communication (1990).

23. Rhein, R. A., "Aluminum Combustion: A Review," Naval Weapons Center, China Lake, CA, Report No. NWC TP 6629, 42 pp. (1985).

24. Macek, A., "Fundamentals of Combustion of Single Aluminum and Beryllium Particles," in Symposium on Combustion, Vol. 11, 203-214 (1966).

25. Clark, A. F., and Hust, J. G., "A Review of the Compatability of Structural Materials with Oxygen," AIAA Journal 12, 441-454 (1974).

26. Grosse, A. V., and Conway, J. B., "Combustion of Metals in Oxygen," Ind. Eng. Chem. 50, 663-672 (1958).

27. Reynolds, W. C., "Investigation of Ignition Temperatures of Solid Metals," National Aeronautics and Space Administration, Report No. NASA TN-D-182 and AD-227648 (1959).

28. Gordon, A. S., and others, "Techniques for the Study of the Combustion of Metals," AIAA Journal 6, 577-583 (1968).

29. Markstein, G. H., "Combustion of Metals," AIAA Journal 1, 550-562 (1963).

30. Wilson, R. P., Jr., and Williams, F. A., "Experimental Study of the Combustion of Single Aluminum Particles in Oxygen-Argon," Proceedings of the 13th International Symposium on Combustion, 833-845 (1971).

31. Jacobson, M., and others, "Explosivity of Metal Powders," Bureau of Mines, Report No. RI 6516 (1976).

32. Rolsten, R. F., and others, "Hypervelocity Impact on Pressurized Structure," General Dynamics/Astronautics, Report No. AE 62-020 and AD-660566 (1962).

33. Christian, J. L., Chafey, J. E., Hurlich, A., Watson, J. F., and Witzell, W. E., "Compatibility of Metals and Cryogenic Liquids," Metal Progress, April, pg 100 (1963).

34. Kuehl, D. K., "Ignition and Combustion of Small-Diameter Al Wires," Western States Section, Combustion Institute, Paper WSS/CI 64-21 (1964).

35. Liedtke, L., "Progress Report for December 1984 on Metal Fire Characterization Study," Naval Weapons Center, China Lake, CA, Report No. NWC RM 3244-006 (1985).

36. Kutateladze, S. S., "Fundamentals of Heat Transfer," Academic Press Inc., New York, NY, 485 pp. (1963).

37. Reed, R. P., and Simon, N. J., "Discontinuous Yielding During Tensile Tests at Low Temperatures," in Advances in Cryogenic Engineering--Materials, Vol. 36, Eds. R. P. Reed and F. R. Fickett, Plenum Press, New York, NY (1990).

38. Brentari, E. G., Giarratano, P. J., and Smith, R. V., "Boiling Heat Transfer for Oxygen, Nitrogen, Hydrogen, and Helium," Technical Note 317, National Bureau of Standards, Boulder, CO (1965)

125

APPENDIX A

Excerpts from NASA NHB 8060.1B

on Cleaning of Specimens for LOX

Compatibility Tests (September 1981).

PREFACE

Date: September 1981

This publication establishes uniform material selection, evaluation and control criteria for all materials that are under consideration for use in and around space vehicles, ground support equipment and facilities during assembly, test and flight operations. It supersedes the February 1974 issue of NHB 8060.1A. Included herein are revised criteria for material applications in high pressure LOX/GOX systems and in combustion supporting environments other than oxygen. Also included are revised criteria for offgassing testing of materials, a new procedure for black box testing, and other clarification changes. This publication provides:

a. Standard requirements for control of flammability, odor and offgassing of materials to be used in the design, development, and testing of manned space vehicles, and of payloads and their related equipment which will fly in habitable portions within such vehicles.

b. Guidelines and directions for material selection.

c. Testing procedures for the candidate materials.

The provisions of this handbook are applicable to the NASA installations responsible for hardware design, development and testing of hardware described above under item a.

Provisions of this handbook will be included as applicable in all future contracts and programs involving space vehicles and payloads, and their equipment which will fly in habitable portions within such vehicles. However, the supply of this document within NASA is limited. Therefore, for those procurement actions involving only a certain portion (or portions) of this handbook, the cognizant NASA installations shall abstract or reproduce only such portions as applicable to a given RFP or contract action in lieu of furnishing copies of this handbook.

Any questions or comments concerning the provisions of this document should be directed to Reliability, Quality and Safety (Code MR), NASA Headquarters.

NHB 8060.1A dated February 1974 is cancelled.

L. Michael Weeks
Acting Associate Administrator
for Space Transportation Systems

4.6 CLEANING MATERIALS

4.6.1 Rinse Water

Rinse water shall be of the distilled or deionized variety conforming to the following:

Conductivity:	50,000 ohm-cm minimum resistance at 25C
pH:	5.0 - 7.5
Chlorides:	1.0 ppm by weight (maximum)
Surface Tension:	71.71 dynes per cm (minimum) at $20^{o}C$.

4.6.2 Detergent

Detergent shall be added to deionized or distilled water in accordance with concentration requirements of Section 4.7.3 and then passed through a 25 micron (absolute) filter, or better, prior to use, for flushing/decontamination purposes. The following detergent types are acceptable: Liqui-Det #2, Turco 4215S, Ivory liquid detergent.

4.6.3 Cleaning Solvents

Cleaning solvent shall be trichlorotrifluoroethane (Freon 113) for cleaning test fixture and apparatus and shall be filtered through a 4.5 micron (absolute) filter, or better, prior to use. The NVR content of the solvent shall not exceed 1.0 mg per 200 ml. Nonmetallic materials shall be suitably cleaned with water and mild detergent solution.

4.6.4 Nitrogen

Gaseous nitrogen used for drying purposes shall conform to the following:

Purity:	99.5% by volume (minimum).
Oxygen Content:	0.5% by volume (maximum).
Hydrocarbons, as Methane:	58.3 ppm by volume (maximum).
Moisture Content:	26.3 ppm by volume (maximum).
Filtration:	25 microns or less.

4.7 CLEANING PROCEDURE

4.7.1 Samples shall be first inspected for any signs of abrasion, etc., and brushed clean, using a nylon brush.

4.7.2 The material specimens shall then be decontaminated, using cold tap water. Flush with water until pH of effluent is within 0.5 pH unit of influent, but do not flush less than 2 minutes.

4.7.3 Perform detergent cleaning using 1/2 to 1 oz. of detergent/gallon of deionized water. Assist cleaning with nylon brush. Immersion time shall be 5 $\pm$ 1 minutes at bath temperature of 120°-150°F. Agitation, not ultrasonic, shall be effected for a period not less than 30 seconds prior to removal from detergent bath.

4.7.4 Soak and agitate for not less than 2 minutes with deionized water (see Section 4.6.1) 140°F maximum until no evidence of detergent solution is apparent when checked by a suitable ASTM or equivalent method.

4.7.5 Rinse-spray using deionized water for at least ten thorough applications.

4.7.6 Place samples in clean Petri dish.

4.7.7   Purge for 5 minutes with nitrogen (GN_2) conforming to Section 4.6.4, filtered through a membrane filter not exceeding a 4.5 micron pore size, and package in a polyethylene or equivalent package.

4.7.8   Samples have now been uniformly cleaned and are ready for testing.

APPENDIX B

Promoted Combustion Tests at White Sands

Test Facility.

J. Stoltzfus, White Sands Test Facility, NASA

(December 1989).

Objective

To evaluate the relative flammability of several aluminum alloys in oxygen by determining the minimum pressure at which a standard test sample combusts completely.

Test System Description

The test chamber (Figure 1) was a 50 cu.ft. pressure vessel with a maximum working pressure of 110 psi. The test sample was mounted inside the chamber in a vertical orientation supported at the top. A magnesium promoter was mounted on the bottom end of the test sample and was initiated by a nichrome heater wire (Figure 2). The test sample, promoter, heater wire, and sample mount were located inside a copper drip pan/splash shield to protect the chamber from burning debris ejected from the test sample. Aviator's breathing oxygen (ABO) per MIL-0-27210E was supplied to the test chamber from a K-bottle source.

Test Procedure

o   1/8-inch diameter by 5-inch long samples were machined from the stock provided by NIST
o   The samples were cleaned per NHB8060.1b Appendix C
o   A test sample was loaded into the chamber as shown in Figure 2
o   A pretest video recording of the sample was made
o   Air was evacuated from the test chamber using a vacuum pump
o   The test pressure was established using ABO and allowed to stabilize for 2 minutes
o   The video recorder was turned on
o   Power was applied to the heater wire and the test was observed
o   A posttest video recording of the sample was made

Test Results and Discussion

The test results are shown in Table 1. The alloys tested for this project to date are 8090-T3, 2219-T851, 2219-T37, and 2090-T8E41. Some data from tests conducted using samples made from 5086 and 6061 aluminum are also included. The minimum pressure at which 2219-T851 and 2219-T37 burned completely was 30 psia. However, these alloys may burn completely at lower pressures if more tests are performed since they burned as much as 4.7 and 6.4 cm respectively during tests performed at 25 psia. The two lithium-bearing alloys, 8090-T3 and 2090-T8E41, did not burn completely at test pressures as high as 80 psia.

It was anticipated that the since lithium is highly reactive and that copper is not that the addition of these elements to aluminum would decrease the minimum pressure required for complete combustion in the case of lithium and increase the minimum pressure required for complete combustion in the case of copper. However, the opposite occurred. (Refer to Table 2 for composition of alloys.) Some theories postulated to explain this result are: (1) Copper may increase the heat transfer for the burning portion of the rod to the unburned rod due to its high thermal conductivity, (2) Li_2AlO_4 may be produced in the burning process, which has a very high melting temperature. This product

135

may freeze out very quickly providing an endothermic process to
quench the flame propagation. Keep in mind, though, that these
are just theories. The important thing to note is that the
lithium bearing alloys appear to be less flammable than the 2219.

RESULTS

TEST PRESSURE (PSIA)

LENGTH OF SAMPLE CONSUMED (cm)

ALLOY	15	20	25	30	35	40	45	50	55	60	65	70	75	80
2219-T37[b]			0.2, 6.4	8.0, CB		6.4				9.7, CB	CB	CB		CB
2219-T851[b]	0.6	3.4, 0.3, 12.3	3.5, 4.7, 1.6	CB[c]						CB				
2219-T87[b]			CB	10.0, CB										
8090-T3[a]			2.1	1.7		2.0		1.6		3.8, 1.6				3.5, 3.3, 3.6
8090-T151[b]														3.1, 2.6, 2.8
8090-T8771[b]														3.4, 3.5, 3.4
Weldalite 049-T351[b]				2.2										3.1, 1.5, 3.3
Weldalite 049-T651[b]														3.7, 3.2, 3.1
2090-T81[b] (1/2" Plate)				0.2						3.4				2.8, 3.1, 3.5

a Initial Sample Length = 12.2 cm
b Initial Sample Length = 14.7 cm
c Sample Completely Consumed

d Unpublished WSTF Data
e Bennins, Zubrenski, Le (1988)

139

TABLE 2. COMPOSITION OF ALLOYS

ALLOY	Ag	Al	Cr	Cu	Fe	Li	Mg	Mn	Si	Ti	Zn	Zr	Other
2090		93.2 - 94.6	0.05	2.4 - 3.0	0.12	1.9 - 2.6	0.25	0.05	0.10	0.15	0.10	0.08 - 0.15	0.20
2219		93		6.3				0.3		0.06		0.18	0.1
8090		93 - 95	0.10	1.0 - 1.6	0.30	2.2 - 2.7	0.6 - 1.3	0.10	0.20	0.10	0.25	0.04 - 0.16	0.20
Weldalite	0.4	91.5		6.3		1.3	0.4					0.14	
5086		95.4	0.15				4.0	0.4					
6061		95.9 - 98.5	0.15 - 0.35	0.15 - 0.40	0.7		0.8 - 1.2	0.15	0.40 - 0.80	0.15	0.25		

140

APPENDIX C

Physical Measurements on Impacted LOX

Compatibility Specimens.

Table C.1. Physical Measurements on Alloy 8090-T3 Specimens in LOX Ambient Environment.

Test Facility	Plate Thickness, in (mm)	Specimen Thickness, in (mm)	Potential Energy ft-lbs (kg-m)	Number of Specimens Impacted	Number of Specimens Measured	$\bar{d}^*$, in (mm)	$\bar{c}^{**}$, in (mm)	Other † (S,C,D,R,L)
WSTF	1/2 (12.7)	1/8 (3.2)	72 (10)	2	2	0.0234 (0.5944)	0.069 (1.75)	0,0,0,0,0
			58 (8)	2	2	0.0158 (0.4013)	0.039 (1.00)	0,0,0,0,0
			43 (6)	2	2	0.0162 (0.4115)	0.079 (2.00)	0,0,0,0,0
WSTF	1/2 (12.7)	1/16 (1.6)	72 (10)	2	2	0.0108 (0.2743)	0.039 (1.00)	1,1,0,0,0
			58 (8)	2	2	0.0082 (0.2083)	0.094 (2.38)	0,0,0,0,0
			43 (6)	2	2	0.0067 (0.1702)	0.079 (2.00)	0,0,0,0,0

* d = average depth of impact

** c = average eccentricity of impact, difference between the impact and specimen centers

† # of Splits(S), # of Cracks(C), # of Delaminations(D), # of Reactions(R), # of Shear Lips(L)

143

Table C.2. Physical Measurements on Alloy 8090-T3 Specimens in LN$_2$ Ambient Environment.

Test Facility	Plate Thickness, in (mm)	Specimen Thickness, in (mm)	Potential Energy ft-lbs (kg-m)	Number of Specimens Impacted	Number of Specimens Measured	$\bar{d}$*, in (mm)	$\bar{c}$**, in (mm)	Other † (S,C,D,R,L)
WSTF	1/2 (12.7)	1/8 (3.2)	72 (10)	2	2	0.0235 (0.5969)	0.039 (1.00)	0,0,1,0,0
			58 (8)	2	2	0.0232 (0.5893)	0.098 (2.50)	0,0,0,0,0
			43 (6)	2	2	0.0105 (0.2667)	0.049 (1.25)	0,0,0,0,0
WSTF	1/2 (12.7)	1/16 (1.6)	72 (10)	2	2	0.0106 (0.2692)	0.079 (2.00)	1,0,0,0,0
			58 (8)	2	2	0.0064 (0.1626)	0.098 (2.50)	0,0,0,0,0
			43 (6)	2	2	0.0065 (0.1651)	0.098 (2.50)	0,0,0,0,0

* d = average depth of impact
** c = average eccentricity of impact, difference between the impact and specimen centers
† # of Splits(S), # of Cracks(C), # of Delaminations(D), # of Reactions(R), # of Shear Lips(L)

144

Table C.3. Physical Measurements on Alloy 2090-T81 Specimens in LOX Ambient Environment.

Test Facility	Plate Thickness, in (mm)	Specimen Thickness, in (mm)	Potential Energy ft-lbs (kg-m)	Number of Specimens Impacted	Number of Specimens Measured	$\bar{d}^*$, in (mm)	$\bar{c}^{**}$, in (mm)	Other † (S,C,D,R,L)
WSTF	1/2 (12.7)	1/8 (3.2)	72 (10)	2	2	0.0072 (0.1829)	0.071 (1.8)	0,0,0,0,0
			58 (8)	2	2	0.0044 (0.1118)	0.098 (2.5)	0,0,0,0,0
			43 (6)	2	2	0.0015 (0.0381)	0.0039 (1.0)	0,1,0,0,0
WSTF	1/2 (12.7)	1/16 (1.6)	72 (10)	2	2	0.0046 (0.1168)	0.059 (1.5)	0,0,0,0,0
			58 (8)	2	2	0.0032 (0.0813)	0.079 (2.0)	0,0,0,0,0
			43 (6)	2	2	0.0007 (0.0178)	0.071 (1.8)	0,0,0,0,0
WSTF	3/4 (19.0)	1/8 (3.2)	72 (10)	2	2	0.0037 (0.0940)	0.039 (1.0)	0,0,0,0,0
			58 (8)	2	2	0.0006 (0.0152)	0.110 (2.8)	0,0,0,0,0
			43 (6)	2	2	0.0034 (0.0864)	N/A	0,0,0,0,0
WSTF	3/4 (19.0)	1/16 (1.6)	72 (10)	2	2	0.0009 (0.0229)	0.098 (2.5)	0,0,0,0,0
			58 (8)	2	2	0.0011 (0.0279)	0.079 (2.0)	0,0,0,0,0
			43 (6)	2	2	0.0032 (0.0813)	0.079 (2.0)	0,0,0,0,0

* d = average depth of impact
** c = average eccentricity of impact, difference between the impact and specimen centers
† # of Splits(S), # of Cracks(C), # of Delaminations(D), # of Reactions(R), # of Shear Lips(L)

145

Table C.4. Physical Measurements on Alloy 2090-T81 Specimens in LOX Ambient Environment (Rebound Catcher Used).

Test Facility	Plate Thickness, in (mm)	Specimen Thickness, in (mm)	Potential Energy ft-lbs (kg-m)	Number of Specimens Impacted	Number of Specimens Measured	$\bar{d}$*, in (mm)	$\bar{c}$**, in (mm)	Other † (S,C,D,R,L)
WSTF	3/4 (19.0)	1/8 (3.2)	72 (10)	2	2	0.0023 (0.0584)	0.071 (1.0)	0,0,0,0,0
			58 (8)	2	2	0.0045 (0.1143)	0.197 (5.0)	0,0,0,0,0
			43 (6)	2	2	0.0027 (0.0686)	0.079 (2.0)	0,0,0,0,0
WSTF	3/4 (19.0)	1/16 (1.6)	72 (10)	2	2	0.0026 (0.0660)	0.079 (2.0)	0,1,0,0,0
			58 (8)	2	2	0.0058 (0.1473)	0.071 (1.8)	0,0,0,0,0
			43 (6)	2	2	0.0017 (0.0432)	0.079 (2.0)	0,0,0,0,0

* d = average depth of impact
** c = average eccentricity of impact, difference between the impact and specimen centers
† # of Splits(S), # of Cracks(C), # of Delaminations(D), # of Reactions(R), # of Shear Lips(L)

146

Table C.5. Physical Measurements on Alloy 2090-T81 Specimens in LN_2 Ambient Environment.

Test Facility	Plate Thickness, in (mm)	Specimen Thickness, in (mm)	Potential Energy ft-lbs (kg-m)	Number of Specimens Impacted	Measured	$\bar{d}^*$, in (mm)		$\bar{c}^{**}$, in (mm)		Other † (S,C,D,R,L)
WSTF	3/4 (19.0)	1/8 (3.2)	72 (10)	2	2	0.0087	(0.2210)	0.138	(3.5)	0,0,0,0,0
			58 (8)	2	2	0.0019	(0.0483)	0.020	(0.5)	0,0,0,0,0
			43 (6)	2	2	0.0013	(0.0330)	0.059	(1.5)	0,1,0,0,0
WSTF	1/2 (12.7)	1/16 (1.6)	72 (10)	2	2	0.0024	(0.0610)	0.071	(1.8)	0,0,0,0,0
			58 (8)	2	2	0.0011	(0.0279)	0.059	(1.5)	0,0,0,0,0
			43 (6)	2	2	0.0004	(0.0102)	0.079	(2.0)	0,0,0,0,0
WSTF	3/4 (19.0)	1/8 (3.2)	72 (10)	2	2	0.0046	(0.1168)	0.118	(3.0)	0,0,0,0,0
			58 (8)	2	2	0.0042	(0.1067)	0.098	(2.5)	0,0,0,0,0
			43 (6)	2	2	0.0012	(0.0305)	0.071	(1.8)	0,0,0,0,0
WSTF	3/4 (19.0)	1/16 (1.6)	72 (10)	2	2	0.0026	(0.0660)	0.079	(2.0)	0,0,0,0,0
			58 (8)	2	2	0.0019	(0.0483)	0.071	(1.8)	0,0,0,0,0
			43 (6)	2	2	0.0009	(0.0229)	0.091	(2.3)	0,0,0,0,0

* d = average depth of impact
** c = average eccentricity of impact, difference between the impact and specimen centers
† # of Splits(S), # of Cracks(C), # of Delaminations(D), # of Reactions(R), # of Shear Lips(L)

Table C.b. Physical Measurements on Alloy WL049-T351 Specimens in LOX Ambient Environment.

Test Facility	Plate Thickness, in (mm)	Specimen Thickness, in (mm)	Potential Energy ft-lbs (kg-m)	Number of Specimens Impacted	Number of Specimens Measured	$\bar{d}^{*}$, in (mm)	$\bar{c}^{**}$, in (mm)	Other † (S,C,D,R,L)
WSTF	1/2 (12.7)	1/16 (1.6)	72 (10)	2	2	0.0076 (0.1930)	0.069 (1.75)	0,0,0,0,0
			58 (8)	2	2	0.0038 (0.0965)	0.069 (1.75))	0,0,0,0,0
			43 (6)	2	2	0.0033 (0.0838)	0.089 (2.25)	0,0,0,0,0

* d = average depth of impact
** c = average eccentricity of impact, difference between the impact and specimen centers
† # of Splits(S), # of Cracks(C), # of Delaminations(D), # of Reactions(R), # of Shear Lips(L)

Table C.7. Physical Measurements on Alloy WL049-T351 Specimens in LN$_2$ Ambient Environment.

Test Facility	Plate Thickness, in (mm)	Specimen Thickness, in (mm)	Potential Energy ft-lbs (kg-m)	Number of Specimens Impacted	Measured	$\bar{d}^*$, in (mm)		$\bar{c}^{**}$, in (mm)		Other † (S,C,D,R,L)
WSTF	1/2 (12.7)	1/16 (1.6)	72 (10)	2	2	0.0064	(0.1626)	0.069	(1.75)	0,0,0,0,0
			58 (8)	2	2	0.0041	(0.1041)	0.079	(2.0)	0,0,0,0,0
			43 (6)	2	2	0.0028	(0.0711)	0.098	(2.5)	0,0,0,0,0

* d = average depth of impact

** c = average eccentricity of impact, difference between the impact and specimen centers

† # of Splits(S), # of Cracks(C), # of Delaminations(D), # of Reactions(R), # of Shear Lips(L)

149

Table C.8. Physical Measurements on Alloy 2219-T851 Specimens in LOX Ambient Environment.

Test Facility	Plate Thickness, in (mm)	Specimen Thickness, in (mm)	Potential Energy ft-lbs (kg-m)	Number of Specimens Impacted	Number of Specimens Measured	$\bar{d}^*$, in (mm)	$\bar{c}^{**}$, in (mm)	Other † (S,C,D,R,L)
WSTF	1/2 (12.7)	1/8 (3.2)	72 (10)	2	2	0.0060 (0.1524)	0.039 (1.0)	0,0,0,0,0
			58 (8)	2	2	0.0058 (0.1473)	0.079 (2.0)	0,0,0,0,0
			43 (6)	2	2	0.0033 (0.0838)	0.091 (2.3)	0,0,0,0,0
WSTF	1/2 (12.7)	1/16 (1.6)	72 (10)	2	2	0.0010 (0.0254)	0.051 (1.3)	0,0,0,0,0
			58 (8)	2	2	0.0016 (0.4064)	0.059 (1.5)	0,0,0,0,0
			43 (6)	2	2	0.0026 (0.0660)	0.059 (1.5)	0,0,0,0,0

* d = average depth of impact
** c = average eccentricity of impact, difference between the impact and specimen centers
† # of Splits(S), # of Cracks(C), # of Delaminations(D), # of Reactions(R), # of Shear Lips(L)

Table C.9. Physical Measurements on Alloy 2219-T851 Specimens in LN2 Ambient Environment.

Test Facility	Plate Thickness, in (mm)	Specimen Thickness, in (mm)	Potential Energy ft-lbs (kg-m)	Number of Specimens Impacted	Number of Specimens Measured	$\bar{d}^*$, in (mm)	$\bar{c}^{**}$, in (mm)	Other † (S,C,D,R,L)
WSTF	1/2 (12.7)	1/8 (3.2)	72 (10)	2	2	0.0059 (0.1499)	0.047 (1.2)	0,0,0,0,0
			58 (8)	2	2	0.0053 (0.1346)	0.079 (2.0)	0,0,0,0,0
			43 (6)	2	2	0.0041 (0.1041)	0.098 (2.5)	0,0,0,0,0
WSTF	1/2 (12.7)	1/16 (1.6)	72 (10)	2	2	0.0049 (0.1245)	0.079 (2.0)	0,0,0,0,0
			58 (8)	2	2	0.0014 (0.0356)	0.059 (1.5)	0,0,0,0,0
			43 (6)	2	2	0.0027 (0.0686)	0.047 (1.2)	0,0,0,0,0

* d = average depth of impact
** c = average eccentricity of impact, difference between the impact and specimen centers
† # of Splits(S), # of Cracks(C), # of Delaminations(D), # of Reactions(R), # of Shear Lips(L)

Table C.10. Physical Measurements on Alloy 2219-T37 Specimens in LOX Ambient Environment.

Test Facility	Plate Thickness, in (mm)	Specimen Thickness, in (mm)	Potential Energy ft-lbs (kg-m)	Number of Specimens Impacted	Number of Specimens Measured	$\bar{d}$*, in (mm)	$\bar{c}$**, in (mm)	Other† (S,C,D,R,L)
WSTF	1/2 (12.7)	1/8 (3.2)	72 (10)	2	2	0.0098 (0.2489)	0.098 (2.5)	0,0,0,0,0
			58 (8)	2	2	0.0065 (0.1651)	0.091 (2.3)	0,0,0,0,0
			43 (6)	2	2	0.0040 (0.1016)	0.110 (2.8)	0,0,0,0,0
WSTF	1/2 (12.7)	1/16 (1.6)	72 (10)	2	2	0.0037 (0.0940)	0.091 (2.3)	0,0,0,0,0
			58 (8)	2	2	0.0039 (0.0991)	0.091 (2.3)	0,0,0,0,0
			43 (6)	2	2	0.0023 (0.0584)	0.079 (2.0)	0,0,0,0,0

* d = average depth of impact
** c = average eccentricity of impact, difference between the impact and specimen centers
† # of Splits(S), # of Cracks(C), # of Delaminations(D), # of Reactions(R), # of Shear Lips(L)

152

Table C.11. Physical Measurements on Alloy 2219-T37 Specimens in LN_2 Ambient Environment.

Test Facility	Plate Thickness, in (mm)	Specimen Thickness, in (mm)	Potential Energy ft-lbs (kg-m)	Number of Specimens Impacted	Number of Specimens Measured	$\bar{d}^*$, in (mm)		$\bar{c}^{**}$, in (mm)		Other † (S,C,D,R,L)
WSTF	1/2 (12.7)	1/8 (3.2)	72 (10)	2	2	0.0132	(0.3353)	0.110	(2.8)	0,0,0,0,0
			58 (8)	2	2	0.0025	(0.0635)	0.091	(2.3)	0,0,0,0,0
			43 (6)	2	2	0.0023	(0.0584)	0.110	(2.8)	0,0,0,0,0
WSTF	1/2 (12.7)	1/16 (1.6)	72 (10)	2	2	0.0048	(0.1219)	0.059	(1.5)	0,0,0,0,0
			58 (8)	2	2	0.0046	(0.1168)	0.130	(3.3)	0,0,0,0,0
			43 (6)	2	2	0.0018	(0.0457)	0.051	(1.3)	0,0,0,0,0

* d - average depth of impact
** c - average eccentricity of impact, difference between the impact and specimen centers
† # of Splits(S), # of Cracks(C), # of Delaminations(D), # of Reactions(R), # of Shear Lips(L)

153

Table C.12. Physical Measurements on Alloy 8090-T3 Specimens in 500 psi GOX Environment.

Test Facility	Plate Thickness, in (mm)	Specimen Thickness, in (mm)	Potential Energy ft-lbs (kg-m)	Number of Specimens Impacted	Number of Specimens Measured	$\bar{d}^*$, in (mm)	$\bar{c}^{**}$, in (mm)	Other † (S,C,D,R,L)
WSTF	1/2 (12.7)	1/16 (1.6)	72 (10)	20	40	0.0132 (0.3353)	0.054 (1.38)	0,0,0,0,3

154

* $\bar{d}$ - average depth of impact

** $\bar{c}$ - average eccentricity of impact, difference between the impact and specimen centers

† # of Splits(S), # of Cracks(C), # of Delaminations(D), # of Reactions(R), # of Shear Lips(L)

Table C.13. Physical Measurements on Alloy 8090-T3 Specimens (Factory Side Impacted) in 500 psi GOX Environment.

Test Facility	Plate Thickness, in (mm)	Specimen Thickness, in (mm)	Potential Energy ft-lbs (kg-m)	Number of Specimens Impacted	Number of Specimens Measured	$\bar{d}^*$, in (mm)		$\bar{c}^{**}$, in (mm)		Other † (S,C,D,R,L)
WSTF	1/2 (12.7)	1/16 (1.6)	72 (10)	9	9	0.0159 (0.4039)		0.035 (0.89)		0,0,0,0,8

* d = average depth of impact
** c = average eccentricity of impact, difference between the impact and specimen centers
† # of Splits(S), # of Cracks(C), # of Delaminations(D), # of Reactions(R), # of Shear Lips(L)

Table C.14. Physical Measurements on Alloy 8090-T3 Specimens in 100 psi LOX Environment.

Test Facility	Plate Thickness, in (mm)	Specimen Thickness, in (mm)	Potential Energy ft-lbs (kg-m)	Number of Specimens Impacted	Number of Specimens Measured	$\bar{d}^*$, in (mm)	$\bar{c}^{**}$, in (mm)	Other † (S,C,D,R,L)
MSFC	1/2 (12.7)	1/16 (1.6)	72 (10)	3	(1)	N/A stuck in cup	0.020 (0.50)	1,0,0,0,3

* d = average depth of impact

** c = average eccentricity of impact, difference between the impact and specimen centers

† # of Splits(S), # of Cracks(C), # of Delaminations(D), # of Reactions(R), # of Shear Lips(L)

Table C.15. Physical Measurement on Alloy 8090-T3 Specimens in 500 psi LOX Environment.

| Test Facility | Plate Thickness, in (mm) | Specimen Thickness, in (mm) | Potential Energy ft-lbs (kg-m) | Number of Specimens | | $\bar{d}^*$, | | $\bar{c}^{**}$, | | Other † (S,C,D,R,L) |
				Impacted	Measured	in	(mm)	in	(mm)	
WSTF	1/2 (12.7)	1/16 (1.6)	72 (10)	20	20	0.0114	(0.2896)	0.087	(2.22)	0,0,0,0,4
WSTF	1/2 (12.7)	1/16 (1.6)	72 (10)	5	4	0.0091	(0.2311)	0.039	(1.00)	0,0,0,3,4

* average depth of impact
** average eccentricity of impact
† # of Splits(S), # of Cracks(C), # of Delaminations(D), # of Reactions(R), # of Shear Lips(L)

157

Table C.16. Physical Measurement on Alloy 2090-T81 Specimens in 500 psi GOX Environment.

Test Facility	Plate Thickness, in (mm)	Specimen Thickness, in (mm)	Potential Energy ft-lbs (kg-m)	Number of Specimens Impacted	Number of Specimens Measured	$\overline{d}^*$, in (mm)		$\overline{c}^{**}$, in (mm)		Other † (S,C,D,R,L)
WSTF	3/4 (19.0)	1/16 (1.6)	72 (10)	40	39	0.0009 (0.0229)		(0.028) 0.71		0,0,0,0,0
WSTF	1/2 (12.7)	1/16 (1.6)	72 (10)	40	40	0.0010 (0.0254)		(0.031) (0.80)		2,0,0,0,0

* d - average depth of impact

** c - average eccentricity of impact, difference between the impact and specimen centers

† # of Splits(S), # of Cracks(C), # of Delaminations(D), # of Reactions(R), # of Shear Lips(L)

158

Table C.17. Physical Measurements on Alloy 2090-T81 Specimens in 50 psi LOX Environment.

Test Facility	Plate Thickness, in (mm)	Specimen Thickness, in (mm)	Potential Energy ft-lbs (kg-m)	Number of Specimens Impacted	Number of Specimens Measured	$\bar{d}^*$, in (mm)	$\bar{c}^{**}$, in (mm)	Other † (S,C,D,R,L)
MSFC	3/4 (19.0)	1/8 (3.2)	72 (10)	20	20	0.0127/ (0.3226/ 0.0069 0.2235)	N/A	-,-,-,0,-
MSFC	1/2 (12.7)	1/8 (3.2)	72 (10)	11	11	0.0121/ (0.3073/ 0.0088 0.2235)	N/A	-,-,-,0,-

* d = average depth of impact

** c = average eccentricity of impact

† # of Splits(S), # of Cracks(C), # of Delaminations(D), # of Reactions(R), # of Shear Lips(L)

Table C.18. Physical Measurements on Alloy 2090-T81 Specimens in 100 psi LOX Environment.

Test Facility	Plate Thickness, in (mm)	Specimen Thickness, in (mm)	Potential Energy ft-lbs (kg-m)	Number of Specimens Impacted	Number of Specimens Measured	$\bar{d}^*$, in (mm)	$\bar{c}^{**}$, in (mm)	Other † (S,C,D,R,L)
MSFC	3/4 (19.0)	1/8 (3.2)	72 (10)	20	20	0.0105/ (0.2667/ 0.0048 0.1219)		-,-,-,0,-
MSFC	1/2 (12.7)	1/8 (3.2)	72 (10)	20	20	0.0134/ (0.3404/ 0.0089 0.2261)	N/A	-,-,-,0,-
SSFL	1/2 (12.7)	1/8 (3.2)	72 (10)	20	20	0.0110 (0.2794)	0.026 (0.65)	1,8,1,0,15
MSFC	1/2 (12.7)	1/16 (1.6)	72 (10)	20	17	0.0126 (0.3200)	0.028 (0.70)	17,0,1,1,17
SSFL	1/2 (12.7)	1/8 (3.2)	72 (10)	20	20	0.0121 (0.3073)	N/A	-,-,-,0,-

* $\bar{d}$ = av rage depth of impact

** $\bar{c}$ = av rage eccentricity of impact, difference between the impact and specimen centers

† # of Splits(S), # of Cracks(C), # of Delaminations(D), # of Reactions(R), # of Shear Lips(L)

160

Table C.19. Physical Measurements on Alloy 2090-T81 Specimens in 400 psi LOX Environment.

Test Facility	Plate Thickness, in (mm)	Specimen Thickness, in (mm)	Potential Energy ft-lbs (kg-m)	Number of Specimens Impacted	Number of Specimens Measured	d*, in (mm)	c̄**, in (mm)	Other † (S,C,D,R,L)
SSFL	1/2 (12.7)	1/8 (3.2)	72 (10)	20	20	0.0136 (0.3454)	0.020 (0.50)	7,8,0,0,19

* d = average depth of impact
** c = average eccentricity of impact, difference between the impact and specimen centers
† # of Splits(S), # of Cracks(C), # of Delaminations(D), # of Reactions(R), # of Shear Lips(L)

161

Table C.20. Physical Measurements on Alloy 2090-T81 Specimens in 500 psi LOX Environment.

Test Facility	Plate Thickness, in (mm)	Specimen Thickness, in (mm)	Potential Energy ft-lbs (kg-m)	Number of Specimens Impacted	Number of Specimens Measured	$\bar{d}^*$, in (mm)		$\bar{c}^{**}$, in (mm)		Other † (S,C,D,R,L)
MSFC	3/4 (19.0)	1/8 (3.2)	72 (10)	20	20	0.0114/	(0.2896/	0.031	(0.78)	2,0,0,0,5
WSTF	3/4 (19.0)	1/16 (1.6)	72 (10)	20	20	0.0012	(0.0305)	0.078	(1.98)	0,0,0,0,0
MSFC	3/4 (19.0)	1/16 (1.6)	72 (10)	9	7	0.0099 0.0057	(0.2515/ 0.1448)	N/A		-,-,-,2,-
MSFC	1/2 (12.7)	1/8 (3.2)	72 (10)	20	17	0.0145	(0.3683)	0.038	(0.97)	11,1,5,1,5
WSTF	1/2 (12.7)	1/16 (1.6)	72 (10)	20	17	0.0016	(0.0406)	0.072	(1.83)	0,0,0,0,0
MSFC	1/2 (12.7)	1/16 (1.6)	72 (10)	5	3	0.0082	(0.2083)	0.026	(0.67)	1,0,2,2,N/A
WSTF	3/4 (19.0)	1/8 (3.2)	72 (10)	20	20	0.0017	(0.0432)	0.078	(1.98)	0,0,0,0,0
WSTF	1/2 (12.7)	1/8 (3.2)	72 (10)	20	20	0.0032	(0.0813)	0.089	(2.25)	0,0,0,0,

* d - average depth of impact
** c - average eccentricity of impact
† # of Splits(S), # of Cracks(C), # of Delaminations(D), # of Reactions(R), # of Shear Lips(L)

162

Table C.21. Physical Measurements on Alloy 2090-T81 Specimens in 1000 psi LOX Environment.

Test Facility	Plate Thickness, in (mm)	Specimen Thickness, in (mm)	Impact Energy ft-lbs (kg-m)	Number of Specimens Impacted	Measured	d^*, in (mm)	$\bar{c}^{**}$, in (mm)	Other † (S,C,D,R,L)
SSFL	1/2 (12.7)	1/8 (3.2)	72 (10)	20	18	0.0128 (0.3251)	0.022 (0.56)	4,2,0,0,16

* d -average depth of impact

** c - average eccentricity of impact

† # of Splits(S), # of Cracks(C), # of Delaminations(D), # of Reactions(R), # of Shear Lips(L)

Table C.22. Physical Measurements on Alloy WL049-T351 Specimens in 500 psi GOX Environment.

Test Facility	Plate Thickness, in (mm)	Specimen Thickness, in (mm)	Potential Energy ft-lbs (kg-m)	Number of Specimens Impacted	Number of Specimens Measured	$\bar{d}^*$, in (mm)	$\bar{c}^{**}$, in (mm)	Other † (S,C,D,R,L)
WSTF	1/2 (12.7)	1/16 (1.6)	72 (10)	20	20	0.0029 (0.0747)	0.027 (0.68)	0,0,0,0,0

* d - average depth of impact
** c - average eccentricity of impact
† # of Splits(S), # of Cracks(C), # of Delaminations(D), # of Reactions(R), # of Shear Lips(L)

164

Table C.23. Physical Measurements on Alloy WL049-T351 Specimens in 500 psi LOX Environment.

Test Facility	Plate Thickness, in (mm)	Specimen Thickness, in (mm)	Potential Energy ft-lbs (kg-m)	Number of Specimens Impacted	Number of Specimens Measured	$\overline{d}^*$, in (mm)	$\overline{c}^{**}$, in (mm)	Other † (S,C,D,R,L)
WSTF	1/2 (12.7)	1/16 (1.6)	72 (10)	20	20	0.0024 (0.0610)	0.086 (2.18)	0,0,0,0,0

* d — average depth of impact
** c — average eccentricity of impact
† # of Splits(S), # of Cracks(C), # of Delaminations(D), # of Reactions(R), # of Shear Lips(L)

165

Table C.24. Physical Measurements on Alloy 2219-T851 Specimens in 500 psi GOX Environment.

Test Facility	Plate Thickness, in (mm)	Specimen Thickness, in (mm)	Potential Energy ft-lbs (kg-m)	Number of Specimens Impacted Measured		$\bar{d}^*$, in (mm)	$\bar{c}^{**}$, in (mm)	Other † (S,C,D,R,L)
WSTF	1/2 (12.7)	1/16 (1.6)	72 (10)	20	20	0.0014 (0.0356)	0.041 (1.03)	0,1,0,0,0

* d = average depth of impact

** c = average eccentricity of impact

† # of Splits(S), # of Cracks(C), # of Delaminations(D), # of Reactions(R), # of Shear Lips(L)

166

Table C.25. Physical Measurements on Alloy 2219-T851 Specimens in 500 psi LOX Environment.

Test Facility	Plate Thickness, in (mm)	Specimen Thickness, in (mm)	Potential Energy ft-lbs (kg-m)	Number of Specimens Impacted	Number of Specimens Measured	$\bar{d}^*$, in (mm)	$\bar{c}^{**}$, in (mm)	Other † (S,C,D,R,L)
WSTF	1/2 (12.7)	1/16 (1.6)	72 (10)	20	20	0.0025 (0.0635)	0.081 (2.05)	0,0,0,0,0
MSFC	1/2 (12.7)	1/16 (1.6)	72 (10)	20	19	0.0085 (0.2159)	0.041 (1.05)	0,0,3,2,4

* d = average depth of impact

** c = average eccentricity of impact

† # of Splits(S), # of Cracks(C), # of Delaminations(D), # of Reactions(R), # of Shear Lips(L)

167

Table C.26. Physical Measurements on Alloy 2219-T37 Specimens in 500 psi GOX Environment.

Test Facility	Plate Thickness, in (mm)	Specimen Thickness, in (mm)	Potential Energy ft-lbs (kg-m)	Number of Specimens Impacted	Measured	$\bar{d}^*$, in (mm)	$\bar{c}^{**}$, in (mm)	Other † (S,C,D,R,L)
WSTF	1/2 (12.7)	1/16 (1.6)	72 (10)	40	40	0.0022 (0.0559)	0.044 (1.13)	0,0,0,0,0

* d -average depth of impact

** c - average eccentricity of impact

† # of Splits(S), # of Cracks(C), # of Delaminations(D), # of Reactions(R), # of Shear Lips(L)

168

Table C.27. Physical Measurements on Alloy 2219-T37 Specimens in 500 psi LOX Environment.

Test Facility	Plate Thickness, in (mm)	Specimen Thickness, in (mm)	Potential Energy ft-lbs (kg·m)	Number of Specimens Impacted	Number of Specimens Measured	$\bar{d}^*$, in (mm)	$\bar{c}^{**}$, in (mm)	Other † (S,C,D,R,L)
WSTF	1/2 (12.7)	1/16 (1.6)	72 (10)	20	20	0.0025 (0.0483)	0.068 (1.73)	0,0,0,0,0
MSFC	1/2 (12.7)	1/16 (1.6)	72 (10)	20	19	0.0068 (0.1727)	0.041 (1.03)	0,0,0,2,8

* d = average depth of impact
** c = average eccentricity of impact
† # of Splits(S), # of Cracks(C), # of Delaminations(D), # of Reactions(R), # of Shear Lips(L)

APPENDIX D

Report from **F. W. Gayle**, National Institute

of Standards and Technology, Gaithersburg, MD

(November 1989).

11-17-89

Dick,

We have examined the striker pin from the failed sample, "2219-T851, 500 psi LOX, #19". The attached micros show typical damage on the edge of this pin. The first set (away from the reaction) indicates the type of edge damage which looked common in the pins I viewed in Boulder. The "beveled" edge with associated pushed up lip may well lead to a greater severity of test: the bevel would encourage metal flow near the bevel whereas the lip would effectively increase the scraping of the aluminum surface. The "lip" is not very high but could play a role in a clean removal of the aluminum oxide from the test specimen. Whatever the failure mechanism, this could be a contributing cause which would be absent if pins in good condition were used.

The second set of micros shows the region near the reaction. The hole with Cr-rich deposits is just below one of the "beveled" regions. If the LOX failure (or at least initiation) was associated with a reaction with the Inconel (catalytic or thermit, etc.), then the hole may represent an initiation site.

I have focussed on failure mechanisms associated with the striker pin, but of course this theory is only one of several. I think an SEM examination of passed and failed LOX specimens (and passed and failed striker pins!), either here or in Boulder, would be the best next step. That would give you a better idea of what to look for with the surface analysis equipment.

For your information, the composition we found for the pin was, in weight percent:
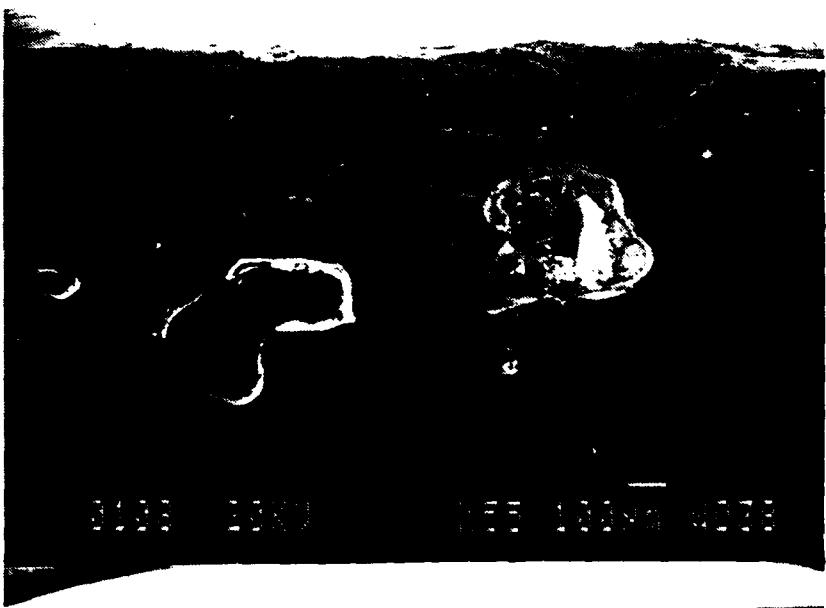
	Ni	Cr	Fe	C	Al	Ti	Nb	Mo
EDS-Pin 19	54.9	19.3	17.1	--	0.4	1.0	4.1	3.3
Inconel 718 nom.	53.5	18.6	18.5	0.04	0.4	0.9	5.0	3.1
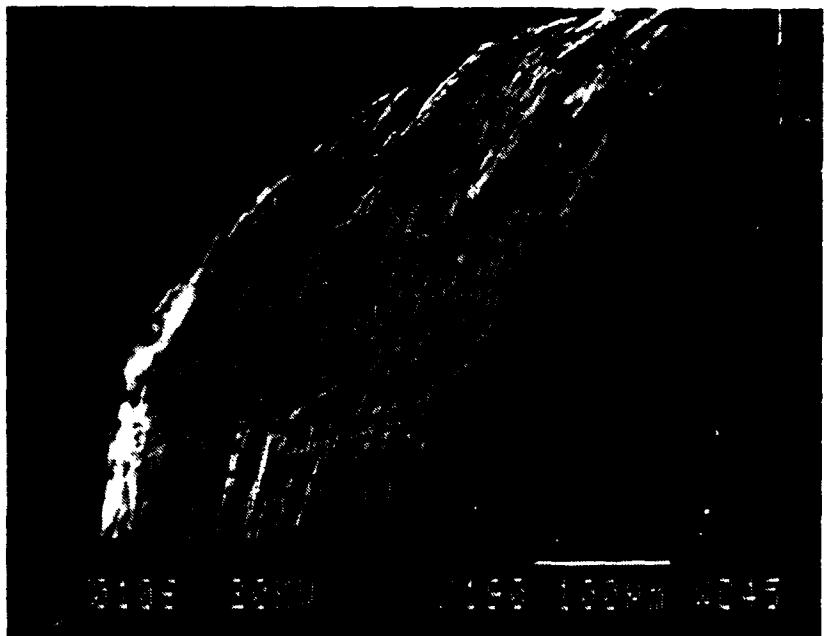
Thus the pin is indeed Inconel 718.

Regards,
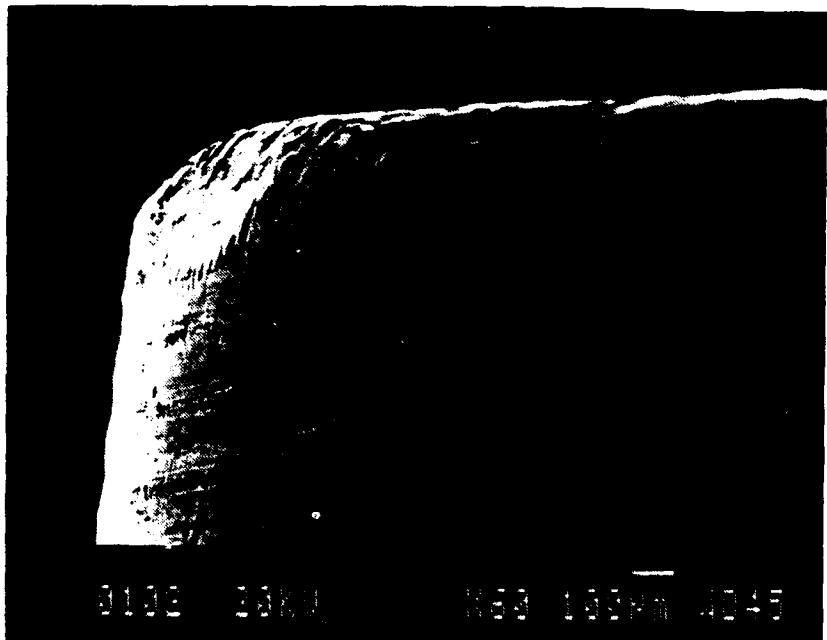
Frank W. Gayle

2219-T851
500 psi LOX, #19

Striker pin, near reaction

Cr-rich deposit

Damaged area just below bevel
(Cr-rich deposition hole)

Striker pin surface and side
Spattered Al-rich oxide.

2219-T851
500 psi LOλ, #19
Striker pin surface

Typical damaged edge
resulting in a bevel
and generally a raised
lip on the flat striker
surface.

There is a thin layer
of Al or Λlumina on
the damaged surface.

175/176

APPENDIX E

Summary Report on Observation Made on

Aluminum and Aluminum-Lithium Alloys Subjected

to Impact While in Contact with Liquid Oxygen.

M. B. Kasen, Boulder, CO (December 1989).

SUMMARY REPORT ON OBSERVATIONS MADE ON ALUMINUM
AND ALUMINUM-LITHIUM ALLOYS SUBJECTED TO IMPACT
WHILE IN CONTACT WITH LIQUID OXYGEN

Submitted by:

M. B. Kasen

I examined thirteen ignited specimens encompassing 2219 alloy (Al-Cu), 8090 alloy (Al-Li), and 2090 alloy (Al-Li), all tested at either MSFC or WSTF. All were 1/16" thick, and were impacted at either 100 or 500 psi pressure. I also examined specimens of the same alloys that had developed significant radial cracking, but no ignition. My major observations are as follows:

a) It would appear most logical for a reaction to start by oxidation of fresh surfaces created by cracking. However, while creation of such surfaces may be a necessary requirement for ignition, it is evidently not a sufficient criterion, because ignition was not observed to form at crack sites.

b) Ignition appears to have initiated below the specimen surface followed by an explosive reaction that caused rapid expulsion of combustion products. This is evidenced by the formation of blowholes or cavities (2219-#15 and 8090-#1), by the sharp edges surrounding the ignition sites (2219-#12, 2219-#15, 2219-#20), and by the observation that the cavity orientation and direction of expulsion is, in some cases, at a substantial angle from surface normal of the specimen (2090-#17).

c) Examination of specimen 8090-#1 suggests that the combustion mechanism of this alloy may differ from that of 2090 and 2219. Here one observes formation of cavities having relatively clean, smooth, shiny surfaces containing a few black spots. This contrasts with the very rough, dark surface of the ignition sites in the other alloys. Also, what appears to be a transparent, amorphous residue was noted around two of the cavities and inside a third, while a large amount of a finely-divided, white, amorphous-appearing powder residue was observed near the cavities and distributed near the shear lip all the way around the indentation. This was not observed in the other alloys.

d) There was some evidence of very localized ignition that

did not go catastrophic--for example, 2090-#12, -#13 show black spots that could be interpreted in this manner. Both specimens evidenced some radial cracking, but not associated with the possible ignition sites. Specimen 2090-#14 showed evidence of localized ignition associated with an unburned radial crack. This suggests that ignition either started adjacent to the crack or that the crack formed after cessation of burning.

e) The impact area of the ram was clean in all ignited specimens. The absence of ignition sites or of slag particles in this region indicates that the ram face remained in contact with the specimen during the burning event.

I also examined a series of 1/8" thick specimens impacted by SSFL at 100, 400, or 1000 psi LOX pressure. These specimens did not evidence catastrophic ignition. However, a careful examination of the fracture surfaces at high binocular magnification indicated that melting had occurred internally in what appeared to be a layered structure. This was most evident in specimen 2090-#14 and 2090-#1, but could be also noted in 2090-#19. The melting was evidenced by formation of very smooth surfaces interspersed with roughly fractured surfaces. Subsequent examination of 1/8" thick MSFC specimen 2090-#16 also showed similar evidence of internal melting. The most likely cause of the melting would appear to be overheating of low melting eutectic constituents during impact.

Comment:

Ignition is defined as achieving a condition where the rate of heat input is in excess of the rate of heat removal. That ignition did not begin on the fresh surfaces created by massive radial cracking, despite the certainty that oxidation was proceeding at such surfaces, suggests that the rate of oxidation was insufficient to generate the heat required for ignition under the prevailing conditions. This could be influenced by the substantial width of the cracks, which may have permitted substantial cooling by the surrounding LOX.

A required condition, not only for ignition, but for catastrophic explosive burning, is confinement of the oxidation reaction. The evidence suggests that this occurred in some of the specimens during impact. The available evidence is inadequate to precisely define the sequence of events; however a possible scenario could be as follows. It is necessary to have a path for oxygen to penetrate the surface. The impact could create a small, tight crack, into which oxygen, gassified by the temperature of the impact, is forced. The heat produced by the resulting oxidation reaction is now confined, and divorced from the cooling effect of the LOX. Increased temperature would increase localized pressure, resulting in increased oxidation which, in turn, further increases temperature and pressure. This

undamped series of events could theoretically provide the necessary conditions for both ignition and catastrophic explosion.

The extent to which localized internal melting contributes to ignition could not specifically be determined. It is possible that a surface crack could penetrate to the melted zone, in which case the reaction proposed above would likely be exacerbated by contact of high-pressure oxygen with already melted constituents that may contain substantial amounts of highly-reactive components such as magnesium or lithium.

APPENDIX F

Surface Chemistries of Selected Al-Li Alloys

and Alloy 2219.

C. C. Wan, Aerospace Corporation, Los Angeles, CA

(December 1989).

LIST OF SAMPLES EXAMINED

SAMPLE 1 (8090) Sample stapled in teflon bag

SAMPLE 2 (8090) Sample in normally heat sealed teflon bag, $1\frac{1}{2}$ x $1\frac{1}{2}$"

SAMPLE 3 (8090) Sample wrapped in clean room tissue

SAMPLE 4 (8090) Bag sealed in area remote from sample

SAMPLE 5 (2090) Sample to be machined later at Aerospace

SAMPLE 6 (2090) Sample to be machined later at Aerospace

Sample 7 (2090) Al-Li T8 E 41 impacted sample @8Kg-m, ambient-LOX from $\frac{1}{2}$" plate #4

Sample 8 (2090) T8 E 41 1/8" from 3/4" Plate 500 PSI LOX #5 MSFC (No reaction)

SAMPLE 9 (2090) Al-Li Spec#11 impacted @ 6Kg-m ambient LOX from 3/4" Plate

Sample 10 (2219) T37 500 PSI LOX #12 MSFC   REACTION

SAMPLE 11 (8090) T3 500 PSI LOX #1 MSFC   REACTION

SAMPLE 12 (8090) T3 500 PSI GOX WSTF #369 (No Reaction)

SAMPLE 5A (2090) Dry machined sample #5 surface

SAMPLE 6A (2090) Dry machined sample #6 surface

Sample 6A (2090) Rocketdyne sample

Sample 18 (2090) Rocketdyne sample

8090-1   (8090)

8090-2   (8090)

GENERAL OBSERVATIONS:

All the samples listed were observed to have some fluorine and chlorine on the surfaces except samples 5A and 6A which were freshly machined.

Only six of the 18 samples were observed to have barium on their surfaces: the were samples # 7, 8, 9, 10, 11, and 12. These six samples were all impacted at var locations and different conditions, see list of samples. Two other samples were al impacted at Rocketdyne, 8A and 18, but these had no barium.

An estimate was made of the surface contamination from "organics". These subs produce a spectrum of peaks in which each mass number is present at a substantial level between 20 and 100. Such an estimate is highly subjective and is crude at best The contamination was arbitrarily divided into three groups, low, moderate, and high Those with low contamination are: 1, 2, 3, 4, 10, 11, 5A, 6A, 8090-1 and 8090-2. Those moderately contaminated were: 5, 6, 7, and 8. Those with the heaviest contam were; 9, 12, 8A, and 18.

The first four samples examined by the IMMA were four 8090 alloy discs which had been cleaned according to proceedure 8060.13 and which had been packaged using four different techniques:

Sample 1   Sample stapled in teflon bag.

Sample 2   Sample in normally spaced heat sealed teflon bag, $1\frac{1}{2}$x$1\frac{1}{2}$".

Sample 3   Sample wrapped in clean room tissue.

Sample 4   Bag sealed at location remote from sample.

The surface analyses of these four sample are shown in table 1. The positive ion analysis is normalized to the Al^{27} peak and the negative ion analysis is normalized to the C^{16} peak.

TABLE 1

ELEMENT	Sample 1	Sample 2	Sample 3	Sample 4
Al^{27}	1	1	1	1
Li^{7}	1.6E-1	2.4E-1	2.1E-1	2.2E-1
Mg^{24}	1.2E-2	1.1E-2	1.3E-2	1.1E-2
Ca^{40}	3.8E-3	6.6E-3	9.3E-3	6.7E-3
Zr^{90}	3.8E-5	4.2E-5	4.4E-5	3.8E-5
Si^{28}	3.6E-3	4.2E-3	2.6E-3	3.6E-3
Na^{23}	8.4E-3	5.7E-3	2.6E-2	1.6E-2
Ba^{138}	-	-	-	-
F^{19}	2.0E-4	2.3E-4	5.6E-4	4.0E-4
K^{39}	3.5E-3	2.2E-3	1.1E-3	5.5E-3
Cu^{63}	5.0E-4	4.8E-4	9.1E-4	8.0E-4
C^{16}	1	1	1	1
H^{1}	3.0E-2	2.6E-2	1.3E-2	3.0E-2
C^{12}	1.7E-2	3.5E-2	1.4E-2	1.9E-2
F^{19}	4.1E-2	4.6E-2	8.6E-2	5.3E-2
Cl^{35}	2.7E-3	1.1E-2	9.2E-3	8.9E-3

The amplitude of the peaks measured by the IMMA depend upon a number of factors such as surface smoothness, surface orientation, the presence of other elements, etc so that variations of a factor of 2 or 3 may be expected when comparing readings taken at different locations on the same sample. The readings listed in table 1 are for the most part well within this range. The conclusion from these data is that there was no measurable effect of the packaging technique on the surface chemistry of these four discs.

All the samples received for inspection by the IMMA were reported to have been cleaned according to proceedure 8060.1B. Two of these samples, #5 and #6 were analysed by the IMMA and then were sent to the machine shop to ~~remove~~ 15 to 20 mils of material using clean, dry techniques, i.e. no oil on chuck or cutting tool. The cleanly machined surfaces were then re-examined in the IMMA. The before and after readings for one of these samples, #5 is shown in Table 2.

Table 2

ELEMENT	Sample #5 (8060.1B)	Sample #5(A) (After machining)
Al^{27}	1	1
Li^7	2.5E-1	9.8E-1
Mg^{24}	2.0E-2	2.0E-4
Ca^{40}	5.6E-2	5.0E-6
Zr^{90}	8.0E-5	3.0E-5
Si^{28}	2.7E-3	5.8E-3
Na^{23}	6.9E-1	2.8E-4
Ba^{138}	0	0
F^{19}	8.0E-4	0
K^{39}	6.4E-1	3.0E-5
Cu^{63}	7.7E-4	4.0E-4
O^{16}	1	1
H^1	1.1E-1	6.3E-3
C^{12}	2.3E-1	1.8E-3
F^{19}	6.3E-2	?

The comparison of the before and after machining surface chemistry of sample #5 clearly indicated that the machining removed from the surface most of the common electrolytes, ie., Na, K, Ca, A~D Mg as well as F, H and C. Since sample #5 had a surface chemistry which was similar to the other samples, it is suggested that the sample

preparation techniques used to machine and clean the samples leaves a surface depo

on the samples which is rich in the afore mentioned elements. The electrolytes

seen here are commonly found on surfaces washed in tap water, as opposed to ultra

high purity water, The fluorine along with the H and C one would reasonably expec

to find on a sample "degreased" with a commercial fluorocarbon solvent, ie Freon.

APPENDIX G

Ignited Specimens of 2090-T81 That Are

Retained by Marshall Space Flight Center.

Courtesy J. Davis, Marshall Space Flight Center,

Huntsville, AL (December 1989).
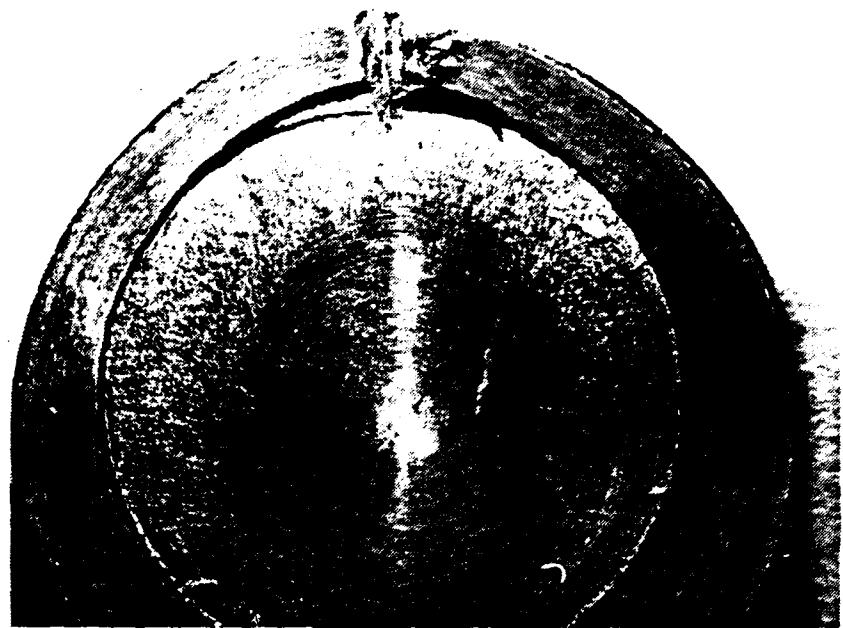
Figure I.G-1.   Alloy 2090-T81 at 50 psi (LOX), 1/8 inch thick specimen
(#4) from 1/2 inch plate.
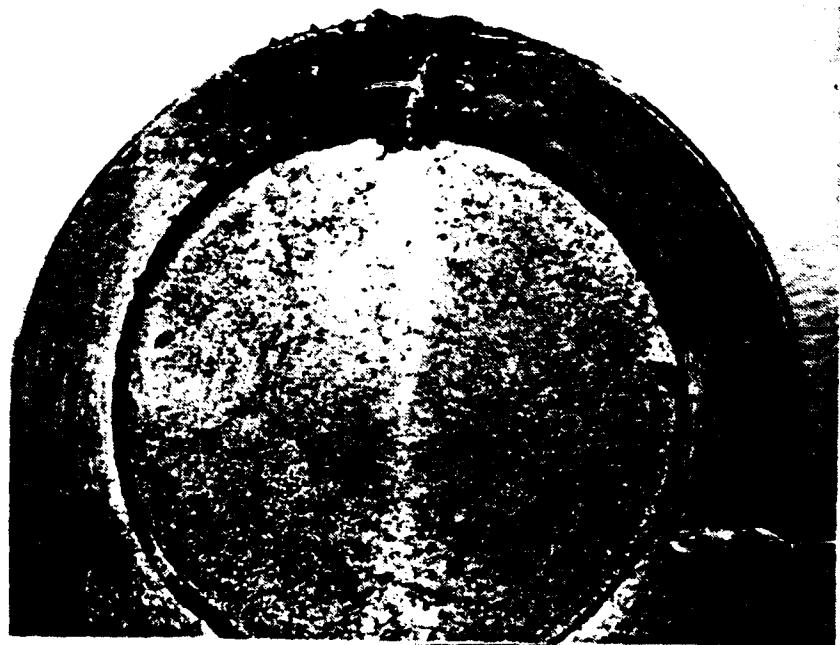
Figure I.G-2.   Alloy 2090-T81 at 50 psi (LOX), 18 inch thick specimen
(#11) from 1/2 inch plate.
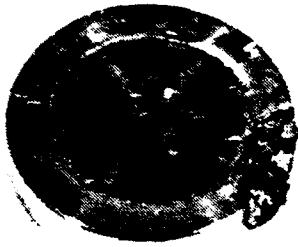
Figure I.G-3. Alloy 2090-T81 at 50 psi (LOX), 1/8 inch thick specimen (#8) from 1/2 inch plate.

Figure I.G-4. Alloy 2090-T81 at 100 psi (LOX),m 1/8 inch thick
specimen (#8) from 3/4 inch plate.

Figure I.G-5. Alloy 2090-T81 at 100 psi (LOX), 1/8 inch thick sp
(#14) from 3/4 inch plate.